Spring 2014

Numerical simulations for wellbore stability and integrity for drilling and completions

Nevan Christopher Himmelberg

Department:

NUMERICAL SIMULATIONS FOR WELLBORE STABILITY AND INTEGRITY FOR DRILLING AND COMPLETIONS

by

NEVAN CHRISTOPHER HIMMELBERG

A THESIS

Presented to the Faculty of the Graduate School of the

MISSOURI UNIVERSITY OF SCIENCE AND TECHNOLOGY

In Partial Fulfillment of the Requirements for the Degree

MASTER OF SCIENCE IN PETROLEUM ENGINEERING

2014

Approved by

Andreas Eckert, Advisor
Runar Nygaard
Ralph E. Flori, Jr.

ABSTRACT

Conventional wellbore trajectory planning is commonly based on an Andersonian state of stress [SoS] and the optimum well azimuth and inclination for a specific depth can be determined using stereographic projections of the safe mud weight window. In this thesis a new methodology using the complete stress tensor is developed to determine optimal well trajectories for complex in-situ stress scenarios. This study uses a 3D finite element analysis to simulate the SoS based on an integrated 3D MEM. The model yields the complete stress tensor at every location for a planned future well path. Using standard equations to determine the wellbore SoS for inclined wellbores the safe operational pressure window can be determined.

Included is a wellbore integrity study on the cement sheath of a well proposed for CO_2 sequestration. This includes both the mechanical interactions of the casing, cement, and formation as well as the effects of temperature change which would be caused by CO_2 injection. The use of a staged finite element model to accurately predict the pre-cementing wellbore SoS is proposed. The SoS results are then implemented into a wellbore model with a perfectly bonded cement sheath in order to investigate the effects of cement curing and degradation.

In this study the evolution of Young's Modulus during cement curing, and de-evolution during cement degradation is accounted for. Traditional cement integrity studies use only a constant value for Young's Modulus. The finite element models show that inclusion of cement hardening may increase the risk of shear failure in the cement, while inclusion of cement degradation may lead to tensile failure during cold CO_2 injection.

ACKNOWLEDGMENTS

I would like to thank my advisor, Dr. Andreas Eckert, for accepting me into both the OURE program and then the geomechanical modeling group as a research assistant. During my time here he has always been an encouraging and supportive mentor in my studies. His technical and editorial guidance have been paramount to the completion of this work. I would also like to express my thanks and gratitude to the United States Department of Energy for funding of this research.

I would also like to thank Dr. Flori and Dr. Nygaard for their help and presence on my graduate committee. They have provided invaluable advice in regards to both the completion of this thesis and career guidance. My thanks also go to my friends and colleagues in the geomechanical modeling group: Xiaolong Liu, Deepak Gokaraju, Kaixiao Tian, Mengke Lee, Weichang Zhang, Amin Amirlatifi, Mathew Paradeis, and Ben Weideman. Their assistance and friendly work environment made the completion of this work possible. Special thanks go to Xiaolong Liu who endured my company 24 hours a day as my close friend and roommate.

Last but not least I would like to thank my family; my parents Mike and Debbie Himmelberg for their encouragement and support throughout this process, and to my fiancée Gracie Zieman for her love, encouragement, and unwavering faith that I can overcome any obstacle.

TABLE OF CONTENTS

Page

LIST OF ILLUSTRATIONS

Page

LIST OF TABLES

Page

1. WELLBORE OPTIMIZATION INTRODUCTION

1.1. OVERVIEW

During the life of a petroleum reservoir many engineering operations are performed, many of which are affected by the in-situ state of stress in the reservoir. One of the most important applications in the discipline of drilling engineering which will be discussed herein is wellbore stability. Unstable wells, amongst others, cause reduced drilling performance, lost circulation, stuck bottom hole assembly, well work-over costs, and at worst can lead to a total collapse and a loss of the wellbore. A thorough geomechanical analysis in the planning stage of a well can significantly reduce these risks. A large number of 'conventional' wellbore trajectory planning studies utilize 1D Mechanical Earth Models (MEMs) to predict the reservoir state of stress and rock strength parameters from wireline logging measurements and hydraulic mini-frac tests. Based on these data sets a mud pressure window for the logged well can be obtained. One method for enhancing wellbore stability is to orient the wellbore's trajectory in such a way that the influence of the stresses acting on the wellbore wall are minimized.

The ability to accurately model the state of stress for complex geometries using the Mechanical Earth Modeling (MEM) technology/approach allows for pre-drilling wellbore stability analyses. The methodology to predict an optimized wellbore trajectory presented in this study implements the complete stress tensor which is obtained from reservoir scale finite element (FE) models. The stresses obtained from the FE model are used to calculate stable operational pressure windows. Stereonet projections of these pressure windows are utilized to determine the most stable wellbore trajectories for the given state of stress.

This process of wellbore trajectory planning is playing an increasingly important role in the petroleum industry. Oil reservoirs currently being discovered are situated in complex geologic scenarios such as sub-salt and significant challenges with respect to safe drilling operations arise. This increase in drilling difficulty is due to increased depth, reservoir complexity, and surface location conditions; with many of them being in offshore locations. This has created a need for more accurate methods in determining safe wellbore trajectories. The effects of poor wellbore planning results in stuck pipe, fluid

loss, and catastrophic blowouts. Because of this conscious efforts to improve pre-drilling workflows to include wellbore trajectory optimization when handling complex reservoir scenarios are necessary.

A methodology for determining safe wellbore trajectories for deviated wells calculating safe mud pressure windows has been documented by Peska and Zoback (1995). If unstable conditions occur, stereographic projections are utilized to find more optimal drilling azimuths and inclinations for different wells in the same field (Zoback, 2007; Rahim et al., 2012; Last et al., 1996). While this approach proves successful and valid for a large number of case studies it utilizes the inherent assumption of an Andersonian state of stress (ASoS) and thus is not valid for cases where complex geologic structures violate this assumption.

In this thesis this methodology has been adapted for use in conjunction with finite element models [FEM]. The pressure windows are constructed from stress data which is obtained from reservoir scale FEMs. These FEMs are capable to accurately reproduce reservoir stress conditions when created from accurate geometries and rock property data (Goodman and Connolly 2007). By combining this methodology with reservoir scale FEMs, stable drilling directions can be determined, thereby reducing the likelihood of catastrophic wellbore failure. Based on 3D numerical MEMs the methodology presented in this thesis represents a valuable work process to optimize wellbore trajectories in the planning stage of a well. Assumptions on the state of stress are not necessary as the 3D MEM provides the complete stress tensor at any location in the model. The methodology is based on most general mathematical description and thus enables all possible scenarios of azimuth, inclination and surface rig location for multiple well types along the entire trajectory of the well path. The methodology can also be applied for any failure criterion.

1.2. LITERATURE REVIEW

Wellbore trajectory planning plays an important role in the development and optimization of any petroleum field. The placement of a wellbore may not only influence the amount of hydrocarbons contacted, but will also influence the ease at which a well is drilled (Aadnøy et al., 2005; Zare-Reisabadi et al., 2012), its long-term integrity (Zare-Reisabadi et al., 2012) and affect hydraulic fracture stimulations (Feng and Shi, 2013).

With the advent of new drilling techniques, the enhanced accuracy during the drilling process and the ability to drill various types and shapes of wells has resulted in a demand and understanding of wellbore trajectory planning (Cooper, 1994; Bourgoyne et al., 1986; Fjaer et al., 2008). Stable wellbore conditions with respect to mechanical failure are a function of the geometrical trajectory within the 3D state of stress (Aadnøy et al., 2005). Wellbore stability can be predicted by determining safe mud pressures preventing either borehole breakdown or collapse (Aadnøy et al., 2005; Zare-Reisabadi et al., 2012; Cooper, 1994; Bourgoyne et al., 1986; Fjaer et al., 2008; Zoback, 2007; Yang et al., 2012; Barton et al., 1997). Thus, a thorough knowledge of the in-situ stresses in the subsurface and how they change during the life of a petroleum field is a crucial input parameter for planning stable wellbores.

Most wellbore trajectory planning studies (Aadnøy et al., 2005; Zare-Reisabadi et al., 2012; Feng and Shi, 2013; Yang et al., 2012; Barton et al., 1997; Tan et al., 2013; Islam et al., 2010; Al-Ajmi and Zimmerman, 2009; Peska and Zoback, 1995) assume an Andersonian state of stress [ASoS] (Twiss and Moores, 2007), where one principal stress is vertical; a common observation in the Earth's crust (Brudy et al., 1997; Zoback, 2007). Implicitly this assumption excludes many scenarios where complex geologic conditions, such as heavily faulted or folded regions, areas subjected to salt intrusion, and any shallow regions where unconsolidated rock is encountered, imply that the SoS is not Andersonian and that shear stresses have to be considered (Zoback, 2007; Tan et al., 2013; Schutjens et al., 2012). When drilling in regions where the stress tensor may be rapidly changing, an inclination or azimuth change of 5^{o} of the wellbore trajectory may result in a significant change in the stress magnitudes acting on the wellbore wall. Assuming an ASoS also introduces a potentially misleading symmetry between drilling directions. In an ASoS the conditions for the stable mud pressure window in any azimuthal combination, which are 180^{o} offset from each other, will be equal at the same inclination. With the addition of shear stresses this is no longer true.

Another limitation of wellbore trajectory studies is the utilization of stereographic projections to predict the safe mud pressure window (Zoback, 2007; Peska and Zoback, 1995; Rahim et al., 2012; Last et al., 1996). Stereographic projections enable visualization of the full range of effects that inclination and azimuth have on the mud

pressure window. Unfortunately, these projection plots are only valid for a specific depth. Rapidly changing stresses with depth could imply different conditions/orientations for a stable wellbore and the overall stability of a wellbore trajectory cannot be studied in a continuous way.

In this thesis a methodology for wellbore trajectory planning/optimization is presented which implements the complete stress tensor obtained from a numerical mechanical earth model [MEM]. This enables analysis of an arbitrary state of stress and precludes the simplification of assuming an ASoS. Stereographic projections predicting stable wellbore orientations at certain locations (starting at the target location in the reservoir) are used to find a suitable and stable overall wellbore trajectory. The continuous stress data from the numerical model is extracted along the planned well trajectory and the safe mud pressure window can be predicted for well trajectories of different well types. The methodology described has been applied to stresses extracted from a synthetic MEM of an offshore field in the Gulf of Mexico [GOM] and best-fit wellbore trajectories and mud pressure windows are presented. An alternative method for wellbore trajectory determination has been used in association with a numerical MEM of a standard anticline structure of a generic CO_2 sequestration site. This methodology assumes that the type of wellbore has been previously determined; therefore the azimuthal angle is the optimized parameter.

1.3. RESEARCH OBJECTIVES AND QUESTIONS

The objective of this study is to address the following question. Can the overall safety of a well be increased by drilling in a specific direction based on stress data obtained from a numerical MEM? If the trajectory can be optimized before the drilling and completion phases have begun, considerable time could be saved, and the chances for negative consequences reduced. The aforementioned question is addressed using the following objectives of this study:

(1) For a given MEM where the wellbore profile is known determine optimized drilling directions for each state of stress using continuous pressure windows.

(2) For a given MEM where the wellbore profile is unknown and freedom of design is given, define an optimization methodology based on the combined use of stereonet projections and continuous pressure windows.

(3) Perform a case study of the optimization methodology for a specific GOM numerical MEM.

2. WELLBORE OPTIMIZATION BACKGROUND THEORY

2.1. INTRODUCTION TO ROCK MECHANICS

The discipline of Rock mechanics studies the mechanical behavior of rock to explain its response to applied loads. Due to the inherent flaws in all rocks, many of the standard mechanical principles must be adjusted before they can be applied to a volume of rock. Rock mechanics is also used to explain rock-rock interaction, rock-fluid interaction, and rock failure. The ability to better understand the aforementioned principles has many applications in the petroleum industry. The main focus of this thesis in regards to rock mechanics is rock failure of the wellbore. Throughout the life of a petroleum well unique rock failure scenarios may occur. In this chapter the most important theoretical concepts used in this thesis are presented. A more thorough description of rock mechanics theory can be found in standard text books (e.g. Jaeger et al., 2007).

2.2. CONCEPT OF STRESS

Deformation of a continuous medium occurs due to body forces and surface forces. Surface forces act on arbitrary surface elements bounding a body. The resistance against surface forces is defined as stress and is expressed by the traction vector $\vec{T}$. The average traction vector (T) is a ratio of a force (F) acting on a surface (A).

$$T = \frac{F}{A} \tag{1}$$

It is common to define the traction vector in terms of limits. This is done by allowing the area over which the traction vector acts to shrink to a point. The traction vector at that point can be defined as follows:

$$\vec{T} = \lim_{dA \to 0} \frac{d\vec{F}}{dA} \tag{2}$$

From the above equation, it can be seen that the traction vector is a function of location in space, and therefore can vary from point to point. Because the traction can vary from point to point, the traction may also vary depending on the plane it is acting on. This leads to the conclusion that the traction vector may also be described in terms of a unit normal vector ($\hat{n}$). In order to simplify this concept Cauchy applied the concept of stress. The stress tensor is of second order and is comprised of nine components. The 'on-in' convention will be used in this text; meaning for any stress component (σ_{ij}) the subscript (i) denotes the axis normal to the surface, and the subscript (j) denotes the direction. For example, (σ_{zy}) is a shear stress acting on the z-plane and in the direction of the y axis. In order to define the stress at a point in three dimensions, an infinitesimally small cube is used (Figure 2.1). In this cube a normal and two shear stresses are acting on each face.

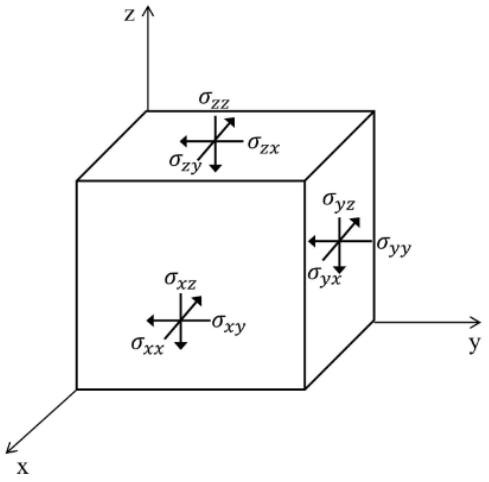

Figure 2.1. Unit cube showing the relative orientation of the stress components acting on each face.

$$\sigma_{ij} = \begin{bmatrix} \sigma_{xx} & \sigma_{xy} & \sigma_{xz} \\ \sigma_{yx} & \sigma_{yy} & \sigma_{yz} \\ \sigma_{zx} & \sigma_{zy} & \sigma_{zz} \end{bmatrix} \tag{3}$$

The conservation of angular momentum results in the stress tensor to be symmetric.

$$\sigma_{ij} = \begin{bmatrix} \sigma_{xx} & \sigma_{xy} & \sigma_{xz} \\ \sigma_{xy} & \sigma_{yy} & \sigma_{yz} \\ \sigma_{xz} & \sigma_{yz} & \sigma_{zz} \end{bmatrix} \tag{4}$$

The detailed derivation of the stress tensor using the theory of Cauchy's tetrahedron is given by Davis and Selvadurai (1996) and results in Cauchy's second law. Cauchy's second law relates the stress tensor to the orientation of an arbitrary plane to obtain the traction vector acting on that plane.

$$T_i = \sigma_{ij} n_j \tag{5}$$

When the normal stresses in a stress tensor are oriented such that that they are directly in line a the local coordinate system where all shear stresses are equal to zero, the stress tensor is known as the principal stress tensor (σ^P). This is usually accomplished by coordinate system transformations. When the stress tensor in question is the principal stress tensor, the normal stresses are also the principal stresses (σ_1, σ_2, and σ_3). The principal stress tensor can be expressed in the following way.

$$\sigma^P = \begin{bmatrix} \sigma_1 & 0 & 0 \\ 0 & \sigma_2 & 0 \\ 0 & 0 & \sigma_3 \end{bmatrix} \tag{6}$$

The mean stress, σ_m, is the arithmetic average of the principal stresses, and represent the isotropic component of the stress tensor. It is the controlling factor for volume change. The mean stress is by**:**

$$\sigma_m = \frac{\sigma_1 + \sigma_2 + \sigma_3}{3} \tag{7}$$

2.3. ELASTIC STRESS – STRAIN RELATIONSHIP

The relationship between stress and strain for any linear elastic material can be given by Hooke's Law. In many engineering applications Hooke's Law in one dimension is sufficient to define a material's linear elastic behavior. However, the field of rock mechanics deals with engineering materials which are acted upon by forces in three dimensions (Jaeger and Cook 1979). For this reason a one dimensional application approach to Hooke's Law would be insufficient. The generalized form of Hooke's Law is:

$$\sigma_{ij} = C_{ijkl}\varepsilon_{kl} \tag{8}$$

where C_{ijkl} is the stiffness tensor which has 81 components and ε_{kl} is strain.

2.3.1. Hooke's Law in Three Dimensions. Rock mechanical applications of Hooke's Law generally include the assumption that the mechanical properties of a rock are isotropic. Assuming isotropic material properties Hooke's Law can be expressed in terms of the principal stresses and strains by using the Lamé parameter and the shear modulus.

$$\sigma_1 = (\lambda + 2G)\varepsilon_1 + \lambda\varepsilon_2 + \lambda\varepsilon_3 \tag{9}$$

$$\sigma_2 = (\lambda + 2G)\varepsilon_2 + \lambda\varepsilon_1 + \lambda\varepsilon_3 \tag{10}$$

$$\sigma_3 = (\lambda + 2G)\varepsilon_3 + \lambda\varepsilon_1 + \lambda\varepsilon_2 \tag{11}$$

2.3.2. Pore Pressure and Effective Stress. The stresses which have been previously discussed are known as total stresses (σ_T). The effective stress (σ') is the result of subtracting the pore pressure (P_p) from the total stress (Terzagi, 1936).

$$\sigma' = \sigma_T - P_P \tag{12}$$

2.3.3. Mohr's Circle. Mohr (1914) introduced a circular diagram which represents the state of stress at a point. The circle is calculated using a principal stress system, where the shear stress equals to zero. The Mohr-Circle diagram also utilizes a failure angle θ which is defined as the angle between the maximum principal stress and the normal vector of the plane of interest. One limitation of the traditional Mohr-Circle diagram is the lack of influence from the intermediate principal stress. The fundamental stress equations used to define a Mohr-Circle are as follows:

$$\sigma_n = \frac{\sigma_1 + \sigma_3}{2} + \frac{\sigma_1 - \sigma_3}{2}\cos 2\theta \tag{13}$$

$$\tau = \frac{\sigma_1 - \sigma_3}{2}\sin 2\theta \tag{14}$$

To construct a Mohr-Circle diagram, the principal stresses σ_1 and σ_3 are plotted along the x-axis in an x-y Cartesian coordinate system where the x-axis represents normal stresses, and the y-axis represents shear stresses. A circle with diameter $\sigma_1 - \sigma_3$ can then be plotted. For a plane with a known orientation and traction, a Mohr-Circle diagram can be used to determine what the stresses would be at the original, or arbitrary, orientation. Figure 2.2 shows a typical Mohr-Circle diagram.

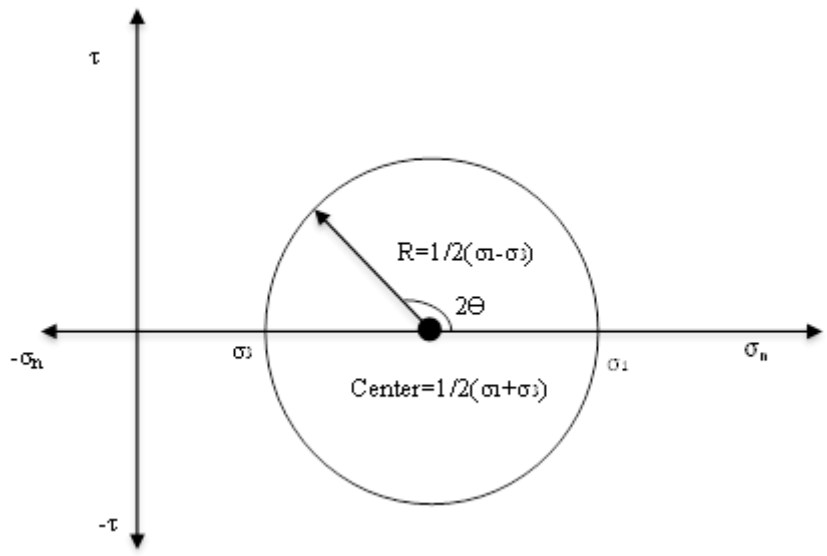

Figure 2.2. Mohr-Circle diagram for a plane acted upon by an arbitrary stress tensor.

2.4. ROCK STRENGTH AND FAILURE

Failure in rocks occurs when the stresses present in a rock are large enough to overcome the rock's strength properties and cause permanent deformation. The two main types of rock failure are shear failure and tensile failure. For many rock mechanics applications rock failure is seen as a negative outcome, but there are situations where rock failure is purposefully induced. For example, shear failure in the borehole in the form of breakouts can cause delays in the drilling process, while tensile failure induced by hydraulic forces can help to stimulate production. By understanding rock failure it becomes apparent that we can minimize the occurrence of detrimental failure, and maximize the effectiveness of intentional failure.

The three modes of rock failure defines Mode I fractures as opening, Mode II fractures as sliding, and Mode III fractures as scissoring (Figure 2.3; Fjaer et al., 2008). A Mode I fracture is characterized by extensional opening by tensile stresses perpendicular to a fracture plane; no shear components are present in Mode I fracturing. Mode II fractures are shear planes where the tractions are parallel to the fracture surface and the direction of propagation. Mode III fractures exhibit lateral shear and are often characterized by scissor type motion perpendicular to the direction of fracture

propagation. In many real situations the actual mode of fracture which is seen will be a mixed mode fracture (Fjaer, et al., 2008).

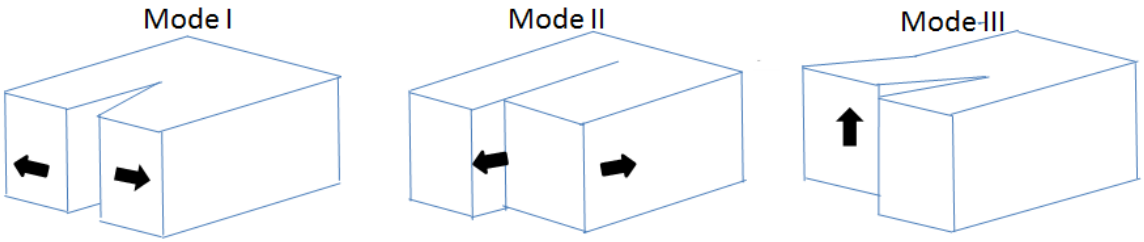

Figure 2.3. Three commonly accepted modes of rock fractures. Mode I fractures exhibit rock splitting, Mode II fractures are sliding, and Mode III fractures are caused by a scissoring motion.

2.4.1. Shear Failure. Shear failure can occur on any failure plane in a rock when the stresses exceed the rock strength parameters. When shear failure occurs on a plane, the portion of rock on either side of the plane will move relative to the other block. The motion of the blocks is resisted by a frictional force which is present on the plane and dependent on the magnitude of the stress acting on the plane. Mohr further hypothesized that the critical shear stress (τ_{max}) must then be a function of the normal stresses which are acting on the plane of failure:

$$\tau_{max} = f(\sigma_n) \tag{15}$$

In a Mohr-Circle diagram the above equation is known as a failure criterion. Many failure criterions exist for differing rock types and scenarios. Some failure criteria display linear relationships, while others are of higher order. For all failure criteria if the stresses are such that the Mohr-Circle comes into contact with the failure criteria, failure will occur. Examples of this are shown in the following sections.

2.4.2. Tensile Failure. Tensile failure in rocks occurs when the effective stresses acting on a rock exceed the tensile strength ($-T_o$) of the rock. For most rock samples, the magnitude of the tensile strength is commonly in the range of 1-10 MPa (Kocker, et al., 2008). This low magnitude is mainly due to the preexistence of tensile fracture planes in the rock where were formed at deposition. For any rock sample the tensile failure criterion is as follows:

$$\sigma_T = -T_o \tag{16}$$

where σ_T is the tensile stress in a rock.

More specifically, if the rock sample in question contains isotropic rock properties, the above criterion may be simplified to the following form.

$$\sigma_3 = -T_o \tag{17}$$

On a Mohr-Circle diagram this criterion can be readily shown (Figure 2.4).

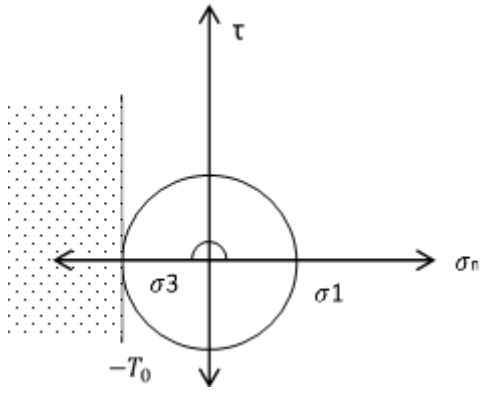

Figure 2.4. Mohr-Circle scenario in which tensile failure of a rock would occur.

2.4.3. Mohr-Coulomb Failure. The Mohr-Coulomb failure criterion is used to determine the onset of shear, or compressive, failure. In this criterion, compressive failure in a wellbore occurs when the stresses at the wellbore wall exceed the

compressive strength of the rock at that location in the wellbore (Aadnøy et al., 2005). When this shear failure is incurred at the wellbore wall it is termed a breakout or wellbore collapse. The Mohr-Coulomb criterion is one of the most frequently used tools to predict the onset of shear failure at the wellbore wall. This criterion is also one of the most conservative failure criterion; meaning that it will predict failure earlier than most other models as shown by Nawrocki (2010). The conservative nature of this failure criterion makes it ideal in determining the earliest possible onset of damage in the wellbore.

The Mohr-Coulomb failure criterion assumes a linear relationship between the shear stress and the normal stress:

$$\tau = S_o + \sigma_n \tan\varphi \tag{18}$$

where τ is the shear stress, S_o is the cohesion of the rock, σ_n is the normal stress on the plane of failure, and φ is the internal angle of friction of the rock. The equation is also commonly written in the following form:

$$\tau = S_o + \mu\sigma_n \tag{19}$$

where μ is the coefficient of friction and is given as:

$$\mu = \tan\varphi \tag{20}$$

Both the cohesion and the internal angle of friction are rock strength properties which vary among different rock types. For a typical solid rock a value of 30^o is commonly used for the internal angle of friction (Fjaer et al., 2008).

The Mohr-Coulomb failure criteria also assumes that the intermediate principal stress has no influence on rock failure, therefore the Mohr circle used for failure is defined using only σ_1 and σ_3. Shear failure will occur at the point where the Mohr circle intersects the Mohr-Coulomb failure line (commonly referred to as the Mohr-Coulomb Failure Envelope). The initial point of failure is shown below (Figure 2.5).

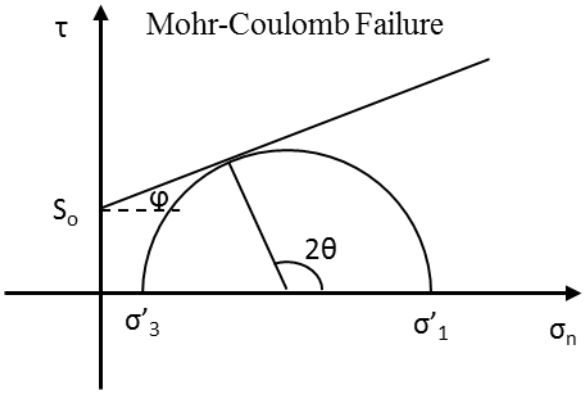

Figure 2.5. Mohr-Circle depicting the point of initial shear failure for an intact rock using the Mohr-Coulomb failure criterion.

By investigating the same scenario in more detail, the exact point at which failure would occur can be determined (Figure 2.5). From equations 14 and 15 the values of the shear and normal stresses at that point can be determined. θ is the orientation of the failure plane and can be related to the internal angle of friction as follows:

$$\theta = \frac{1}{2}\varphi + \frac{\pi}{4} \tag{21}$$

Due to the constraints of the internal angle of friction ranging from 0^o-90^o, the failure angle must range from 45^o-90^o. The Mohr-Coulomb criterion indicates that orientations of shear failure are independent of the state of stress if the internal angle of friction is constant. For this scenario, the failure angle is commonly defined as the angle between the normal of the failure plane and the direction of the maximum principal stress (Figure 2.6).

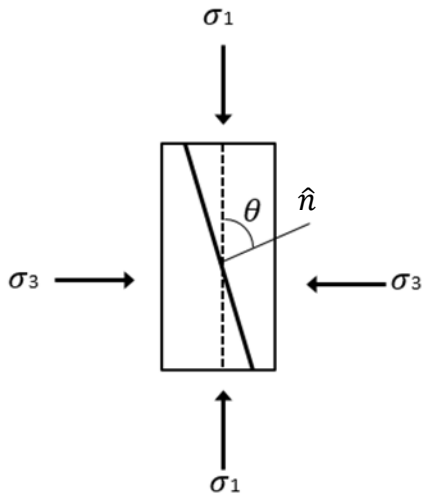

Figure 2.6. Definition of the failure angle θ for an arbitrarily oriented plane of failure.

At the point of failure the Mohr Coulomb failure criterion can be expressed by the principal stresses σ_1 and σ_3 (Jaeger and Cook 2007):

$$\sigma'_1 = 2\frac{S_o \cos\varphi}{1-\sin\varphi} - \frac{1+\sin\varphi}{1-\sin\varphi}\sigma'_3 \tag{22}$$

From the above equation the minimum mud pressure for wellbore stability analysis can be calculated (Lee et al., 2011).

2.5. IDEALIZED STRESSES IN THE SUBSURFACE

2.5.1. E.M. Anderson's Theory of Faulting. One of the most common assumptions used in geomechanical analyses is that of an Andersonian state of stress (ASoS). The Andersonian stress theory uses the assumption that the surface of the Earth is a free surface (no shear stresses are present) and that one principal stress, σ_v, is vertical, and the two other principal stresses are horizontal. The two horizontal principal stresses are distinguished from one another by their magnitude where the maximum horizontal stress is σ_H and the minimum horizontal stress is σ_h. If an ASoS is assumed, three unique stress regimes can be defined based on the magnitude of the vertical stress relative to the magnitude of the horizontal stresses.

If the vertical stress is the maximum principal stress (σ_1), the stress regime is extensional, or normal. In an extensional stress regime steeply dipping normal faults are created in order to compensate for the extension. If the vertical stress is the intermediate principal stress (σ_2), the stress regime is strike-slip. In a strike-slip stress regime two blocks of crust move horizontally along a vertical, or near vertical, fault. If the vertical stress is the minimum principal stress (σ_3), the stress regime is compressional. In this stress regime the crust is being compressed by the relatively larger magnitudes of the horizontal stresses. Low angle reverse faults are typical in compressional stress regimes (Zoback 2007). The stress tensors and block diagrams (Figure 2.7) which are associated with an Andersonian stress regime assumption are as follows:

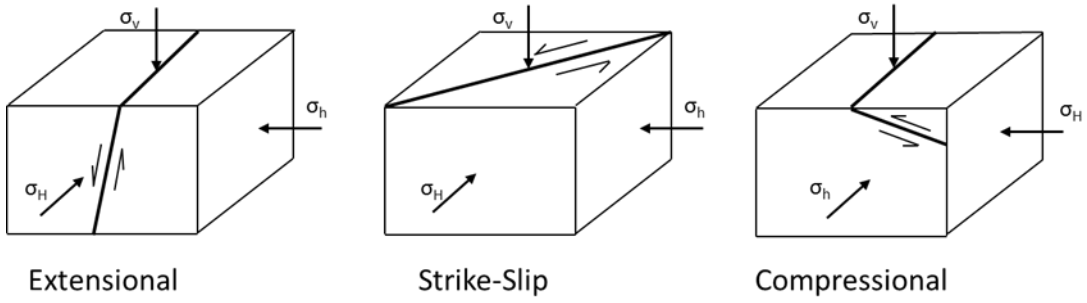

Figure 2.7. Block diagrams representing the three possible stress regimes for an ASoS.

$$\boldsymbol{\sigma}_{\boldsymbol{ext}} = \begin{bmatrix} \sigma_v & 0 & 0 \\ 0 & \sigma_H & 0 \\ 0 & 0 & \sigma_h \end{bmatrix} \tag{23}$$

$$\boldsymbol{\sigma}_{\boldsymbol{ss}} = \begin{bmatrix} \sigma_H & 0 & 0 \\ 0 & \sigma_v & 0 \\ 0 & 0 & \sigma_h \end{bmatrix} \tag{24}$$

$$\boldsymbol{\sigma}_{\boldsymbol{comp}} = \begin{bmatrix} \sigma_H & 0 & 0 \\ 0 & \sigma_h & 0 \\ 0 & 0 & \sigma_v \end{bmatrix} \tag{25}$$

The vertical stress is caused by the weight of the overburden formations and can be calculated from data gathered from the density well log.

$$\sigma_v = \int_{z_1}^{z_2} \rho_{(z)} g dz \tag{26}$$

where z is a depth, g is gravitational acceleration, and the density is a function of depth.

Similarly if pore pressure is assumed hydrostatic it can be calculated from the integration of water density (ρ_w) with respect to depth.

$$P_p = \int_{z_1}^{z_2} \rho_{w(z)} g dz \tag{27}$$

2.6. WELLBORE STATE OF STRESS

2.6.1. Analytical Solution to Wellbore Stresses. Before drilling, the state of stress in the subsurface is in equilibrium and in most situations an Andersonian state of stress exists. During the drilling process, solid material is removed and the loads which were acting on the material must be compensated for by the adjacent rock. This compensation is achieved by a redistribution of the stresses concentrated around the wellbore. The linear elastic solution describing this phenomenon of radial and tangential stress redistribution was first derived by Kirsch in 1898 and later extended by Zhang et al. (2006) to account for pore pressure and fluid pressure in the wellbore. The stress distribution in the cylindrical coordinate system of a wellbore along the σ_{33}-direction is given by:

$$\begin{aligned} \sigma'_{rr} = {} & \frac{(\sigma_{11} + \sigma_{22} - 2P_p)}{2}\left(1 - \frac{R_w^2}{r^2}\right) + \frac{(\sigma_{11} - \sigma_{22})}{2}\left(1 + \frac{R_w^2}{r^2} - \frac{3R_w^4}{r^4}\right)\cos(2\theta) \\ & + v\sigma_{12}\left(1 + 3\frac{R_w^4}{r^4} - 4\frac{R_w^2}{r^2}\right)\sin(2\theta) + (P_m - P_p)\frac{R_w^2}{r^2} \end{aligned} \tag{28}$$

$$\sigma'_{\theta\theta} = \frac{(\sigma_{11} + \sigma_{22} - 2P_p)}{2}\left(1 + \frac{R_w^2}{r^2}\right) - \frac{(\sigma_{11} - \sigma_{22})}{2}\left(1 + \frac{3R_w^4}{r^4}\right)\cos(2\theta) - \mathrm{v}\sigma_{12}\left(1 + 3\frac{R_w^4}{r^4}\right)\sin(2\theta) - (P_m - P_p)\frac{R_w^2}{r^2} \quad (29)$$

$$\sigma'_{zz} = \sigma_{33} - P_p - v\left[\frac{2R_w^2}{r^2}(\sigma_{11} - \sigma_{22})co\,s(2\theta) + 4\sigma_{12}\frac{R_w^2}{r^2}\sin 2\theta\right] \quad (30)$$

$$\tau'_{r\theta} = \frac{(\sigma_{11} - \sigma_{22})}{2}\left(1 - 3\frac{R_w^4}{r^4} + 2\frac{R_w^2}{r^2}\right)\sin 2\theta + \sigma_{12}\left(1 - 3\frac{R_w^4}{r^4} + 2\frac{R_w^2}{r^2}\right)\cos 2\theta \quad (31)$$

$$\tau'_{\theta z} = (-\sigma_{13}\sin\theta + \sigma_{23}\cos\theta)\left(1 + \frac{R_w^2}{r^2}\right) \quad (32)$$

$$\tau'_{rz} = (\sigma_{23}\sin\theta + \sigma_{13}\cos\theta)\left(1 - \frac{R_w^2}{r^2}\right) \quad (33)$$

where σ'_{rr} , $\sigma'_{\theta\theta}$, σ'_{z} , $\tau'_{r\theta}$, $\tau'_{\theta z}$ and τ'_{rz} are the radial stress, hoop stress, vertical stress, shear stress in the r-θ plane, shear stress in the θ-z plane, and shear stress in the r-z plane respectively; R_w is the wellbore radius, and r is the distance from wellbore center; and θ is the angle with respect to the direction of the maximum horizontal stress. P_m represents the internal wellbore fluid pressure and P_p is the formation pore pressure.

For a vertical wellbore in an ASoS if a constant pore pressure and Biot coefficient of 1 is assumed, the effective stresses around the borehole for a vertical well is given by:

$$\sigma'_{rr} = \frac{(\sigma_H + \sigma_h - 2P_p)}{2}\left(1 - \frac{R_w^2}{r^2}\right) - \frac{(\sigma_H - \sigma_h)}{2}\left(1 - \frac{R_w^2}{r^2} + \frac{3R_w^4}{r^4}\right)\cos(2\theta) + (P_m - P_p) \quad (34)$$

$$\sigma'_{\theta\theta} = \frac{(\sigma_H + \sigma_h - 2P_p)}{2}\left(1 + \frac{R_w^2}{r^2}\right) - \frac{(\sigma_H - \sigma_h)}{2}\left(1 + \frac{3R_w^4}{r^4}\right)\cos(2\theta) - (P_m - P_p) \quad (35)$$

$$\sigma'_{zz} = \sigma_v - P_p - v\frac{2R_w^2}{r^2}(\sigma_H - \sigma_h)cos(2\theta) \quad (36)$$

$$\tau'_{r\theta} = \frac{(\sigma_H - \sigma_h)}{2}\left(1 - \frac{2R_w^2}{r^2} - \frac{3R_w^4}{r^4}\right)sin(2\theta) \quad (37)$$

$$\tau_{rz} = \tau_{\theta z} = 0 \quad (38)$$

where σ_H , σ_h , and σ_z are the maximum horizontal, minimum horizontal, and the vertical stress, respectively;

It is common for the above equations to be expressed at intervals of $\theta = 90^o$ and at the wellbore wall (where $r = R_w$). At $\theta = 90^o$ and 270^o, the magnitude of the hoop stress around the borehole reaches its maximum value. At these locations shear failure in the form of borehole breakouts may occur if the resulting hoop stress is greater than the compressive strength of the rock. At $\theta = 0^o$ and 180^o, the magnitude of the hoop stress around the borehole reaches its minimum value. At these locations tensile failure may occur. The simplified expressions for the hoop and radial stresses at the wellbore wall as presented by Zoback (2007) are given by:

$$\sigma'_{\theta\theta} = \sigma_h + \sigma_H - 2(\sigma_H - \sigma_h)\cos 2\theta - 2P_p - \Delta P \quad (39)$$

$$\sigma'_{rr} = \Delta P \quad (40)$$

$$\Delta P = P_m - P_p \quad (41)$$

$$\sigma_{\theta\theta}^{min} = 3\sigma_h - \sigma_H - 2P_p - \Delta P \quad (42)$$

$$\sigma_{\theta\theta}^{max} = 3\sigma_{\mathrm{H}} - \sigma_{\mathrm{h}} - 2P_p - \Delta P \tag{43}$$

In order to resolve the borehole state of stress for an arbitrarily oriented wellbore it is convenient to define a coordinate system (x', y', z') using inclination (*i*) and azimuth (α) for a certain point along the well path (Figure 2.8).

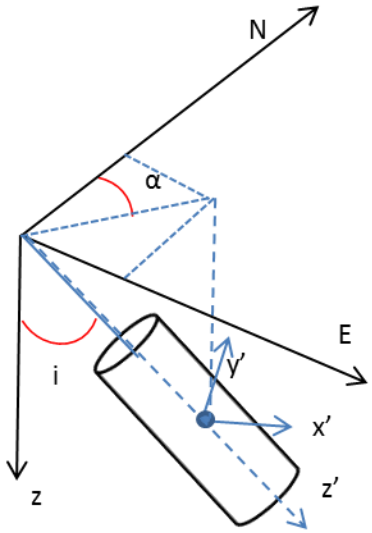

Figure 2.8. Orientation of wellbore coordinate system. The azimuth is measured from North toward the East, and the angle of inclination is measured from the vertical to the new wellbore axis.

In the new coordinate system the z' axis coincides with the wellbore axis, the x' axis acts toward the bottom side of the wellbore, and the y' axis acts horizontally in the plane perpendicular to the wellbore axis (Figure 2.8). Using this coordinate system the stress tensor (Equation 5) can be transformed using the following transformation matrix (Peska and Zoback 1995):

$$\mathbf{D} = \begin{bmatrix} -\cos(\alpha)\cos(i) & -\sin(\alpha)\cos(i) & \sin(i) \\ \sin(\alpha) & -\cos(\alpha) & 0 \\ \cos(\alpha)\sin(i) & \sin(\alpha)\sin(i) & \cos(i) \end{bmatrix} \tag{44}$$

In order to obtain the stress tensor for the new wellbore coordinate system the following operation is performed (Peska and Zoback 1995):

$$\sigma'_w = D\sigma'_{ij}D^T = \begin{bmatrix} \sigma_{x'x'} & \sigma_{x'y'} & \sigma_{x'z'} \\ \sigma_{x'y'} & \sigma_{y'y'} & \sigma_{y'z'} \\ \sigma_{x'z'} & \sigma_{y'z'} & \sigma_{z'z'} \end{bmatrix} \tag{45}$$

where σ'_{ij} represents the complete effective stress tensor, σ_w is the wellbore stress tensor, and D^T is the transpose of the transformation matrix.

From the new wellbore stress tensor (σ'_w) the effective stresses at the wellbore wall ($r=R_w$) for a wellbore along the new $\sigma_{z'z'}$ direction can be calculated using the Kirsch solution (Equations 29-34) which is simplified as:

$$\sigma'_{\theta\theta} = \sigma_{z'z'} - 2\left(\sigma_{x'x'} - \sigma_{y'y'}\right)\cos 2\theta + 4\sigma_{x'y'}\sin 2\theta - \Delta P \tag{46}$$

$$\sigma'_{rr} = \Delta P \tag{47}$$

$$\sigma'_{zz} = \sigma_{z'z'} - 2v\left(\sigma_{x'x'} - \sigma_{y'y'}\right)\cos 2\theta + 4v\sigma_{x'y'}\sin 2\theta \tag{48}$$

$$\tau'_{\theta z} = 2(\sigma_{y'z'}\cos\theta - \sigma_{x'z'}\sin\theta) \tag{49}$$

where $\sigma'_{\theta\theta}$ is the effective hoop stress, θ is the angle around the wellbore measured from x' toward y', ΔP is the difference between pore pressure and the mud pressure, σ'_{rr} is the effective radial stress, and υ is the Poisson's ratio. This accounts for the utilization of the complete stress tensor from the FE models in Chapter 4 used for the wellbore trajectory optimization procedure.

From equations 47-50 the principal stresses around the wellbore can be calculated:

$$\sigma'_{tmax} = \frac{1}{2}[\sigma_{zz} + \sigma_{\theta\theta} + \sqrt{(\sigma_{\theta\theta} - \sigma_{zz})^2 + 4\tau_{\theta z}^2}] \quad (50)$$

$$\sigma'_{tmin} = \frac{1}{2}[\sigma_{zz} + \sigma_{\theta\theta} - \sqrt{(\sigma_{\theta\theta} - \sigma_{zz})^2 + 4\tau_{\theta z}^2}] \quad (51)$$

$$\sigma'_{rr} = \Delta P \quad (52)$$

2.6.2. Deviated Wellbores. A deviated wellbore is any wellbore which does not lie entirely along the vertical axis (Zare-Reisabadi et al., 2012). Deviated wellbores are defined by an angle of inclination and an azimuthal angle (Figure 2.8). The angle of inclination is the deviation of the wellbore from the vertical axis and ranges from 0^o-90^o. The azimuthal angle is the direction of the borehole axis with respect to north. The azimuth ranges from 0^o-360^o where 0^o is north and the angle increases clockwise (Zoback 2007; Barton et al., 1997). In this study four unique wellbore profiles will be used, three of which contain deviations from vertical.

2.6.2.1 Type I wellbore. The Type I wellbore profiles which will be used in this thesis are vertical wellbores. The information needed to construct a Type I wellbore is simply the surface location coordinates and the target location coordinates. Because there are no bends or curves in a Type I wellbore the measured depth [MD] which is the total length of the well from surface to target will be equal to the true vertical depth [TVD] of the wellbore. A schematic drawing of the wellbore types is shown in Figure 2.9.

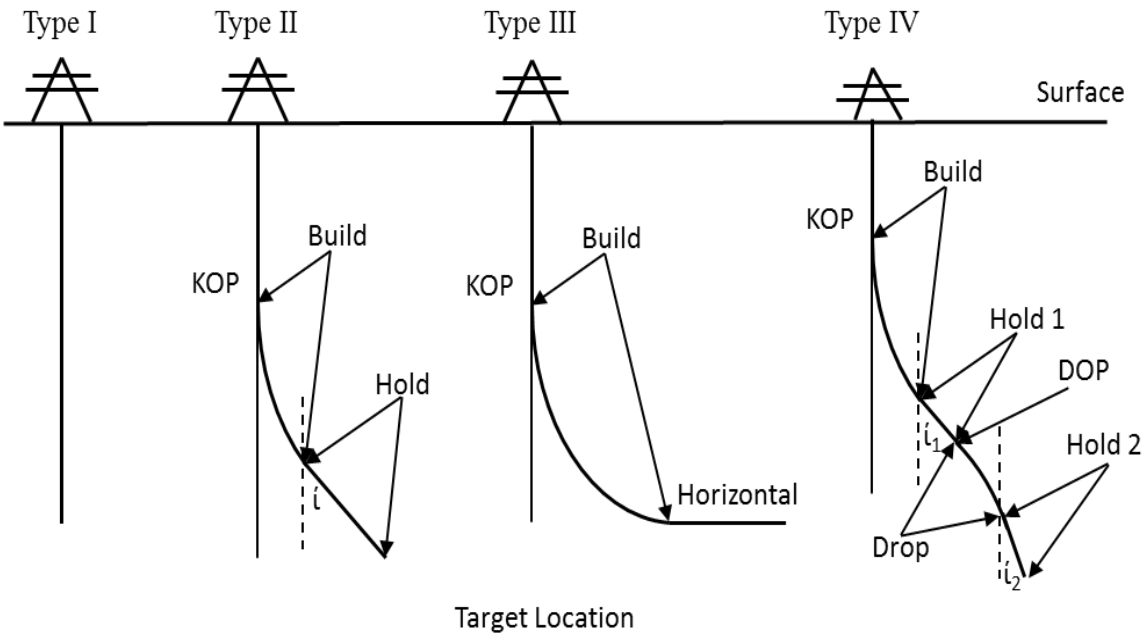

Figure 2.9. Profile view depicting the shape and important features for each individual well type.

2.6.2.2 Type II wellbore. The Type II wellbore profiles (Figure 2.9) which will be used consist of a vertical section, a build section, and a hold section. The vertical section of the well extends from the surface location down to the depth of the kick off point [KOP]. After the KOP has been reached, the well will enter a build section where an angle will be created between the axis of the wellbore and vertical. The build section of the wellbore continues until a pre-determined value for the inclination has been achieved. Once this final inclination value is achieved, the angle is held constant creating the hold section of the wellbore profile. The hold section continues until the target location is achieved.

2.6.2.3 Type III wellbore. The Type III wellbore profile (Figure 2.9) consists of three sections; a vertical section, a build section, and a horizontal section. A Type III profile is actually a special case of the Type II wellbore profile where the final inclination angle of the build section is 90^{o}. A final inclination of 90^{o} implies that the hold section of the wellbore is perfectly horizontal.

2.6.2.4 Type IV wellbore. The final wellbore profile is a Type IV (Figure 2.9), or 'S' shaped**,** wellbore profile. This wellbore consists of a vertical section, a build section, an initial hold section, a drop section, and a final hold section. In some cases the hold sections are unnecessary and can be omitted if necessary. The Type IV wellbore profile is identical to the Type II profile until the drop off point [DOP] is reached. This point is located at the end of the initial hold section and is where the inclination angle begins to drop, or moves back toward vertical. Once the inclination required to reach the target location is met, the wellbore inclination is held constant for the final hold section.

2.7. WELLBORE FAILURE AND WELLBORE STABILITY

2.7.1. Borehole Failure. Failure at the wellbore wall (Figure 2.10) can occur as either shear or tensile failure. Failure of the borehole wall is directly related to the magnitude of the principal stresses at the borehole wall; the hoop and radial stress. As Equation 29 shows, the hoop stress varies with respect to the angle θ along the borehole wall (Figure 2.11). The cos2θ dependence of the hoop stress results in a hoop stress maximum at $\theta=90^o$ and a hoop stress minimum at $\theta=0^o$. At $\theta=90^o$ the hoop stress can reach large compressive stress magnitudes (i.e. $\sigma_1=\sigma_{\theta\theta}=3S_H-S_h-P_i-P_p$) and as the radial stress is comparatively small (i.e. $\sigma_3=\sigma_{rr}=Pi-Pp$) large differential stresses can occur resulting in shear failure of the wellbore wall. This shear failure results in borehole breakouts and rock fragments/spallings (Figure 2.10) collapse into the wellbore. This damage can cause stuck pipe and increase the amount of time it would take to drill a well. The minimum mud pressure resulting in the onset of shear failure is termed collapse pressure. For this reason the density of the drilling fluid should always be kept great enough such that the mud pressure is greater than the collapse pressure.

At $\theta=0^o$ the hoop stress has a minimum and may reach tensile stress magnitudes (i.e. $\sigma_3=\sigma_{\theta\theta}=3S_h-S_H-P_i-P_p$) and exceed the tensile strength of the rock. This generates tensile fractures at the wellbore wall. When this occurs during the drilling process it is termed drilling induced tensile failure (DITF). The main consequence of DITF is lost circulation due to the fluid flow pathways which are created. Figure 2.10 depicts shear and tensile failure at the wellbore wall for a well drilled in an ASoS.

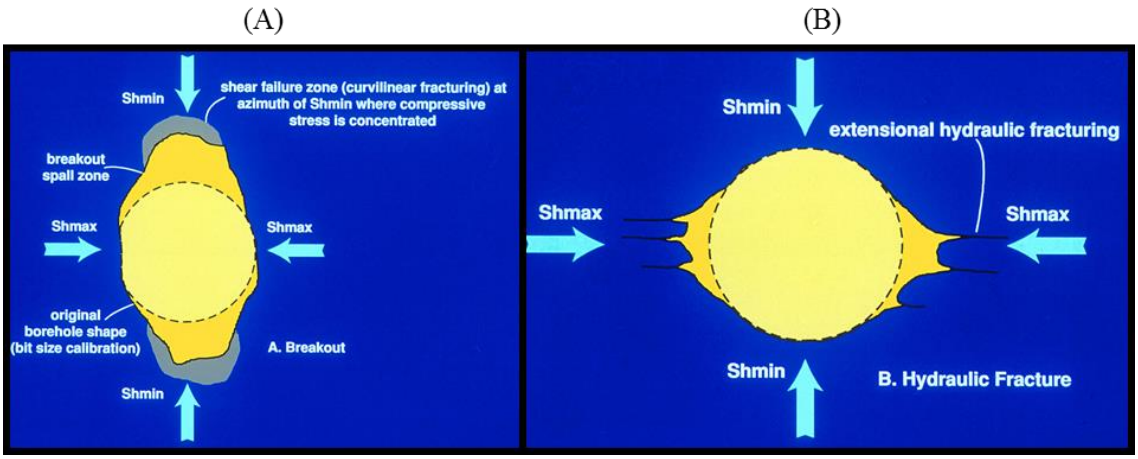

Figure 2.10. Graphical depiction of shear failure at the borehole wall (A). Graphical depiction of tensile failure at the borehole wall (B).

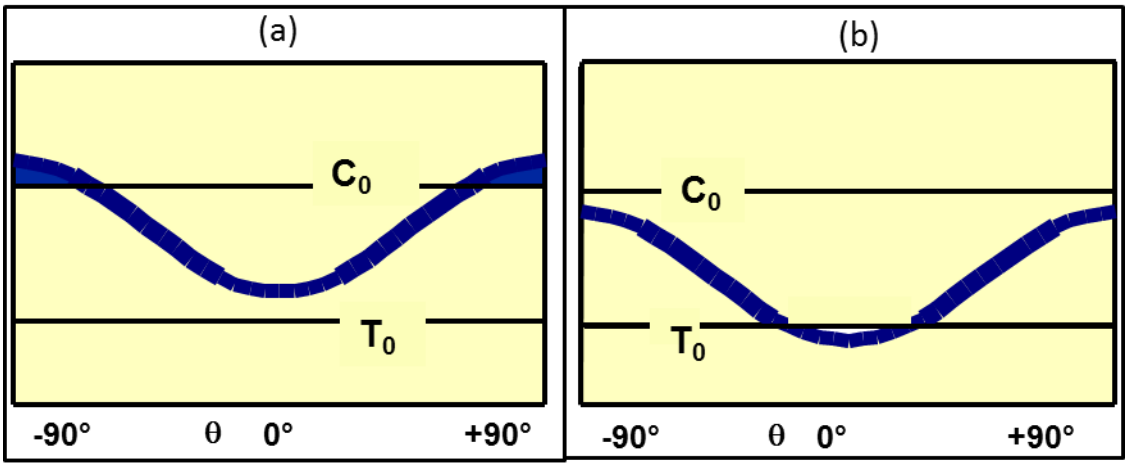

Figure 2.11. Graph showing the hoop stress with respect to theta around the wellbore. (a) shows shear failure occurring at maximum hoop stress, and (b) shows tensile failure at values of minimum hoop stress.

2.7.2. Influences of Pore Pressure and Mud Pressure. The influence of pore pressure and mud pressure on a Mohr's Circle of the wellbore state of stress is fundamental for the understanding of wellbore failure. The existence of pore pressure results in a leftward translation of the Mohr's Circle. This translation results in a scenario more likely to fail. Although the original in-situ stresses and pore pressure cannot be

influenced during the drilling process; it is important to understand how changes in pore pressure could influence the safety of a well either after reservoir depletion or during injection. However this represents a complex phenomena changing the differential stress (Altmann et al., 2010) and is dependent on a variety of parameters and hence not the scope of this study.

From Equations 47 and 48 it can be seen that mud pressure also has an effect on wellbore stability. The mud acts as a fluid pressure induced on the wellbore wall. This fluid pressure causes a decrease in the hoop stress while increasing the radial stress. The overall effect is that the size of the Mohr's Circle becomes smaller, and wellbore stability is improved. However, if the mud pressure is too high the hoop stress may enter the tensile regime and a hydraulic fracture may occur. If the mud pressure is too low, the hoop stress is large, and shear failure may occur. Figure 2.10 shows two failure scenarios. Figure 2.10A showing how a state of stress initially stable may fail in shear if the mud pressure is reduced and Figure 2.12B showing how a state of stress which is initially safe can be caused to fail in tension by increasing the mud pressure.

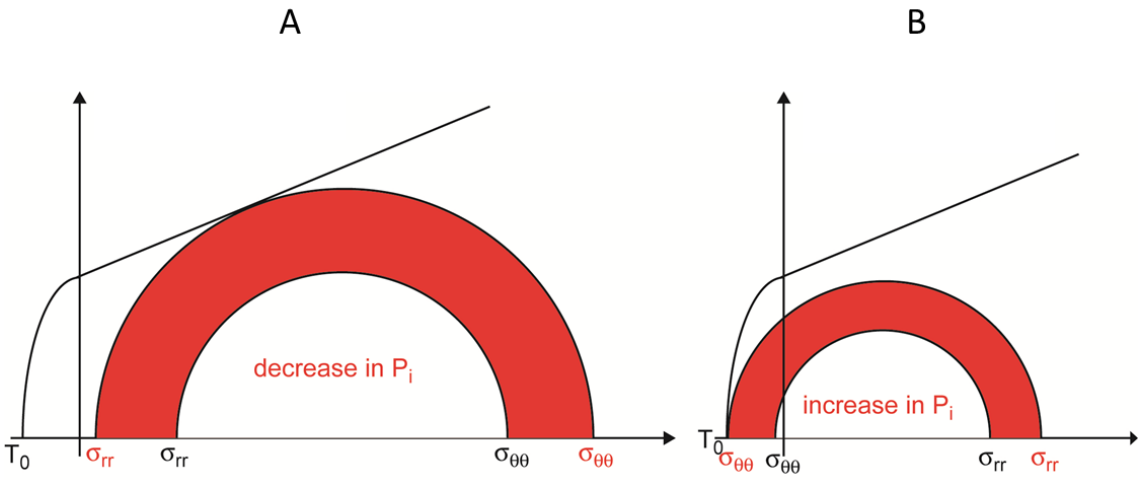

Figure 2.12. (A) Decrease in mud pressure causes an increase in the size of the Mohr Circle which may lead to shear failure. (B) Increase in mud pressure will reduce the stresses possibly leading to tensile failure.

When the hoop stress is large such that the wellbore fails in shear (Figure 2.10A) the integrity of the wellbore is compromised and collapse occurs. Figure 2.10A shows that for a certain mud pressure shear failure at the wellbore will be induced. This mud pressure is then the minimum mud pressure which must be exerted on the wellbore wall unless collapse will occur; it is termed the collapse pressure. In the same fashion Figure 2.10B shows that if the mud pressure is increased tensile failure may occur at the wellbore wall. The mud pressure which would be required to initiate tensile failure is termed the breakdown pressure. These pressures are used to define a safe operational window of pressures which can be used to safely drill a well.

2.7.3. Pressure Window. The pressure window (also termed operational window; Figure 2.13) defines the safe operating pressures to avoid wellbore failure. To ensure wellbore stability, the mud pressure should be kept higher than the formation pressure to keep formation fluids from entering the wellbore and higher than the collapse pressure. If the mud pressure becomes lower than the collapse pressure shear failure at the wellbore wall will occur. The lower limit of the pressure window therefore is either the formation pressure or the collapse pressure. The lower of the two entities is chosen to ensure no damage incurs. This scenario occurs when the hoop stress is at its maximum value.

The upper limit of the pressure window is defined by the formation breakdown pressure (or fracture gradient). The formation breakdown pressure is the maximum mud pressure which can be used before the onset of tensile failure at the wellbore wall. Tensile failure occurs when the hoop stress acting on the wellbore wall reaches values lower than the tensile strength of the rock.

Another use of the pressure window is to locate the positions of casing points. Casing is used in order to protect the overlying formation from being subjected to large mud pressures during the drilling of deeper sections of the wellbore. If no casing strings were placed downhole, the overlying formations may be fractured and lost circulation may occur. Casing sections are also placed in order to protect any fresh water zones from being contaminated by the drilling fluid.

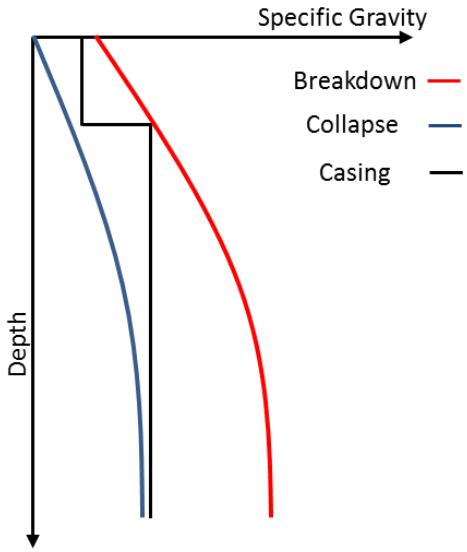

Figure 2.13. Exemplary operational window defined with the breakdown gradient as the upper limit and the collapse gradient as the lower limit of safe operational conditions. Using this, the locations for casing sections can be determined.

2.7.4. Stereonet Projections. A stereonet projection (Zoback 2007; Figure 2.14) is a graphical representation to display the relationship of a single variable versus two independent variables. For the purposes of wellbore stability analyses stereonet projections are used to display stress calculations (the dependent variable) against two separate angles; the azimuth and inclination of the plane of interest (Figure 2.9). The circumferential variable is the azimuth, the concentric circles are inclination angles ranging from 0^o at the center to 90^o at the outer boundary, and the color scale represents a stress magnitude.

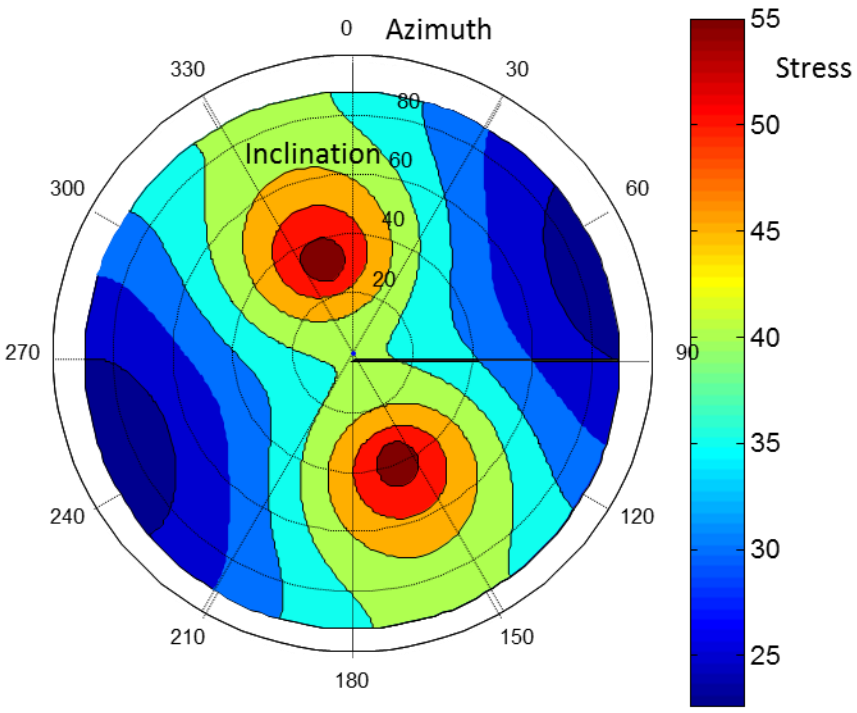

Figure 2.14. Exemplary stereonet projection of a stress magnitude plotted against azimuth and inclination.

The variable which is used in this study for the optimization approach (explained fully in section 3.6) is the difference between the breakdown and the collapse pressure, P_{diff}. This variable represents the width of the mud pressure window for any arbitrary stress tensor. If this is done for every combination of azimuth and inclination, a stereonet projection can be created. Figure 2.15 displays how this operation is performed in stereonets.

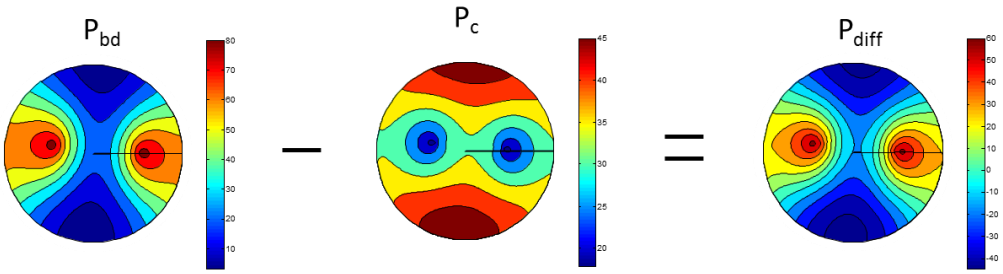

Figure 2.15. Calculation of the P_{diff} stereonet using the stereonets of collapse pressure and breakdown pressure.

3. WELLBORE OPTIMIZATION TECHNICAL APPROACH

3.1. THE EQUATIONS OF EQUILIBRIUM

In order to determine the state of stress for a body that is subjected to a certain set of loads a set of three partial differential equations has to be solved. For the field of rock mechanics where accelerations are negligible these equations are termed the equations of (static) equilibrium. These equations can be derived by applying the conservation of linear and angular momentum to the rock. Figure 2.1 is used to determine the equation of motion for a body with differential volume in a rectangular coordinate system. The detailed derivation of the equations of equilibrium can be found in Jaeger et al. (2007).

$$\frac{\partial \sigma_{xx}}{\partial x} + \frac{\partial \sigma_{yx}}{\partial y} + \frac{\partial \sigma_{zx}}{\partial z} + B_x = 0 \tag{53}$$

$$\frac{\partial \sigma_{xy}}{\partial x} + \frac{\partial \sigma_{yy}}{\partial y} + \frac{\partial \sigma_{zy}}{\partial z} + B_y = 0 \tag{54}$$

$$\frac{\partial \sigma_{xz}}{\partial x} + \frac{\partial \sigma_{yz}}{\partial y} + \frac{\partial \sigma_{zz}}{\partial z} + B_z = 0 \tag{55}$$

where the subscripts on the stresses follow the on-in convention addressed previously; $\partial x, \partial y,$ and ∂z are the lengths of each side of the cube; and B_x, B_y, and B_z are the body forces.

Similarly the equilibrium equations can be derived for a cylindrical coordinate system and are given by the following.

$$\frac{\partial \sigma_{rr}}{\partial r} + \frac{1}{r}\frac{\partial \sigma_{\theta r}}{\partial \theta} + \frac{\partial \sigma_{zr}}{\partial z} + \frac{\sigma_{rr} - \sigma_{\theta\theta}}{r} + B_r = 0 \tag{56}$$

$$\frac{\partial \sigma_{r\theta}}{\partial r} + \frac{1}{r}\frac{\partial \sigma_{\theta\theta}}{\partial \theta} + \frac{\partial \sigma_{z\theta}}{\partial z} + \frac{2\sigma_{r\theta}}{r} + B_\theta = 0 \tag{57}$$

$$\frac{\partial \sigma_{rz}}{\partial r} + \frac{1}{r}\frac{\partial \sigma_{\theta z}}{\partial \theta} + \frac{\partial \sigma_{zz}}{\partial z} + \frac{2\sigma_{rz}}{r} + B_z = 0 \tag{58}$$

3.2. FINITE ELEMENT METHOD

Many physical processes can be described by partial differential equations [PDE]. PDEs are used to describe many physical phenomena in which a dependent variable is a function of more than one independent variables.

For many engineering applications exact solutions are difficult to calculate due to geometric and material complexities. For this reason numerical methods are used to determine approximate solutions to complex problems. The finite element method [FEM] is one numerical method used to obtain approximate solutions to complex problems. These problems may include complicated geometries, loadings, boundary conditions, or material interactions for processes where an analytical solution does not exist. The FEM utilizes the discretization of the model domain into finite elements (to obtain a discrete system) for which approximate solutions can be determined. This system will have a finite number of solutions in its domain which can be solved numerically through the use of computer algorithms. The FEM is a standard approach across all disciplines of engineering.

3.2.1. The ABAQUS™ Solver. The FEM offers a numerical approximation method for solving the governing PDEs in problems with complicated geometries, loadings and material properties. For rock mechanics the continuum of an object can be divided into an equivalent system with small finite units (elements) which are interconnected at points (nodes) by boundary lines. If linear elasticity is assumed, the characteristic relationship between the force *q* and the displacements *u* will always be of the form (Zienkiewicz, et al., 2005):

$$q^e = K^e u^e + f^e \tag{59}$$

where K^e is the element stiffness matrix, f^e is the element loading, and q^e is the internal force at the element nodes.

By inducing shape functions N_a prescribed in terms of independent variables, the displacements at any point within the element can be approximated as a column vector (Zienkiewicz, et al., 2005):

$$\vec{u} \approx \hat{u} = \sum_a \vec{N}_a \tilde{u}_a^e \tag{60}$$

The shape functions are expressed as polynomial functions of the independent variables in such a way that they can be derived to satisfy a given set of conditions at the nodes of the model. When all of the equations are combined for each element in the discrete system, a global matrix form of the equations which describes the physical conditions of the system can be obtained when the approximating equations are in integral form. The theoretical concept and method for the FEM can be found in extensive detail in many standard text books (e.g. Zienkiewicz, et al., 2005; Bathe, 2008; Dhatt and Touzot, 2012).

One drawback of this method is the introduction of errors caused by the use of approximations. Depending on the complexity of the model, the errors introduced through the FEM may be substantial. One method to lessen the amount of error introduced is to refine the mesh around complex areas in the model. Extensive studies have been conducted on the optimal mesh sizes for both wellbore and reservoir scale models (Lee et al., 2011). It has been shown that by calibrating these models with existing stress data from specific case measurements that the stress fields calculated are accurate and feasible for use in rock mechanics analyses (Goodman and Connolly 2007).

The FE modeling in this research is performed using the finite element code ABAQUS^{TM}/Standard. This software is capable of solving geotechnical problems involving 2D and 3D models (e.g., Smart, et al., 2004, 2010a, 2010b). ABAQUS^{TM} is efficient in simulating the complicated physical response of rocks due to their nonlinear material behavior and the complex geometries of petroleum reservoirs. The built-in material library consists of several constitutive material models that are capable to simulate different rock behaviors including linear elastic models and plastic models. ABAQUS^{TM} also has functions to couple stress and temperature boundary conditions.

3.2.2. Pre-stressing. In a natural setting rock formations are under an initial state of stress (in-situ) (Twiss and Moores 2007). For most of the simulations presented here it is necessary to not only consider boundary conditions, but to consider this initial state of stress in order to meet equilibrium conditions. The most appropriate way to do this is to first apply an initial state of stress to a model and then apply the appropriate boundary conditions on the pre-stressed FEM. This methodology creates a model with the appropriate stress magnitudes and boundary conditions (Thies 2008; Smart et al., 2009).

3.3. MODELLING APPROACH

3.3.1. Wellbore Optimization Methodology. The methodology presented here for determining the optimal drilling direction relies on the use of stereonet projections and pressure windows. Both the stereonet projections and mud pressure window data is obtained from 3D FEMs. The FEMs are able to accurately calculate the stresses for locations not only in the reservoir, but also in the overburden section. These stress values are extracted from the FEM and MATLAB^{TM} is used to post-process the stress data into stereonet projections and pressure windows.

3D numerical MEMs represent an excellent tool to simulate the state of stress in complex geologic environments (Goodman and Connolly 2007; Paradeis et al., 2012; Thies 2008; Eckert and Connolly 2004). When calibrated against existing stress measurements numerical MEMs are capable of predicting realistic stress magnitudes and provide a continuous 3D data field of the state of stress. This stress field can then be used to determine the optimal well path to a specific target location.

In the approach presented here, the 3D state of stress at a target location for a specific well path is extracted from the numerical MEM and stereographic projections are used at each evaluation location to determine the collapse pressure, P_c, the breakdown pressure, P_{bd}, and the pressure difference, $P_{diff}=P_{bd}-P_c$, for all possible combinations of azimuths and inclinations. The optimal angles for azimuth and inclination are determined by the largest pressure difference between breakdown and collapse pressure. In other words, the full range of inclination/azimuthal mud pressure windows is obtained at each location along the proposed well and then collapsed into a single parameter (P_{diff}) that can be optimized for. If the surface location of the drilling rig is fixed (e.g. pad or template

based drilling) the following procedure can be used to find optimal well inclinations and KOP locations. If the surface location of the rig is flexible, the procedure can be used to find both optimal drilling azimuths (i.e. surface location) and inclinations.

In order to determine the safe mud pressure window, i.e. to determine collapse and breakdown pressure, a combined Griffith-Mohr-Coulomb failure criterion is used. The procedure to calculate breakdown and collapse pressures is described in detail by Lee et al. (2011) and is exactly followed here. Calculations of inclination/azimuthal wellbore stability (IAWBS) using stereographic projections are used to calculate mud pressures (either breakdown or collapse) for all combinations of azimuths and inclinations (Peska and Zoback 1995).

It should be noted that several studies have shown that the choice of the failure criterion used has a significant influence on the prediction of the safe minimum mud pressures (Ewy 1999; Tran et al., 2010; Nawrocki 2010). The Mohr-Coulomb failure criterion is chosen for this study due to its simplicity and slightly more conservative character for predicting the collapse pressure (Zoback 2007; Yang et al., 2012). However, the methodology for wellbore trajectory planning presented in this paper can be applied using any failure criterion and thus investigation of the impact of different failure criterions is beyond the scope of this study.

The proposed methodology differs slightly based on the type of initial information. The main difference depending on whether or not the surface location for the proposed well has previously been determined, or if the surface location is fixed. For many “land” situations the surface location is pre-determined by the lease; while in many offshore situations there is more flexibility with where the actual surface location may be. Figure 3.1 outlines the workflow which is followed herein.

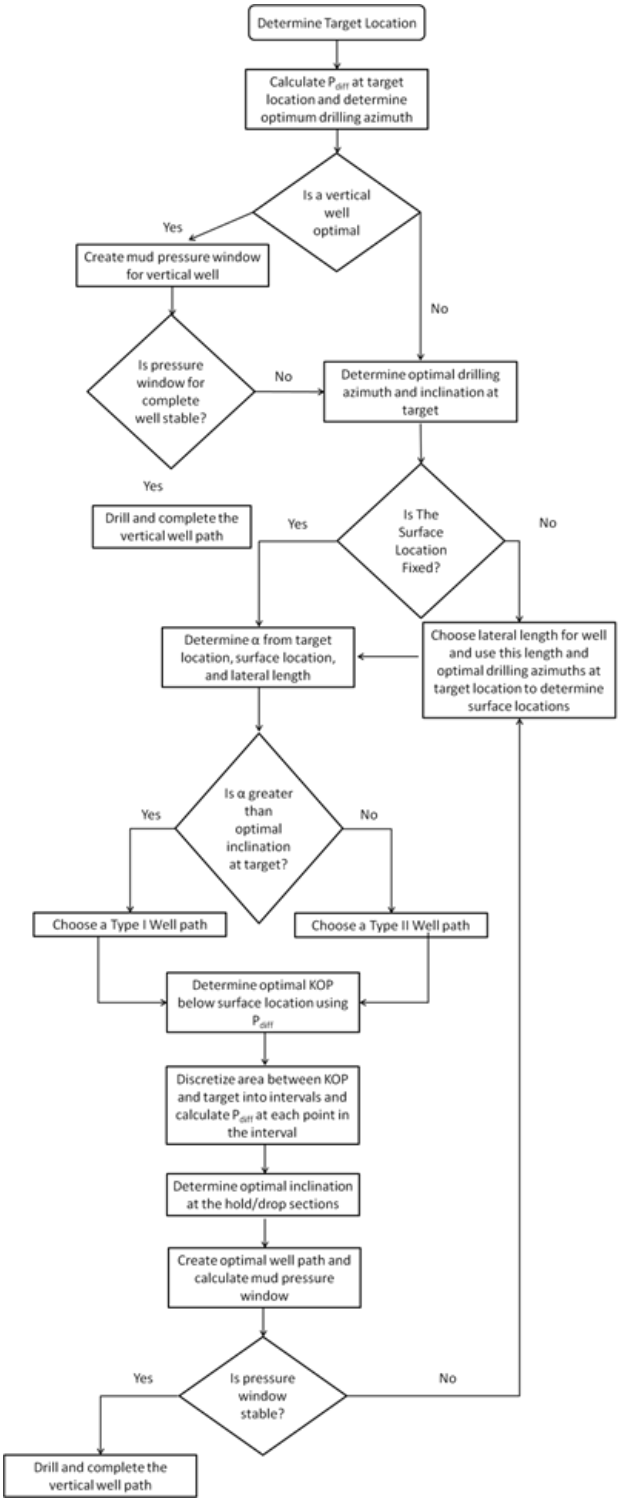

Figure 3.1. Workflow used to calculate optimal wellbore trajectories based on stress data obtained from FE models.

The angle α mentioned in Figure 3.1 is defined as the angle between ether the surface location, or the KOP, of the well and the target location (Figure 3.2).

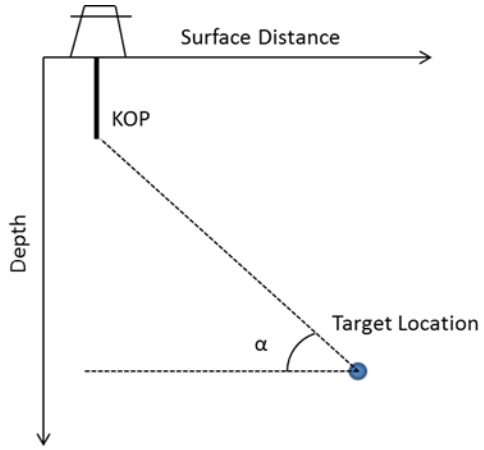

Figure 3.2. Graphical depiction of the angle α.

For any surface location starting point, the vertical section below the rig is analyzed using stereonet plots to find a suitable (i.e. safe) KOP. From the KOP the lateral distance to the target location is divided into equal intervals and at each interval stereonet plots at five depths are analyzed to determine safe conditions for the hold angle (see Figure 2.9, 3.3) and for Type IV wells to find a suitable DOP.

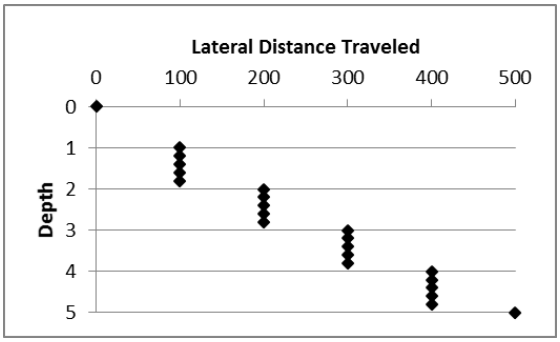

Figure 3.3. Generic representation of how the locations of stereonet projections are chosen between the KOP and target location. Each diamond represents the location of a single calculation.

With a basic layout of safe azimuth and inclination combinations at specific depths, the virtual well paths are constructed. Using a nearest neighbor approach the stress tensors extracted from the 3D FE model are mapped onto the well path (Figure 3.4) and a continuous mud pressure window for the entire well is calculated.

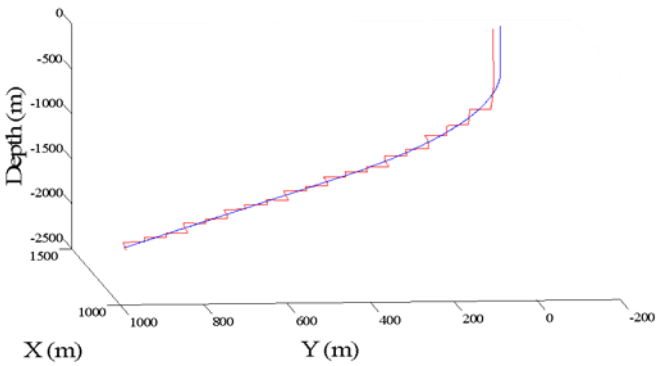

Figure 3.4. Graphical representation of the stress tensors mapped on the well. The smooth blue line is the calculated well path, while the jagged red line is made from the locations of the nodes extracted from a MEM.

3.3.2. Anticline Model Optimization Approach. An arbitrary anticline model geometry created by Paradeis et al. (2011) is used to test the importance of wellbore trajectory on the stability of a wellbore. The anticline model is described in more detail in Appendix A. Each stress regime studied simulates a unique state of stress and thus will produce differing pressure windows for the same trajectory paths. For each stress regime three vertical wellbores; one which passes through the crest, one which passes through the limb, and one which passes through the trough of the anticline structure are studied (Figure 3.5). The mud pressure windows are calculated by extracting stress data from the virtual well paths in the model and using the material properties in conjunction with the Griffith-Coulomb failure to predict wellbore failure.

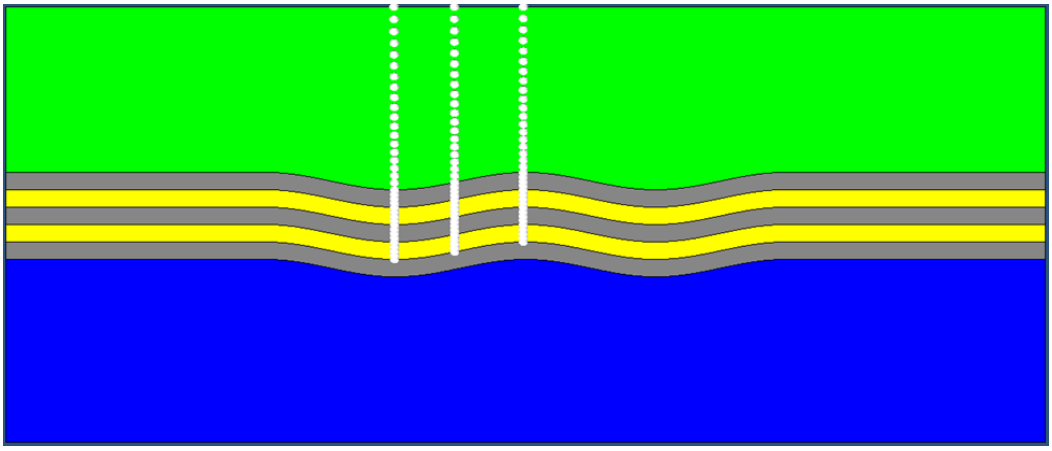

Figure 3.5. Vertical Well Locations in the anticline model (cross sectional view).

Along with the vertical wellbores above, the previously described 3D FEM has been used to plan the placement of a group of Type II deviated wellbores. The wells are placed in a circular pattern with an angle of 30^{o} separating each of the wells. Figure 3.6 shows the layout of the virtual well paths. The purpose is to determine which path would provide the most stable conditions (i.e. best mud weight window for all sections) based on the stress information from the FE model. If the best drilling location can be identified using FE models as a pre-drilling risk assessment tool, significant amounts of money and time can be saved.

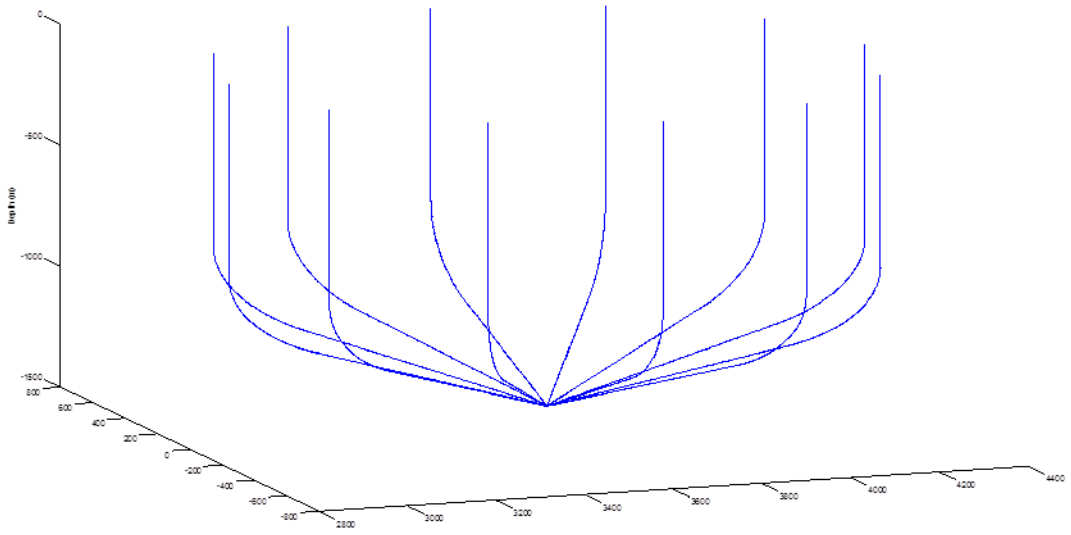

Figure 3.6. Circular group of virtual wellpaths created for data extraction from model geometry.

For the stress extraction routine along the well path a MATLAB^{TM} script is written to perform all calculations required to process the data from the FE model. The first calculations in the file constructs the path of one well. This well path is then translated in order to form the other wells in the group. For this study the well created has a true vertical depth of 1415m, a kick off point depth of 800m, the inclination angle is defined by a build-up rate of 15^{o}/100m, and a horizontal distance traveled of 718m. All of the other wells have the same initial data as this well, but are shifted 30^{o} from one another (Figure 3.6). Once all of the wells are created, the file will then use the coordinate and stress data and extract a cylinder of data which encompasses all of the wells; i.e. all stress data not containing a well path is discarded. This step is necessary to significantly reduce computation time. Figure 3.7 shows the created smoothed well paths (blue) and the matched data wells (red). It should be noted here that the angle for the well deviation is taken from the smooth trajectory (Figure 3.7, blue line) and the stress input is taken from the nearest node (Figure 3.7, red line).

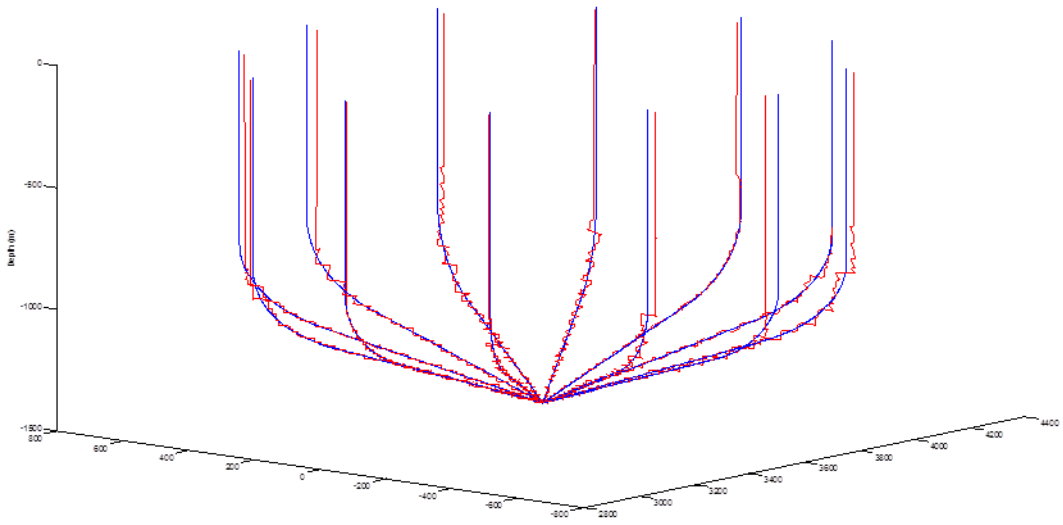

Figure 3.7. Verification plots of the extracted coordinate locations of the matched well data.

3.3.3. Approach Verification. A simplified FE model has been setup in order to validate the wellbore trajectory calculation and pressure window calculation procedures. The model which has been created for this task is a simple single material isotropic block model. The purpose of the analysis is to compare the values of the pressure window which has been calculated from the block model results to the analytical solution. The rock properties and model setup are shown in the Figure 3.8.

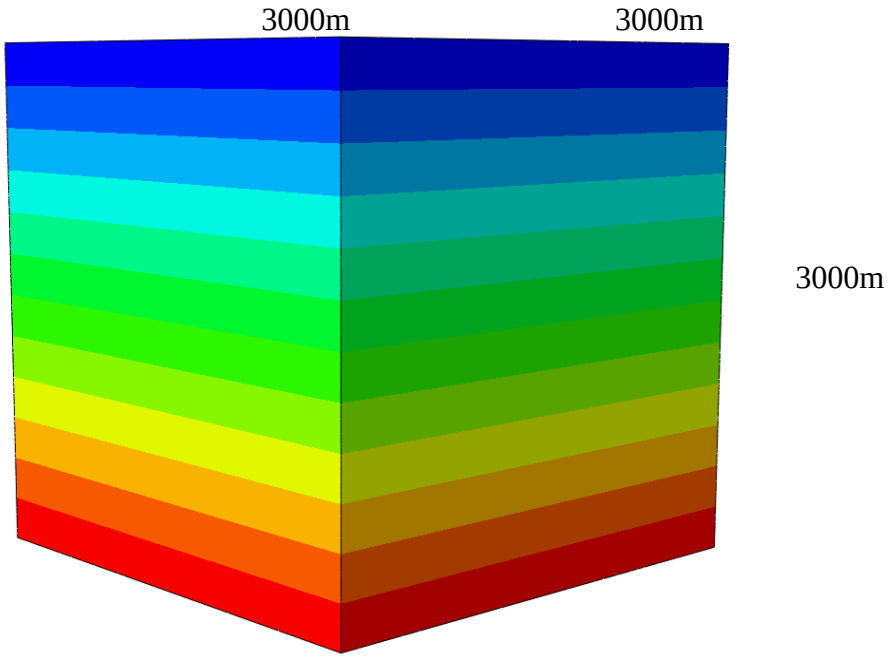

Figure 3.8. Model geometry for the simplified FE model used to calculate stresses for approach verification.

This model is comprised of only a single rock type, and was given boundary conditions which would simulate an extensional stress regime where the vertical stress is the maximum principal stress and the two horizontal stresses are equal in magnitude. The pore pressure for the model was setup to be hydrostatic. Two well paths, one vertical and one with an inclination of 45^{o} from vertical, were created in order to perform the analysis. The stress and well data which was used in the analysis are given in Table 3.1.

Table 3.1. Verification model data used as inputs to verify approach.

Model Data for Vertical Well										
Solution Type	Depth (m)	S11 (MPa)	S22 (MPa)	S33 (MPa)	S12 (MPa)	S13 (MPa)	S23 (MPa)	Pp (MPa)	α (^{o})	*i* (^{o})
Analytical	2500	40.29	40.29	61.31	0	0	0	24.53	0	0
MATLAB™	2490	40.14	40.14	61.08	~0	~0	~0	24.44	0	0
Model Data for Deviated Well										
Solution Type	Depth (m)	S11 (MPa)	S22 (MPa)	S33 (MPa)	S12 (MPa)	S13 (MPa)	S23 (MPa)	Pp (MPa)	α (^{o})	*i* (^{o})
Analytical	2500	40.29	40.29	61.31	0	0	0	24.53	30	45
MATLAB™	2490	40.14	40.14	61.08	~0	~0	~0	24.44	30	44.99

The results from the statistical analysis of the validation model are shown in Table 3.2. These results show that the analytical solution and the results from the FE model are in good agreement. In both cases the percentage of error introduced is < 1%, which shows that the results obtained through these methods are accurate and comparable to the analytical solution. A larger amount of error may be encountered in models where the element density is not high enough to obtain close matches of the experimental well path. The percentage of error is also higher in the deviated well due to the addition of the stress transformation from the geographic coordinate system to the borehole coordinate system, but still less than one percent.

Table 3.2. Verification model results.

Model Data for Vertical Well								
Results					**Statistics**			
Solution Type	$S_{\theta\theta}'$ (MPa)	S_{rr}'	Pmin (MPa)	Pmax (MPa)	% Error $S_{\theta\theta}'$	% Error S_{rr}'	% Error Pmin	% Error Pmax
Analytical	31.40	8.39	32.92	61.00	0.00	0.24	0.03	0.25
MATLAB™	31.40	8.37	32.81	60.85				
Model Data for Deviated Well								
Results					**Statistics**			
Solution Type	$S_{\theta\theta}'$ (MPa)	S_{rr}'	Pmin (MPa)	Pmax (MPa)	% Error $S_{\theta\theta}'$	% Error S_{rr}'	% Error Pmin	% Error Pmax
Analytical	21.02	14.97	39.50	50.55	0.19	0.27	0.03	0.34
MATLAB™	20.98	15.01	39.61	50.38				

4. WELLBORE OPTIMIZATION RESULTS

4.1. ANTICLINE MODEL WELLBORE TRAJECTORY STUDY

4.1.1. Extensional Regime. Fifteen pressure windows and specific gravity windows are created from the extensional regime anticline model, and are compiled in Appendix B. The pressure windows for all models are shown starting from the surface while the specific gravity windows are only shown for the near reservoir sections. The specific gravity windows are only shown for this region due to unrealistically high stresses near the surface of the models caused by the boundary conditions. For all of the pressure window plots in this thesis the blue line represents pore pressure (P_p), the green line is the collapse pressure (P_c), and the red line is the breakdown pressure (P_{bd}). For all of the specific gravity plots in this thesis the blue line represents the pore pressure gradient (P_{pg}), the green line is the collapse pressure gradient (P_{cg}) and the red line is the fracture gradient (P_{fg}).

By using the pressure windows and the knowledge of the intermediate principal stress direction the optimal drilling directions can be determined for the various models. The intermediate principal stress direction is usually the least safe drilling direction because the differential stress acting on the borehole wall is the largest for a particular stress regime. Figure 4.1 shows a visualization of the intermediate stress direction for the extensional stress regime.

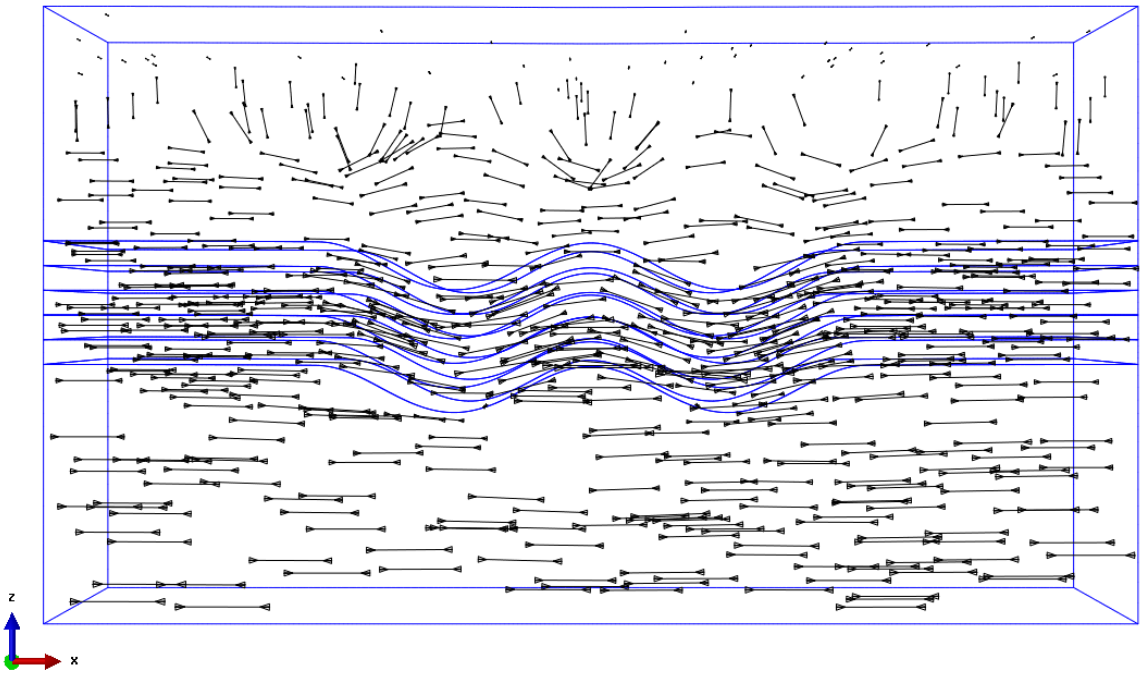

Figure 4.1. Orientation of the mid-principal stress for the extensional anticline model.

From Figure 4.1 the least safe drilling direction in this stress regime is highly influenced by the geometry and boundary conditions. At the surface of the model the least safe direction is along the y axis, but then changes to the vertical direction after about 100m. The least safe direction at the reservoir would be a completely horizontal well along the x axis. The same trends can be seen from the figures given in Appendix B. The smallest sections of the pressure windows are at the surface where the pore pressure has become the minimum safe mud weight for drilling. If the windows are examined as a whole, with the target as the main point of interest, it can be seen that as the azimuthal angle approaches either 90^o or 270^o the pressure window narrows more than it does at other angles. By inspection it can be seen that as the azimuthal angle approaches angles of either 0^o or 180^o the pressure window gets wider. Figure 4.2A shows the pressure window at an azimuth of 0^o, while Figure 4.2B shows the pressure window at an azimuth of 90^o. Figures 4.2C and 4.2D display the specific gravity windows for the reservoir layer at 0^o and 90^o respectively. The specific gravity windows show similar results as the pressure windows in that as the azimuth of the wellbore approaches 90^o, the window

narrows. This implies that wellbores which are oriented at 90^{o} would require mud weight programs with smaller safety margins.

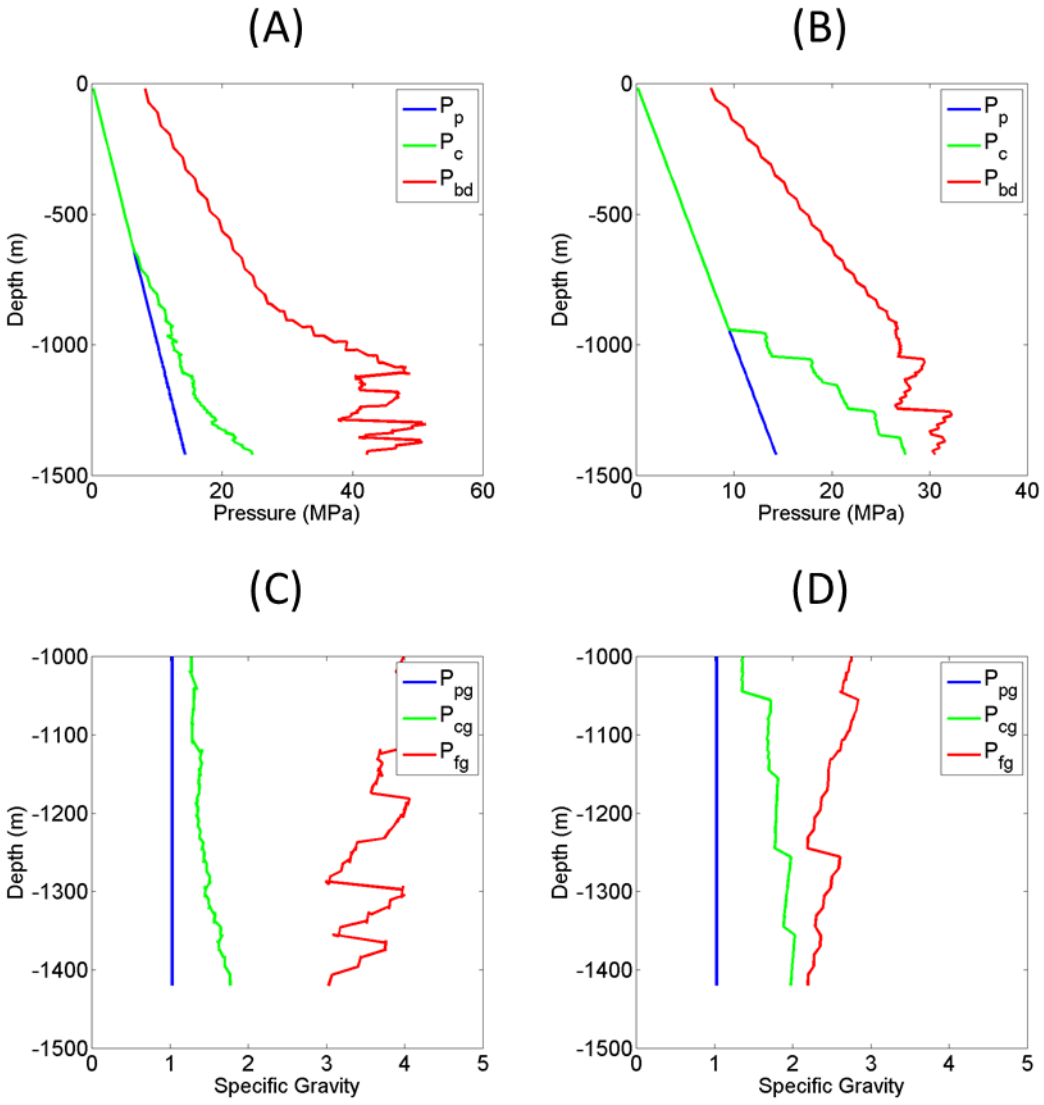

Figure 4.2. Pressure windows and specific gravity windows for Type II wells at 0^{o} (A and C) and 90^{o} (B and D).

Figure 4.2A represents the best and Figure 4.2B the least favorable drilling directions for the extensional model. It can be seen that the pressure window at 0^{o} is wider and may lessen the amount of casing points needed. It should be noted that both wells can be drilled safely, however the costs associated to casing and mud design will be

different. If drilling were to be done in this model the best direction would either be at 0^o or 180^o, but there may still be slight drilling problems near the surface where all of the wells would be vertical and would be drilling in the least safe drilling direction. Wells drilled in directions of 90^o or 270^o should be avoided in this model.

The same results can be seen by using a stereonet projection of the P_{diff} at the target location (Figure 4.3). The principal stress tensor obtained from the reservoir layer which is used to create the stereonet projection in Figure 4.3 is given by:

$$\sigma^P = \begin{bmatrix} 22.32 & 0 & 0 \\ 0 & 17.21 & 0 \\ 0 & 0 & 11.55 \end{bmatrix} (MPa) \tag{61}$$

This projection shows that wells drilled at high inclinations and azimuths of 0^o or 180^o would be marginally safer than wells which are drilled at high inclinations with azimuths of 90^o or 270^o.

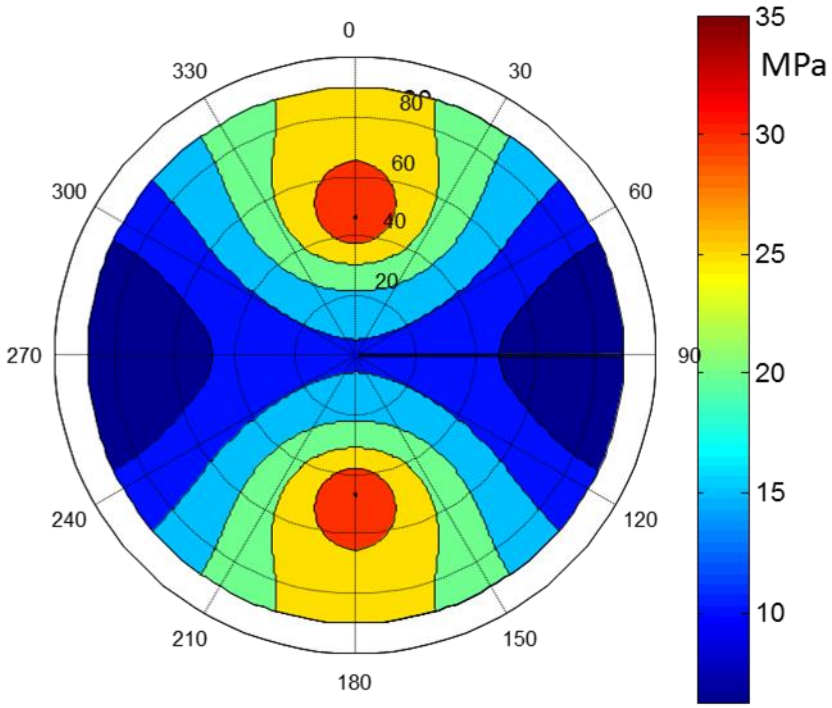

Figure 4.3. Stereonet projection of P_{diff} at the target location for all of the deviated wellbores in the extensional model.

Pressure and specific gravity windows are also constructed for the three vertical wells in the anticline model. The pressure windows for these wells are displayed in Figure 4.4.

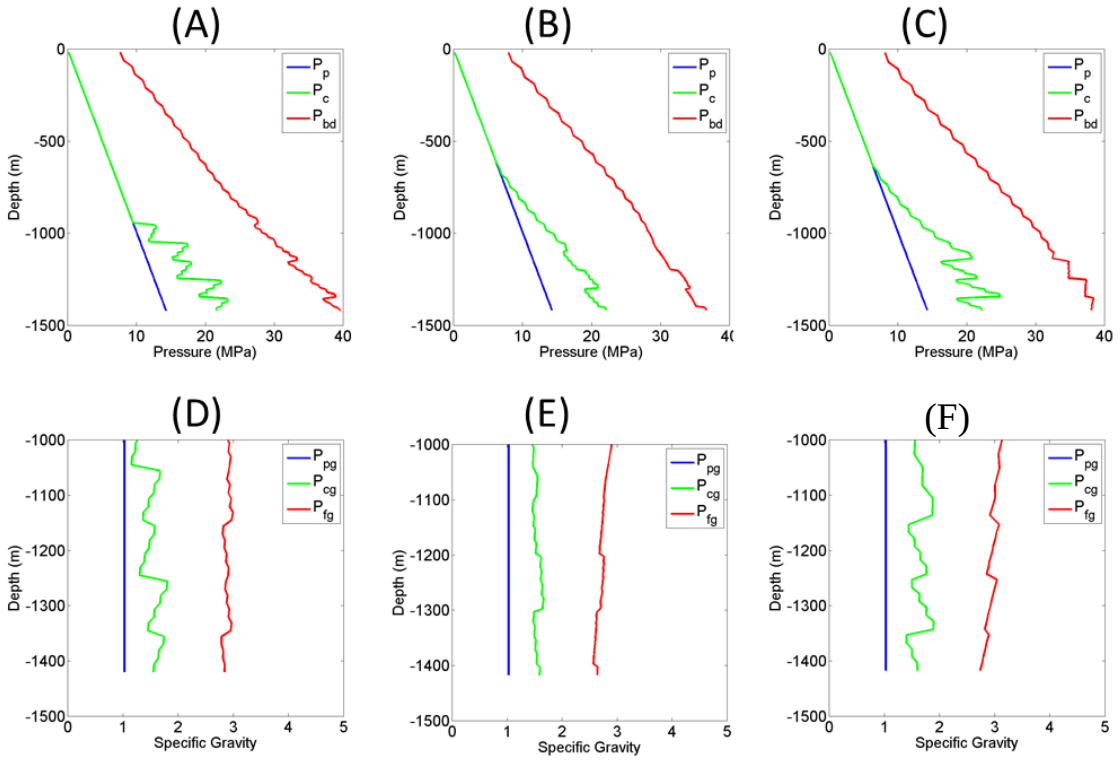

Figure 4.4. Vertical well pressure windows at the crest (A and D), limb (B and E), and valley (C and F) of the anticline in the extensional stress regime.

4.1.2. Compressional Regime. Fifteen pressure and specific gravity windows are created from the compressional regime anticline model, and are shown in detail in Appendix C. Figure 4.5 shows a visualization of the intermediate stress direction for this model.

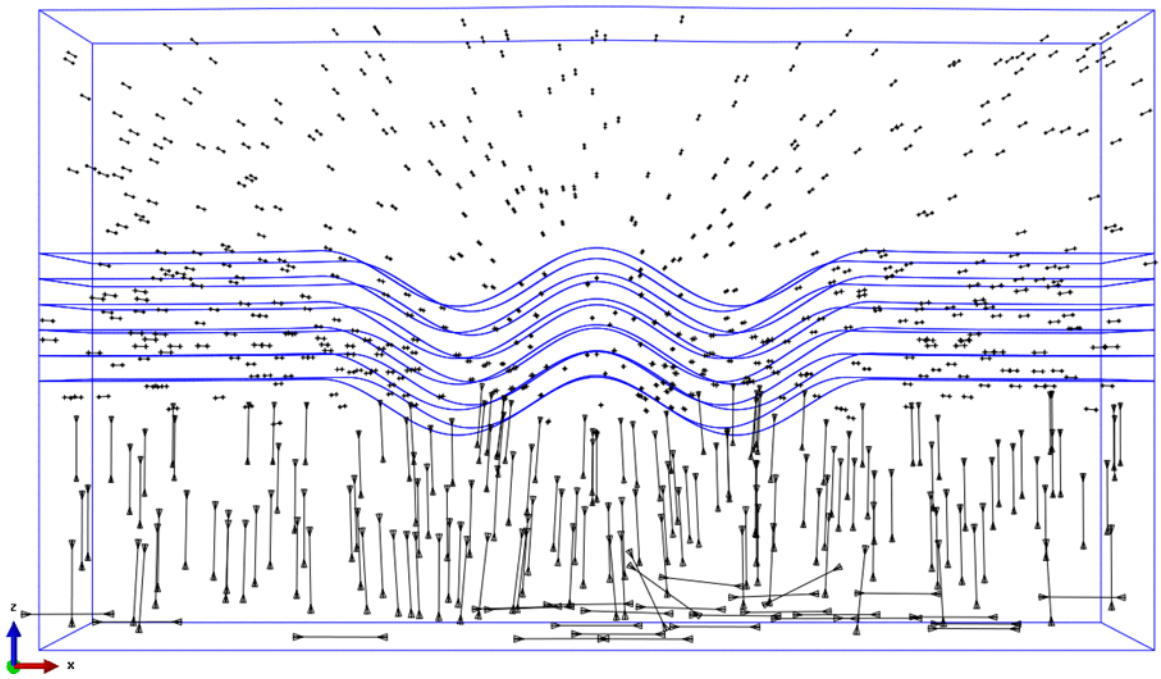

Figure 4.5. Orientation of the mid-principal stress for the compressional anticline model.

The least safe drilling direction in this stress regime is highly influenced by the geometry and boundary conditions. At the surface of the model the least safe direction is along the y axis. The least safe direction at the reservoir would be a completely horizontal well along the x axis. The same trends can be seen from the figures in Appendix C. For this stress regime the safest drilling direction would be at angles of 90^{o} and 270^{o}, while the least safe drilling direction would be wells along 0^{o} and 180^{o}. This can be seen in the pressure windows displayed in Figure 4.6 and the stereonet projection in Figure 4.7. Figure 4.6C and Figure 4.6D also show that the specific gravity window for wells drilled at 0^{o} are narrower than specific gravity windows for any other orientation.

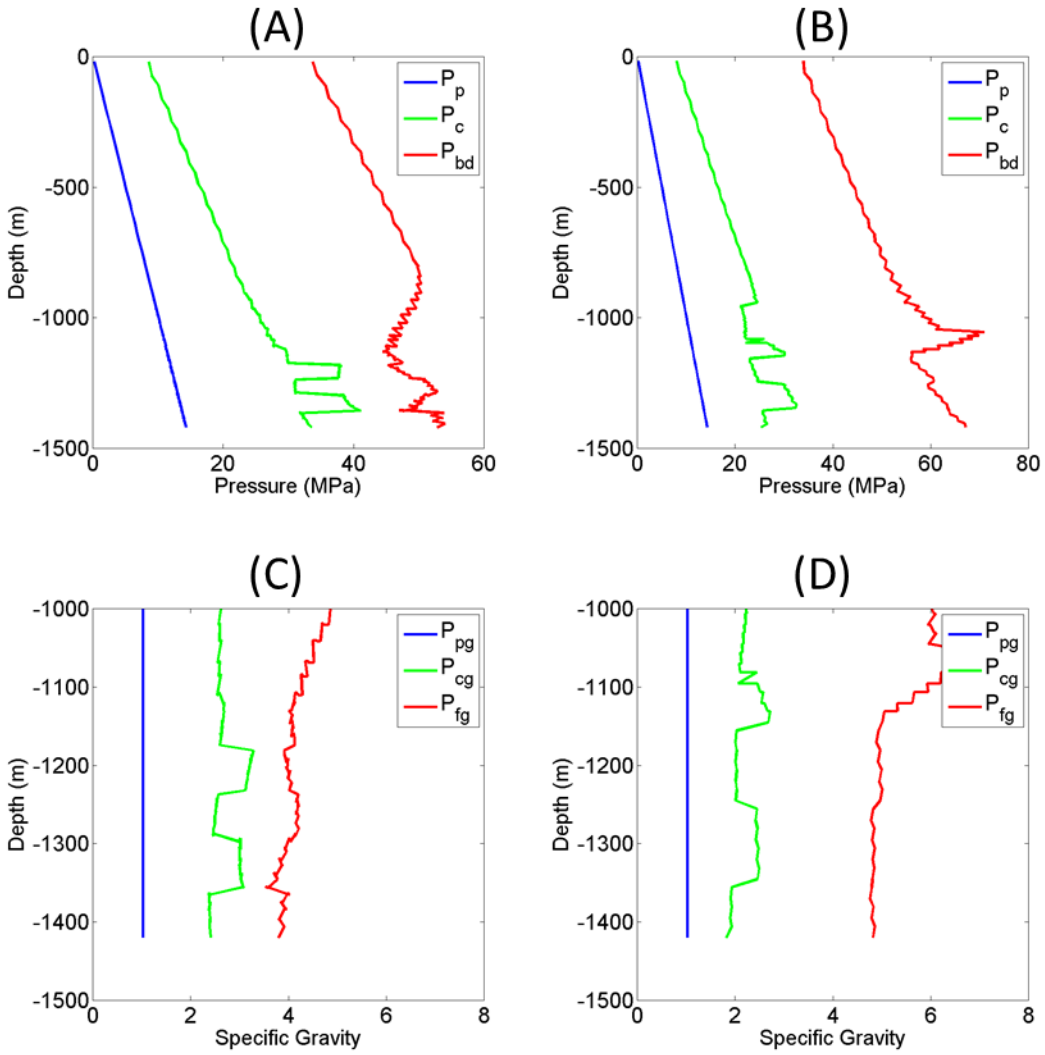

Figure 4.6. Pressure windows for Type II wells at 0^o (A and C) and 90^o (B and D) in the compressional stress regime.

The principal stress tensor obtained from the reservoir layer and which is used to create the stereonet projection in Figure 4.7 is given by:

$$\sigma^P = \begin{bmatrix} 34.25 & 0 & 0 \\ 0 & 25.42 & 0 \\ 0 & 0 & 21.78 \end{bmatrix} (MPa) \tag{62}$$

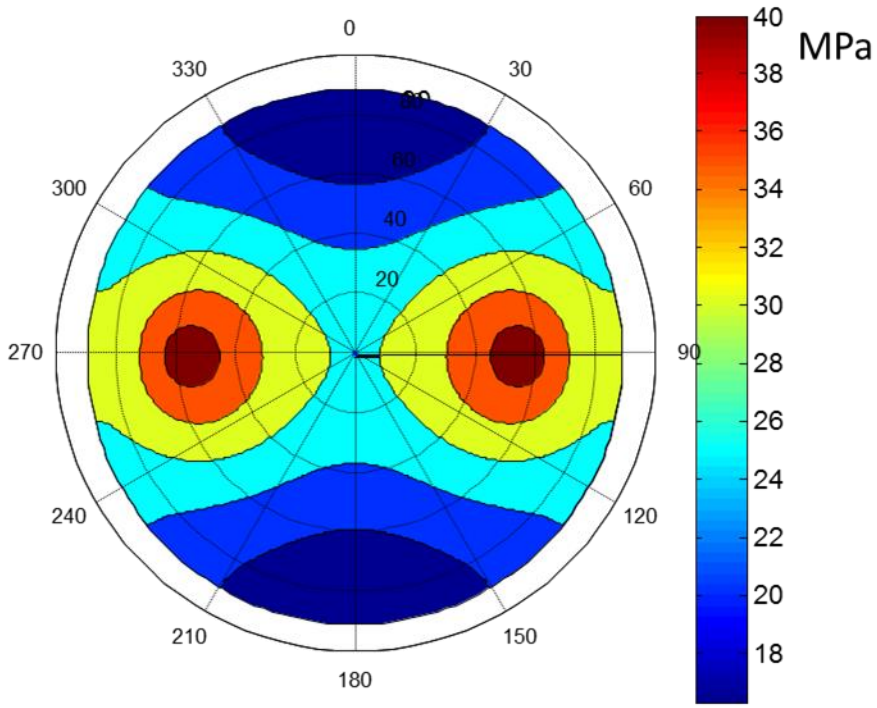

Figure 4.7. Stereonet projection of P_{diff} at the target location for all of the deviated wellbores in the compressional model.

Pressure and specific gravity windows are also constructed for the three vertical wells in the anticline model. The pressure windows for these wells are displayed in Figure 4.8. As can be seen all three vertical wells are stable.

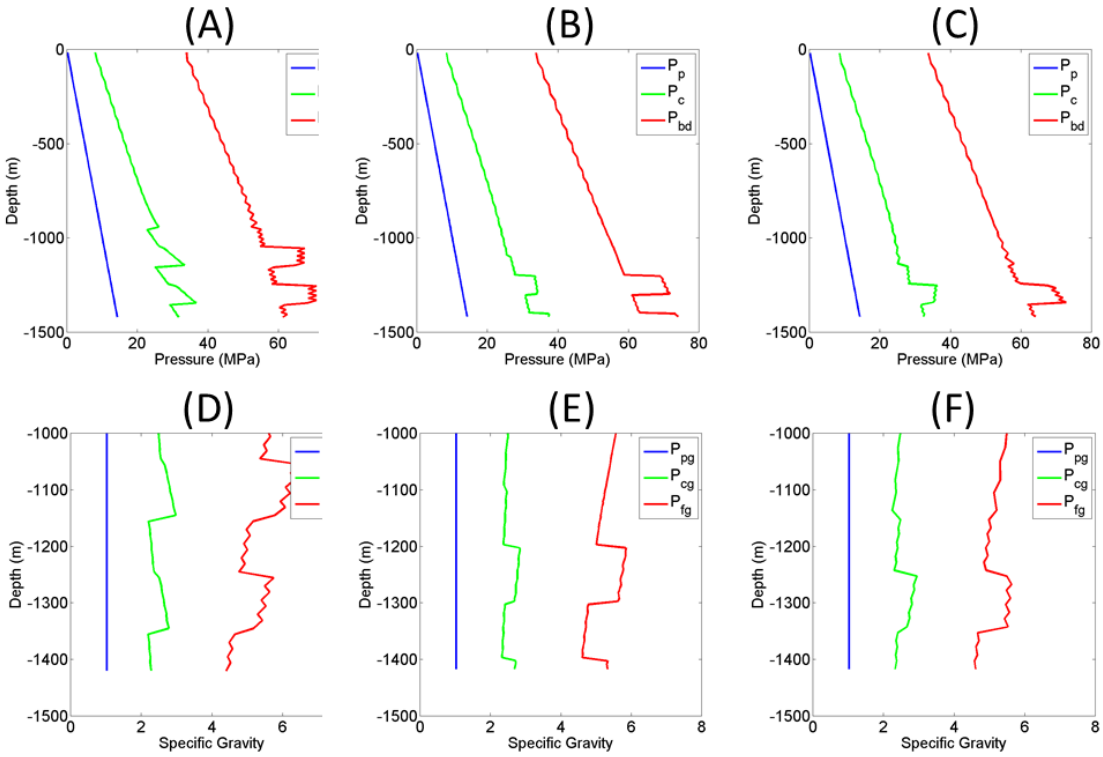

Figure 4.8. Vertical well pressure windows at the crest (A and D), limb (B and E), and valley (C and F) of the anticline in the compressional model.

4.1.1. Strike-Slip Regime. Fifteen pressure and specific gravity windows are created from the strike-slip regime anticline model and are compiled in Appendix D. By using the pressure windows and the knowledge of the intermediate principal stress direction the optimal drilling directions can be determined for this model. Figure 4.9 shows a visualization of the intermediate stress direction for this model.

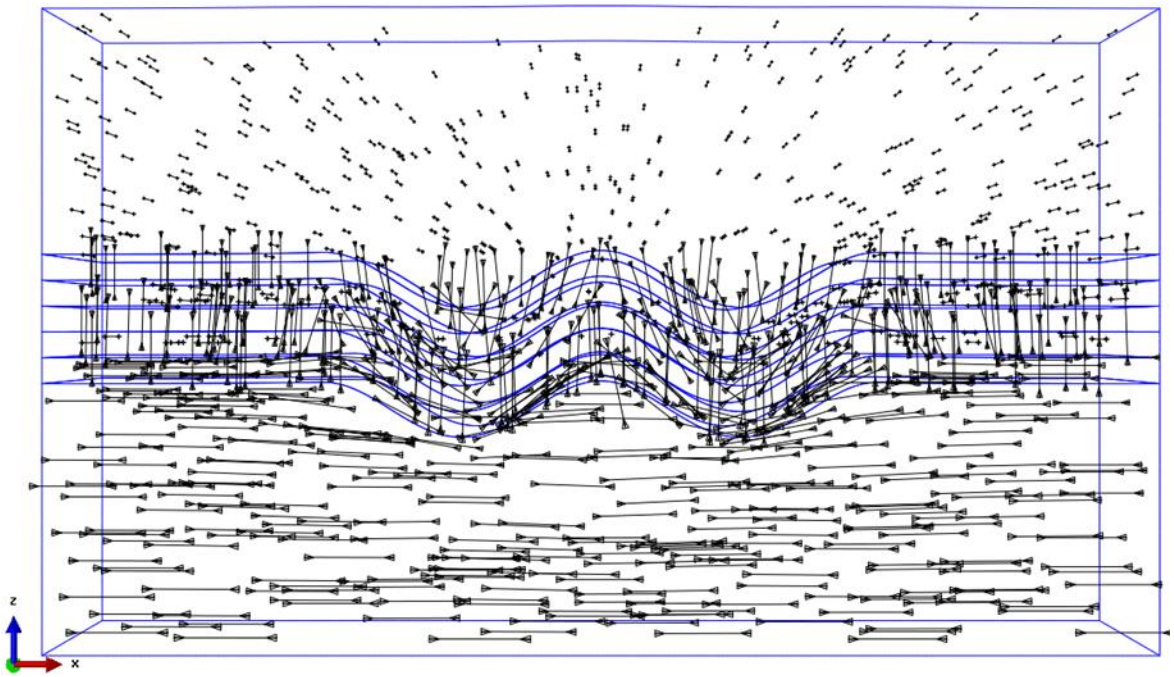

Figure 4.9. Orientation of the mid-principal stress for the strike-slip anticline model.

Figure 4.9 shows the least safe drilling direction in this stress regime is highly influenced by the geometry and boundary conditions. At the surface of the model the least safe direction is along the y axis. The least safe direction at the reservoir would be a vertical well along the z axis. The same trends can be seen from the figures in Appendix D. For this stress regime pressure and specific gravity windows at 0^o and 90^o are displayed in Figure 4.10, while a stereonet from the target location is displayed in Figure 4.11.

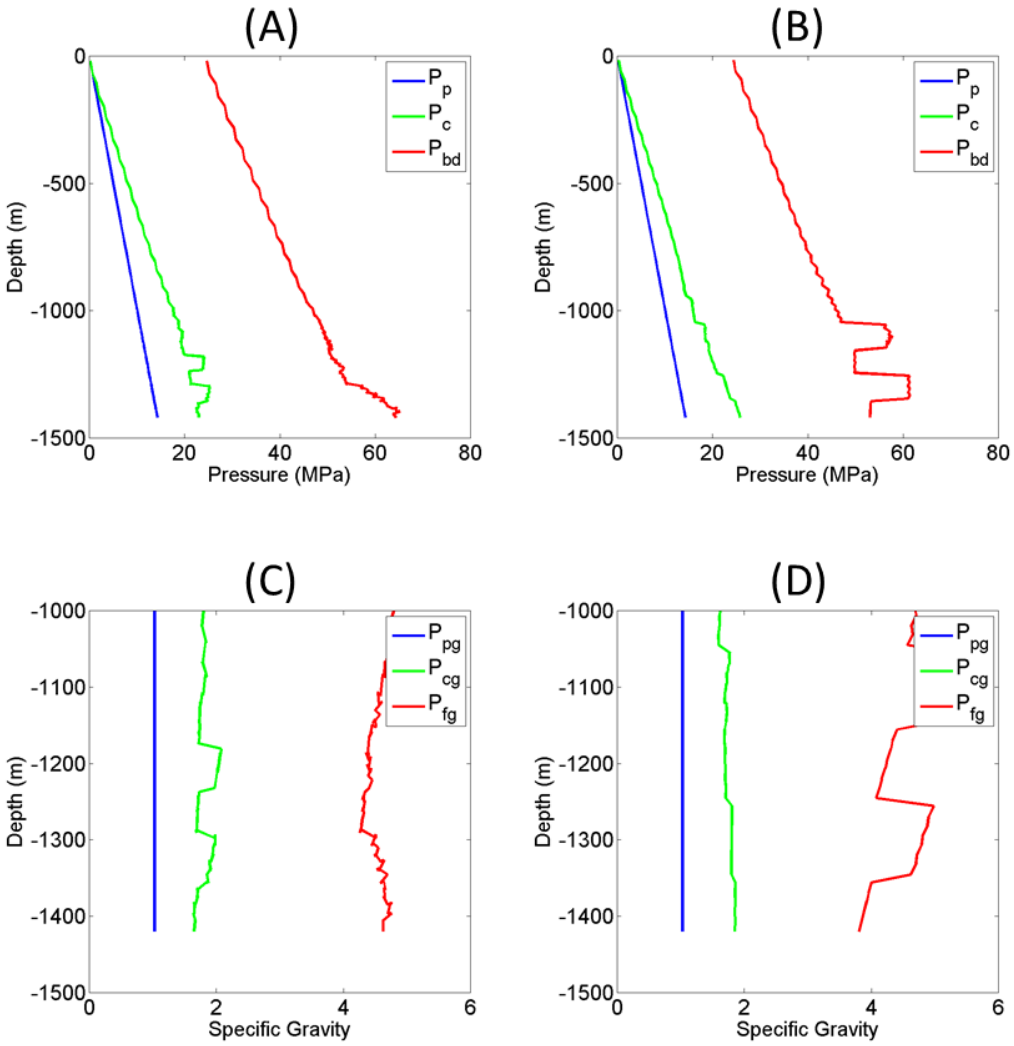

Figure 4.10. Pressure windows for Type I wells at 0^o (a) and 90^o (b) in the strike-slip stress regime.

The principal stress tensor obtained from the reservoir layer and which is used to create the stereonet projection in Figure 4.11 is given by:

$$\sigma^P = \begin{bmatrix} 24.97 & 0 & 0 \\ 0 & 22.94 & 0 \\ 0 & 0 & 19.40 \end{bmatrix} (MPa) \tag{63}$$

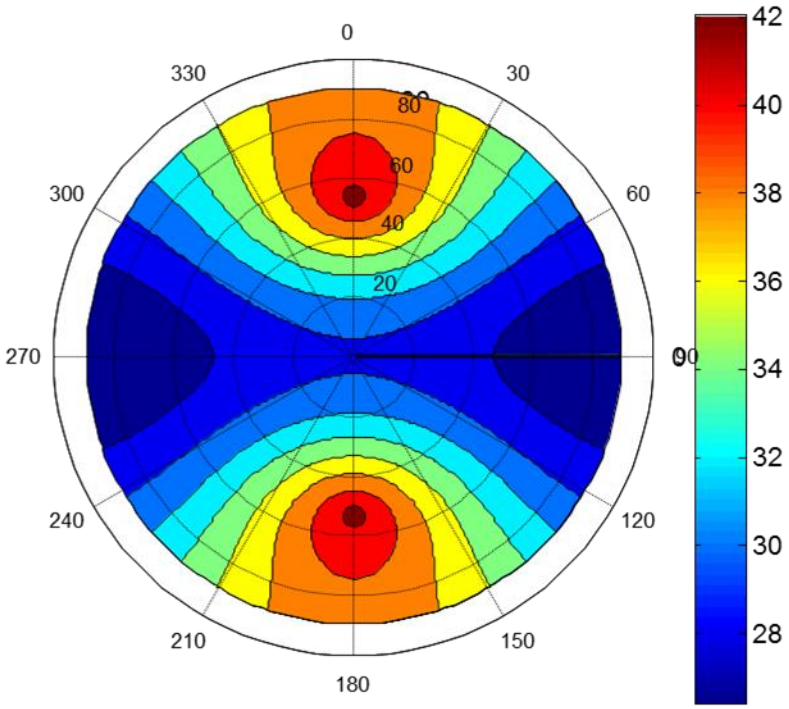

Figure 4.11. Stereonet projection of P_{diff} at the target location for all of the deviated wellbores in the strike-slip model.

Pressure windows are also constructed for the three vertical wells in the anticline model. The pressure windows for these wells are displayed in Figure 4.12. As can be seen all three vertical wells are stable.

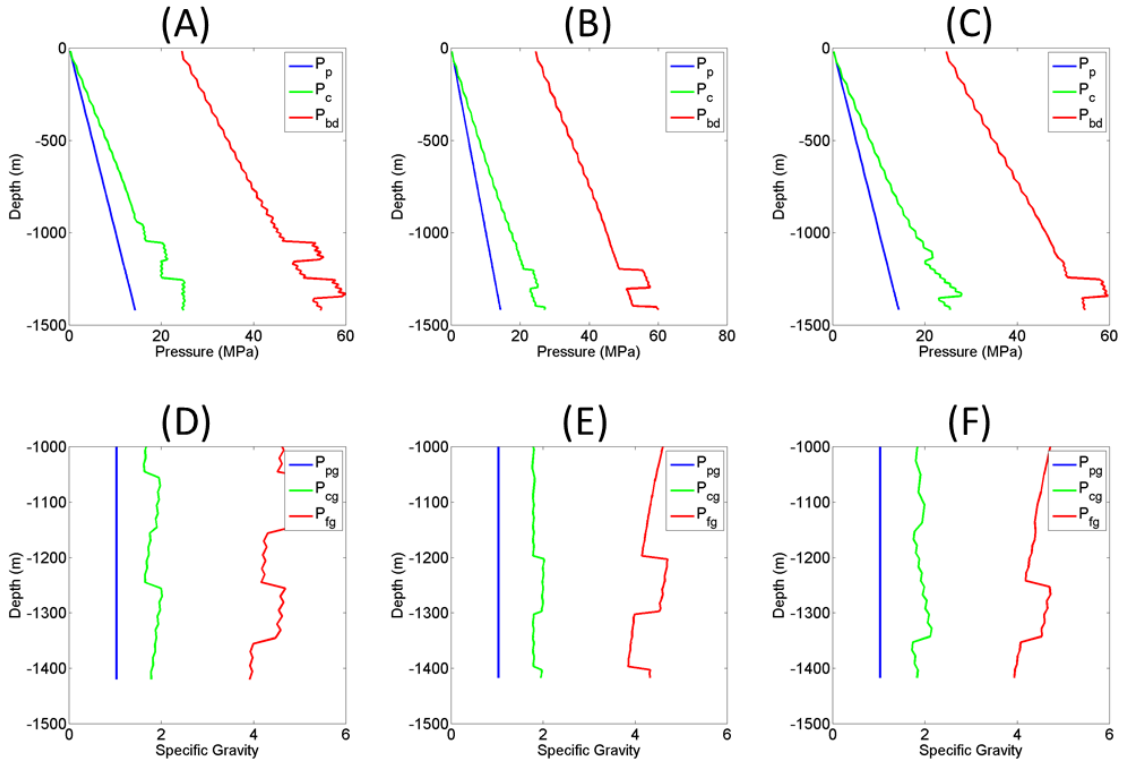

Figure 4.12. Vertical well pressure windows at the crest (a), limb (b), and valley (c) of the anticline in the strike-slip model.

4.2. OPTIMIZED DRILLING CASE STUDY

The methodology described in section 3.3.1 is also being applied to stress tensors extracted from a synthetic MEM representative of a "3 way against salt" field in the deep water Gulf of Mexico (Peter Connolly, personal communication). The geologic scenario results in a state of stress which is non-Andersonian and varies considerably both laterally and vertically.

For this study a common target location in the center of the model is chosen for all wells tested. The surface location is assumed to be flexible; therefore, all possible azimuth angles are tested. A lateral reach of 1,000m is chosen based on the size of the numerical model. The rock properties required to calculate failure are assumed to be constant throughout the volume. Cohesion, So, tensile strength, T_o, friction angle, ø, and Poisson's ratio, ν are given values of 10MPa, 5MPa, 30°, and 0.3 respectively. Clearly,

this is not the case in a real world situation, where these parameters change along the well trajectory, just as the stresses are in these illustrative examples.

Assessment of an arbitrary well path, in this case vertical, is the first step for finding an optimized wellbore trajectory Stereonet projections at selected depths and a continuous mud pressure window are presented in Figure 4.13. Both stereonet projections and the mud pressure window show the highly varying conditions of the vertical well path. Although the overall conditions suggest a stable well, the vertical trajectory is considered unpractical. To maintain wellbore stability a total of 4 casing sections have to be used. Furthermore, the pressure window between 1600m and 2100m narrows to less than 5MPa. In order to circumvent these complications, a deviated well path is designed for this area.

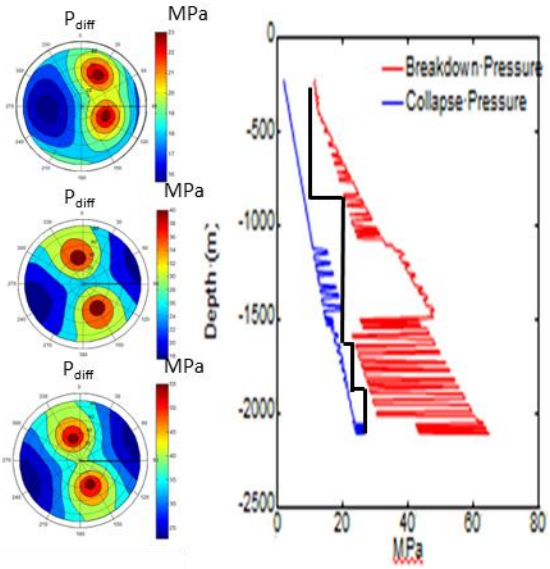

Figure 4.13. Three stereonets along a vertical path above the target location are shown above. The first was taken at a depth of 600m, the second at 1500m, and the third at 2100m.The plot on the right is a mud pressure window from a vertical well located at the target location where the solid black lines indicate casing sections.

In order to determine an optimized, stable deviated wellpath, a stereonet projection of P_{diff} at the target location is used to define the optimum drilling azimuth and inclination angle (Figure 4.14).

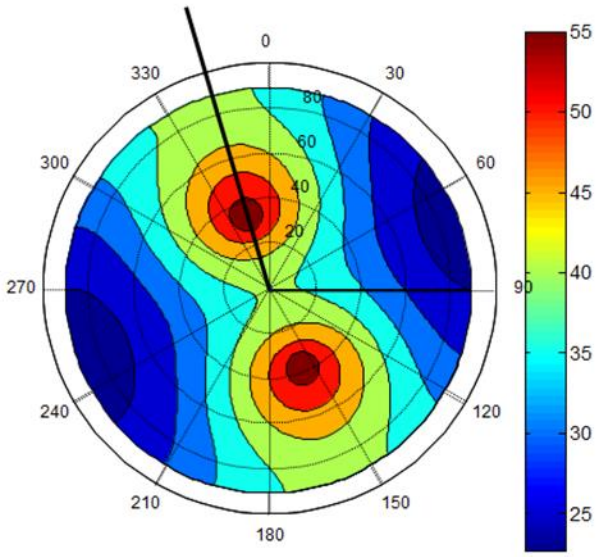

Figure 4.14. Stereonet projection of the P_{diff} at the target location. The solid black line denotes the azimuth of optimal drilling. The solid red line shows the azimuth of the un-optimized well path.

The optimal drilling direction at the target location is shown as the solid black line in Figure 4.14. This line lies at an azimuth of 345^{o}, with the optimal inclination being approximately 35^{o}-45^{o}. With the optimal drilling direction at the target location being determined, and with the lateral length of the chosen well, the surface location of the well can be found. Using this surface location as a starting point, 20 stereonet projections of P_{diff} at varying depths below the surface location are used to determine the optimal KOP (Figure 4.15). The depth of stereonet B is chosen as the most suitable depth for the KOP. At this depth the optimal azimuth and inclination angles determined for the target location (345° and 45°) also result in the largest P_{diff} compared to the other depths. As

can be seen in stereonets C and D (Figure 4.15) P_{diff} decreases in the direction of optimal drilling azimuth.

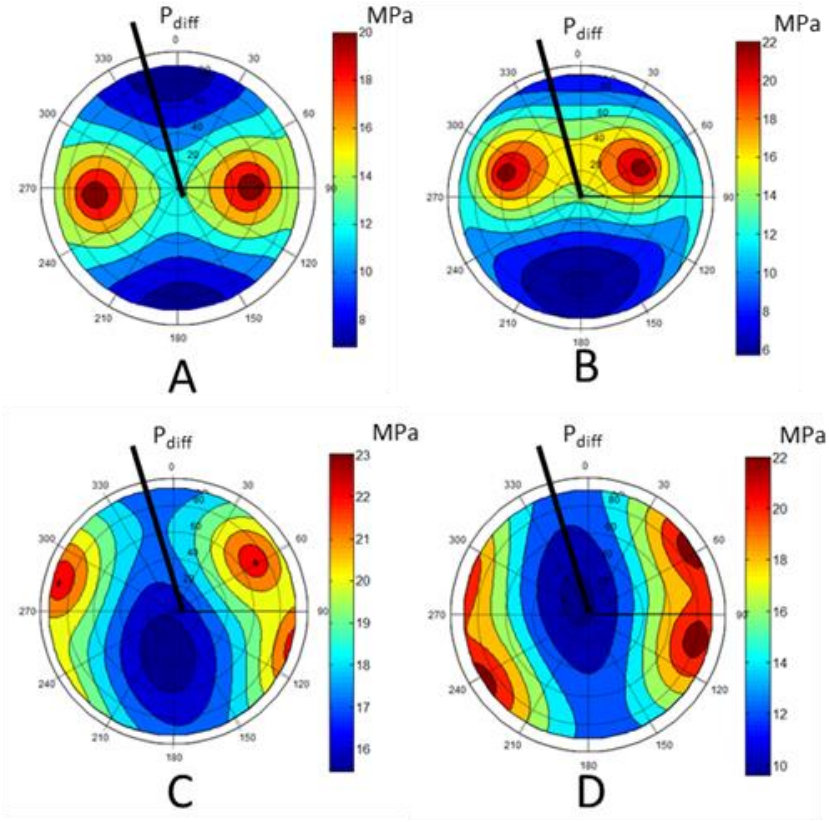

Figure 4.15. Stereonet projections of P_{diff} along a vertical line below the surface location. Stereonet A is at a depth of 450m, stereonet B at 500m, stereonet C at 550m, and stereonet D is at a depth of 600m.

Following the geometry in Figure 3.2 the angle α is determined as 57°. Thus, a Type II well profile is chosen to be the preferred well shape. In order to ensure stable conditions for the "hold" section (for the chosen azimuth and inclination) of the well path, the distance between the target location and the KOP is discretized into ten 100m intervals (following the methodology of Figure 3.3). At each interval 5 depths are analyzed using stereonet projections. Figure 4.16 shows four stereonet projections which are intersected by the well path at lateral intervals of 200m (Figure 4.17).

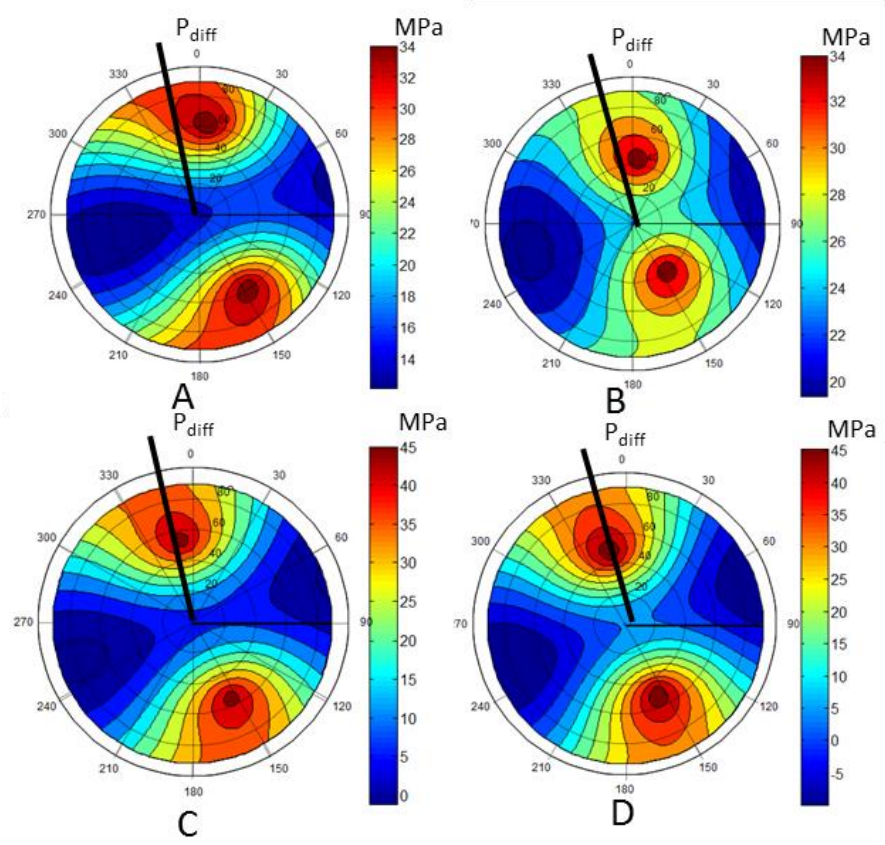

Figure 4.16. Stereonet projections of Pdiff along the hold section of the optimized well path. The depth is decreasing from A-D.

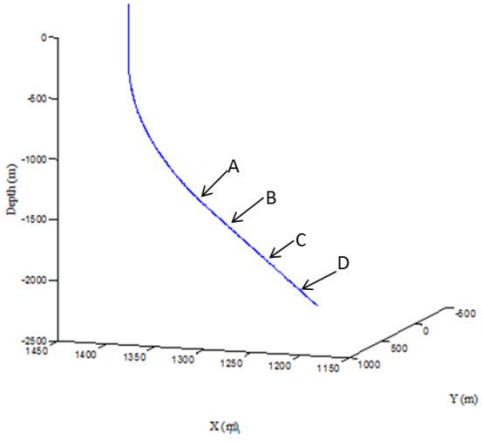

Figure 4.17. Approximate locations for the given stereonet projections on the proposed well path.

The stereonets displayed in Figure 4.16 show that the chosen azimuth and inclination do not represent the most optimized combination at the beginning of the hold section. However, as the well extends deeper into the subsurface the stress orientations are changing such that the optimal azimuth and inclination converge to the previously determined optimized combination at the target location.

With all of the necessary components to build a Type II well path tested, the well trajectory can be constructed and placed in the numerical MEM. By extracting the stress data from the MEM along the well path the continuous mud pressure window can be created (Figure 4.18). Compared to the vertical well (Figure 4.13) the mud pressure window is much wider (i.e. the wellbore is more stable) and fewer casing points have to be set.

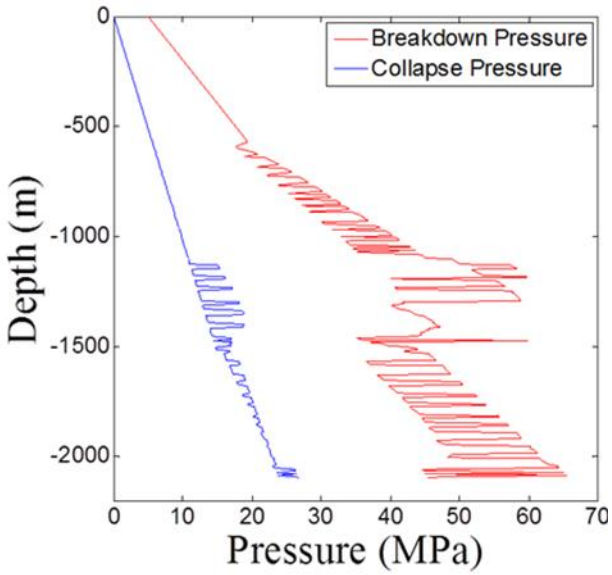

Figure 4.18. Mud pressure window for the optimized well trajectory.

For the purpose of comparison, an un-optimized, worst-case scenario well path is also presented. This well is created using the same Type II trajectory and inclination angle as the optimized well path, but was placed along an azimuth of 60^{o}. As seen in Figure 4.14, a well placed along this azimuth is not preferentially oriented and has a

much narrower mud pressure window when compared to the optimized well path (Figure 4.19). Furthermore, at specific depths, the breakdown pressure and the collapse pressure lines cross indicating unstable drilling conditions which cannot be resolved by mud weight adjustments.

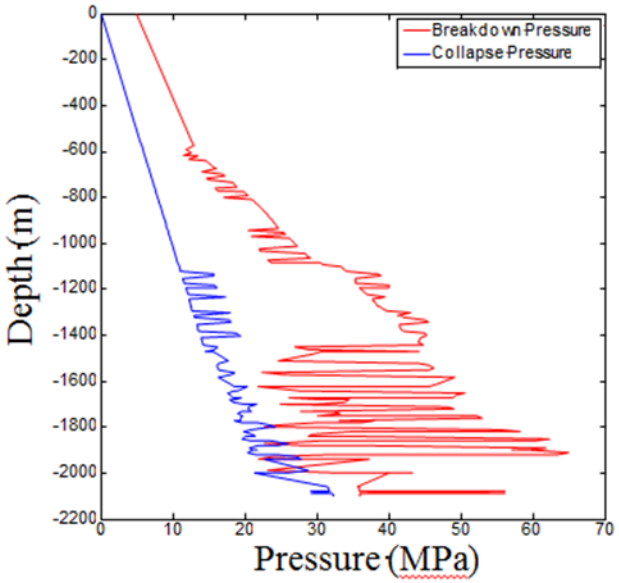

Figure 4.19. Mud pressure window from an un-optimized well path with an azimuth of 60^{o} and an inclination of 45^{o}.

5. WELLBORE OPTIMIZATION DISCUSSION AND CONCLUSIONS

5.1. ANTICLINE MODEL

The results for the wellbore stability analysis have shown that while vertical wells have proven to be stable for all three stress regimes, deviated wellbores through the same model may not be as safe. However, in many situations a deviated wellbore may be necessary in order to reach the target location or for maximizing the reservoir volume contacted. For these situations the procedure which has been developed can be readily applied to prospective case studies with more complex material models and geometries. It has been shown that knowledge of stress directions can be applied to the results of FEMs to determine the orientation of safe wellbores.

The results of the anticline model show that the presence of geometry can significantly influence the wellbore safety and optimal drilling directions. If information of the reservoir shape, commonly obtained through seismic, is known the accuracy of FEMs for determining the safe operating windows can be improved.

For the extensional stress regime the mud pressure windows show a clear dependence on the wellbore orientation; an optimal orientation can be determined for the given wellbore profile. In this model the mud pressure windows concur with the theory that the least safe drilling direction is in the direction of the intermediate principal stress; direction of the maximum horizontal stress for the case of an extensional stress regime (Figure 4.1). The safest wells would have azimuths of 90^o and 270^o, which are perpendicular to the intermediate principal stress direction. Because the full wellbore profile (i.e. the inclination) was already pre-determined for the anticline model, only the azimuth is able to be optimized. If the wellbore profile was not pre-determined then more extensive use of the stereonet projections could have been used to fully optimize the wellbore trajectories for the anticline model. As shown in the figures in Appendix B, as the azimuthal angle deviates further from either of 90^o or 270^o the operational windows closes to its least safe positions at 0^o and 180^o. For these orientations (0^o and 180^o) the safe operational window narrows to <5MPa and would require multiple casing points to be set.

The results of the compressional model are similar to that of the previously discussed extensional model. The mud pressure windows are highly influenced by the orientation of the wellbore. From the pressure windows we can see that for vertical sections of the wellbore the proposed well paths are less safe than they were in the extensional model. For the extensional model vertical wellbore sections, the pore pressure represents the minimum allowable mud pressure, while in the compressional model the collapse pressure, P_c, curve is greater than the pore pressure at all locations. This is most likely due to the relatively minimal differences in magnitude between the principal stresses in the shallow regions in both the compressional and strike-slip models.

For the compressional model the safest drilling direction is also at 90^o and 270^o, while the least safe drilling directions would be at 0^o and 180^o. The most notable difference for these drilling directions in this model can be seen in Figure 4.6, where a well oriented at 90^o could theoretically be drilled using a single pressure, while wells which are non-preferentially oriented would need at least two pressure magnitudes. This would result in more time spent tripping in and out of the hole and an increase in mud additive costs.

The strike-slip model features mud pressure windows which have less variability when compared to the extensional and compressional models. This is mostly due to the boundary conditions which were used to create the strike-slip stress regime at the reservoir layer. This boundary condition setup yields a differential stress throughout the overburden layers that is constant throughout the model. This constant differential stress then equates to giving a relatively constant operational window for each of the wellbore trajectories.

For the original purpose of these models in the context of wellbore stability and integrity assessment for CO_2 sequestration applications, the use of extra casing sections may be preferred for each of the models near the target location. This would be especially true for any scenario which may cause additional fractures into the formation. For CO_2 sequestration the zone which is being used for storage must be isolated in order not to breach any other formations. If drilling induced tensile fractures were to form they may open pathways for fluid flow into an area which is not desired, and/or could cause seal breach of the CO_2 into other formations. Not only is this a problem for sequestration of

the CO_2, but depending on where the leak is occurring, it could also pose an environmental risk.

5.2. CASE STUDY WELLBORE TRAJECTORY OPTIMIZATION

Wellbore stability represents a crucial field in the development of hydrocarbon exploration and production. Instable wells, amongst others, cause reduced drilling performance, lost circulation, stuck bottom hole assembly, well work-over costs, and at worst can lead to a total collapse and a loss of the wellbore. A thorough geomechanical analysis in the planning stage of a well can significantly reduce these risks. A large number of 'conventional' wellbore trajectory planning studies utilize 1D MEMs to predict the reservoir state of stress and rock strength parameters from wireline logging measurements and hydraulic minifrac tests. Based on these data sets a mud pressure window for the logged well can be obtained. If unstable conditions occur, stereographic projections are utilized to find more optimal drilling azimuths and inclinations for different wells in the same field (Zoback 2007; Rahim et al., 2012; Last et al., 1996). While this approach proves successful and valid for a large number of case studies it utilizes the inherent assumption of an ASoS and thus is not valid for cases where complex geologic structures violate this assumption.

For such scenarios 3D numerical MEMs have proven to be an excellent tool for continuous spatial stress prediction. 3D MEMs of hydrocarbon fields are calibrated against stress measurements and predict realistic stress magnitudes (Goodman and Connolly 2007). Based on 3D numerical MEMs the methodology presented in this paper represents a valuable work process to optimize wellbore trajectories in the planning stage of a well. Assumptions on the state of stress are not necessary as the 3D MEM provides the complete stress tensor at any location in the model. The methodology is based on most general mathematical description and thus enables all possible scenarios of azimuth, inclination and surface rig location for multiple well types along the entire trajectory of the well path. The methodology can also be applied for any failure criterion.

The case study results show that if applied to a scenario with a highly varying state of stress a significant improvement of wellbore stability conditions can be achieved. In comparison to a vertical well the proposed well trajectory has a significantly wider

mud pressure window also resulting in a reduction of casing points. In an industry where days can equate to millions of dollars, any pre-drilling steps which can be taken to either reduce drilling time or the occurrence of drilling failure is valuable. The methodology presented in this study gives drilling engineers yet another tool which can be used to alleviate some common problems.

Although neither stereographic projections nor mud pressure windows alone can produce optimal wellbore trajectory results, the combination of the two can be a powerful tool for predicting optimal drilling directions and wellbore profiles. The presented methodology however, still utilizes significant 'human' effort for analyzing stereonets at various locations of a deviated well path. As the 3D MEM provides all necessary input data, the next step for the presented methodology is to find an automatic process to find an optimal well trajectory for a given target location. If a full optimization application is applied, the presented methodology has been successfully shown to provide safe mud pressure windows.

5.3. SHORTCOMINGS AND FUTURE WORK

The wellbore trajectory optimization approaches presented in this thesis have shown that the safety of a wellbore is influenced by the azimuth and inclination of the wellbore. However, much of the results presented here are heavily dependent upon the quality of data and numerical models which are used. Due to the methodology used including a step in which virtual well paths coordinate data is matched with that of model data, the resolution of the model plays a large role in the quality of results. If the resolution of the model is insufficient the stress data which is mapped to the wellbore trajectory may not be accurate. As increasing the resolution of a FEM causes an increase in computational time a compromise between time and quality of data must be made.

Also critical to the accuracy of results for any methodology including rock failure analyses is the determination of proper failure criteria. Most failure criteria were developed from lab testing of specific rock types and are not completely accurate when used on differing rock types. This difference in results from failure criteria may result in completely different safety window outcomes. The exclusive use of the Mohr-Coulomb failure criterion in this thesis limits the possibilities for addressing the varying outcomes

which may result from the use of additional failure criteria. In addition to the use of a single failure criterion, the assumption that all rocks along the wellbore contain a single set of rock strength parameters significantly reduces the accuracy of results. In the anticline model for example, a sandstone-shale sequence is used in the near reservoir layer however, their strength properties which are used to calculate the operational window are identical. For completeness a unique set of strength parameter should be used for each rock encountered.

In addition to the input parameters, the methodology presented here requires a significant effort of the analyst. The analysis of stereonet projections can be tedious and may lead to significant human errors. If possible this process should be eliminated and replaced with an optimized, automated computer algorithm. The methodology presented can be optimized over the aforementioned P_{diff} variable.

Due to the increasing complexity of FE modeling, the methodology presented provides many areas for future improvements. One possible improvement is mapping realistic rock strength properties to the stress data obtained from the FE models. By assigning more realistic rock properties for each specific layer in the FE model the accuracy of the final operational window will be increased. In addition, the use of a specific failure criterion based on each type of rock could increase accuracy. Multiple studies have shown that the choice of failure criteria can significantly affect the final operating window (Ewy 1999; Tran and Abousleiman 2010; and Nawrocki 2010).

The above recommendations for improvement of this methodology will require significant software coding knowledge. The optimization process is complex and logic intensive. The use of additional failure criteria for each rock type would further increase this complexity. However, with the proper knowledge this methodology could be implemented into the source code for any FE models due to the simplicity of the nearest neighbor approach which is used in the stress mapping procedure.

6. WELLBORE INTEGRITY INTRODUCTION

6.1. OVERVIEW

While the first five chapters of this thesis focus on wellbore stability, the proceeding chapters will cover the topic of wellbore integrity. Wellbore stability typically includes topics which account for the ability to successfully drill a well to depth safely. Topics in wellbore stability often only include drill bit, formation, and drilling fluid interactions. Wellbore integrity is a general term used to describe the relative safety of a wellbore system after drilling has occurred. This includes any topics which alter the near wellbore state of stress after drilling (e.g. cementing, completions design, hydraulic fracturing, and injection). Wellbore integrity studies often include complex mechanical interactions between each of the components in the system, and may include time dependent concepts.

After a well has been successfully drilled, steel pipe known as casing, and cement are used in order to complete the well and end the drilling phase. This casing and cement sheath ensures longevity for the life of the well, protects the formation from damage, and protects any fresh water zones from being contaminated by drilling fluids or flowing hydrocarbons (Bourgoyne et al., 1986). These functions require a quality bond between casing and cement and between cement and formation. If any of the bonds fail a pathway for fluid flow may be opened and could cause disastrous effects in the well. Unfortunately many essential processes can initiate wellbore integrity issues, one of these being production. During the production process fluids are extracted from the reservoir and a pressure gradient is created in the near wellbore region which can cause damage to the cement (Fontoura et al., 2013; Addis et al., 1997). Large scale processes such as subsidence and compaction of rock layers can also cause wellbore integrity issues (Freij-Ayoub et al., 2009; Hilbert et al., 2009). In these occasions large masses of rock move causing stress changes which can be great enough to buckle or even shear the casing. If this occurs the entire well may be lost.

Another wellbore integrity challenge is faced in carbon dioxide [CO_2] sequestration projects where excess CO_2 is injected into either depleted hydrocarbon reservoirs for enhanced oil recovery (Celia et al., 2004) or into specifically selected

aquifers for geologic storage. For depleted petroleum reservoirs, the original production wells can be modified for injection (Jarrell et al., 1991). These wells are cased and the annulus is cemented. If subjected to CO_2 injection, CO_2 can leak along the casing-cement interface, along the cement-formation interface, through fractures in the cement and if casing is subject to corrosion through fractures in the cement (Celia et al., 2004). Figure 6.1 shows the 6 main pathways for fluid flow in the cement sheath (Celia et al., 2004). In addition, CO_2 is injected at surface temperature and the temperature difference at reservoir temperatures may result in cement shrinkage and debonding (Haider et al., 2012). The effects of this cold fluid injection on the integrity of casing-cement and cement-formation boundaries will be studied herein (Bois et al., 2010; Haider et al., 2012). In addition to these factors it is also important to know the age of the well which has been converted for use of storage. Often such abandoned wells have produced oil and gas for many years, and then were left stagnant for many more years. Due to this possibility the cement present in the well may be decades old and its integrity already compromised before any CO_2 injection occurs.

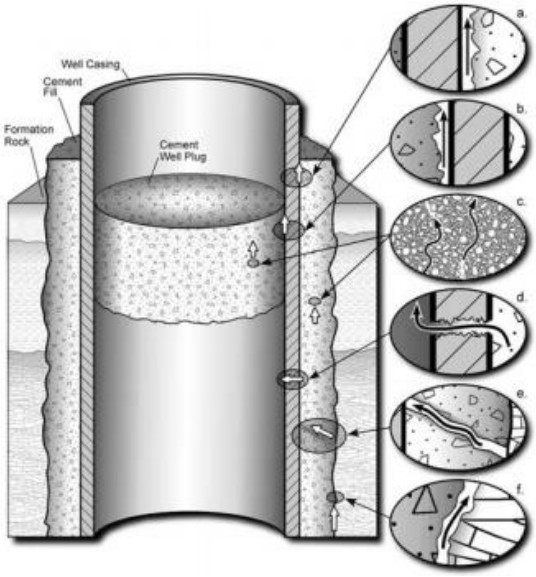

Figure 6.1. Fluid flow pathways in an abandoned well. A and B are spaces between the casing and cement due to cement debonding; C is through the pore spaces of the cement. D is through the casing; E is through fractures; and F is space between formation and cement. After Celia et al., 2004.

6.2. LITERATURE REVIEW

Cement sheath integrity plays a large role in the overall integrity of a petroleum wellbore system. An unstable cement job can lead to many hazardous situations; the worst being a blowout due to tensile failure opening pathways for hydrocarbons to flow into the annular space (Bois et al., 2010). Historically cement sheath studies had been conducted solely in a laboratory setting or by using specialized downhole tools; however, with the widespread acceptance of FE modeling cement sheath studies have been extended past the laboratory (Cooke et al. 1983). By using FE models the behavior of the cement sheath at reservoir conditions can be studied more readily (Shahri et al., 2005; Shen and Beck 2010). The finite element approach allows for more complex scenarios to be tested than is possible in laboratory studies, and when the FE models are benchmarked using laboratory obtained material properties, the results have proven to be accurate (Haider et al., 2012).

Finite element studies have proven to accurately couple many physical phenomena including wellbore temperature and pressure changes, formation pressure changes, and volume changes in the cement sheath during the curing process (Haider et. al., 2012; Patillo and Kristiansen 2002; Gray et. al., 2007 Shahri et. al., 2005). Although these models include in depth analyses of casing-cement-formation interactions, the inclusion of pre-cementing stress changes are rarely taken into account. In order to include these stress changes the use of staged finite element analyses has been proposed by some authors (Patillo and Kristiansen 2002; Bosma et. al. 2003; Gray et. al., 2007).

The intent of the staged finite element analysis is to include the most significant physical processes into one or more FE models such that any residual stresses or deformations which are caused by these physical processes are included in the final model. These models are more complex and require higher computation costs when compared to previously utilized single step FE models. In most staged FE models three main steps are included; drilling, cementing, and final completion design. In many cases these FE models follow similar work flows (Figure 6.2) but not all staged FE model

contain every step shown in Figure 6.2. Often certain assumptions are implemented/considered in order to reduce computational costs of the models.

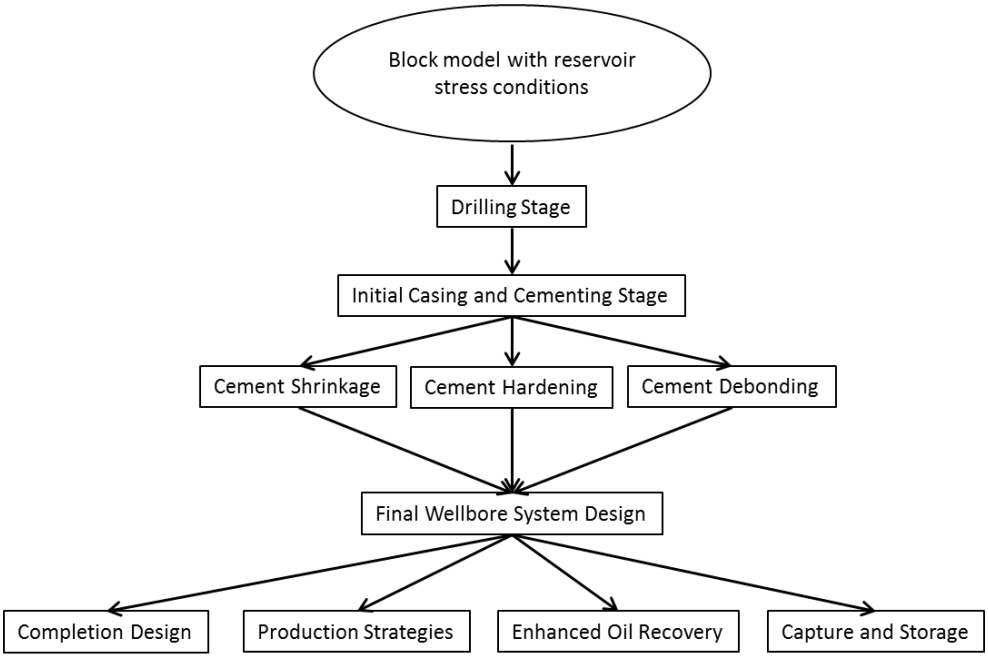

Figure 6.2. Workflow depicting common steps for a staged finite element model of a wellbore system.

Due to the complexity which arises from the phase change of cement during the curing process, multiple methods have been proposed on how to model the cementing process. In some instances certain physical processes (hardening, shrinkage, hydration, etc.) which result from, or are part of this phase change are ignored (Gray et al., 2007; Haider et al., 2012) in order to isolate a certain process. One common assumption is that the final Young's Modulus of cured cement can be directly applied to the FE model (Gray et al., 2007; Haider et al., 2012; Shen and Beck 2012). However, laboratory results have shown that as cement cures the Young's Modulus increases (Mueller and Eid 2006; Zheng et al., 2010). Mueller and Eid (2006) analyzed the elastic and strength properties of common cements during the initial stages of cement curing. Their experiments have shown that the early time physical and mechanical responses should be given ample

curing time before pressure testing is conducted in order to minimize the chances of causing failure in the cement sheath (Mueller and Eid, 2006).

Similar experiments conducted by Zheng et al. (2010) analyzed in detail the influence of the water to cement ratio on the evolution of Young's Modulus in curing cement pastes. They found that as the amount of water in a cement paste is increased, the final obtained Young's Modulus of the cement is decreased. These experiments have shown that depending on this ratio (values of 0.6 to 0.2 water content to cement), the magnitude of the drop in Young's Modulus can vary from 20MPa to <5MPa. Assuming that the pore pressure in the cement during the curing process equals the formation pore pressure an increase in the water content may result. If proper care is not taken in cement design, the cured cement may possess a lower Young's Modulus than originally designed. It should be noted that the experiments conducted by Zheng et al. (2010) initially tested cement pastes with curing times which were greater than 14 days.

Gray (2007) conducted a staged FE model using the ABAQUS^{TM} software which included the drilling and completions process. The model includes the use of multiple steps for producing in situ stresses, borehole stresses, and cement stresses. In their model the cementing stage is accomplished by placing a hydrostatic stress on the cement elements, but does not include the increase of the Young's Modulus during cement hardening. Shahri (2005) discusses the influence of differing Young's Moduli of the cement in high pressure high temperature situations. Shahri uses the effects of temperature to lower the Young's Modulus of the cement in order to decrease the tensile strength and thereby decrease the chances of tensile failure in the cement. Shen and Beck (2012) a staged FE modeling approach to study the influence of multiple formation layers on the stresses in the near wellbore region.

In this study a staged FE model of the drilling and cementing process which includes the evolution of Young's Modulus during the curing process is conducted. A sensitivity analysis of the magnitude of the change in Young's Modulus is conducted in order to determine the necessity of quality laboratory testing of cement samples during the curing process. Also included in the study are the effects of temperature change on the near wellbore region during the flow of liquid CO_2 through the wellbore. Because the temperature of liquid CO_2 is lower than the temperature of the formation, the formation

will be cooled. This decrease of temperature will be shown to produce a negative thermal stress effectively lowering the hoop stress in the cement sheath. However, the temperature change which is included in this model is non-cyclic.

The work presented in this thesis has three main limitations. The first and most significant limitation is the lack of cement shrinkage. The models presented here contain three concentric cylinders (casing, cement, and formation) which are assumed to be perfectly bonded to each other; this allows for the full use of the thick-walled cylinder assumption. This also means that any and all interactions which occur due to debonding are not included. The second limitation is the use of only a single elastic parameter to account for the entire cement hardening process. In this thesis only the Young's Modulus of the cement is changed throughout the hardening process, whereas in reality there are multiple properties which are influenced and may affect the results. The third limitation is that no laboratory testing has been completed in order to verify the properties which are used in the model. This is especially significant during the stages of Young's Modulus hardening. This thesis assumes only linear increases/decreases in Young's Modulus where if lab testing had been completed, a more accurate relationship to be adopted in the numerical simulations could have been used.

6.3. RESEARCH OBJECTIVES AND QUESTIONS

The objective of this study is to determine whether a staged FEM can be used to gain a better understanding cement sheath integrity. The staged FEM presented includes steps to simulate the drilling, cementing, curing, and temperature change of the cement sheath. The overall objective of this study can be further divided into three main sub-objectives.

(1) Create and perform a staged FE model of the near wellbore region.

(2) Determine the influence of the increase in Young's Modulus due to the cement curing influences the state of stress of the near wellbore region.

(3) Determine the influence of cement degradation, in terms of a Young's Modulus decrease, on the likelihood of cement sheath failure.

(4) Determine the influence of temperature changes due to cold fluid injection on the likelihood of cement sheath failure.

7. WELLBORE INTEGRITY BACKGROUND THEORY

The previously discussed Kirsch solutions which were used in Part I to determine wellbore failure are not valid to describe the state of stress for a scenario including cylinders of multiple materials. The original Kirsch solutions were developed for a circular hole in an infinite, single material medium. Because the near wellbore region of a completed well includes casing, cement, and formation material sets other theories such as thin-walled and thick-walled cylinder theories must be used to determine the stresses (Boresi and Schmidt 2002). Depending on the scenario which is being investigated, either of these theories or a combination of both theories may be acceptable (Boresi and Schmidt 2002). For the purposes of this thesis a modified version of the thick-walled cylinder theory is applied to the near wellbore region. This theory is considered valid based on the assumption that scenarios in which perfect bonds between the cement and casing, and cement and formation are investigated.

7.1. THERMAL STRESSES

For any material the laws of thermodynamics state that equilibrium is maintained by changing any two of the state variables. Three commonly used state variables are temperature, pressure, and density. In order to best derive stresses caused by temperature changes, the specific volume (v) will be used as opposed to its reciprocal, density.

$$v = \frac{1}{\rho} \tag{64}$$

For equilibrium the change in volume of one state variable can be related to any two other state variables. The specific volume can then be related to pressure and temperature through the following partial differential equation.

$$dv = \left(\frac{\partial v}{\partial T}\right)_p dT + \left(\frac{\partial v}{dp}\right)_T dp \tag{65}$$

where the subscripts on the partial derivatives signify the property which is held constant.

Equation 65 contains two common thermodynamic quantities; the isothermal compressibility (β) and the volumetric coefficient of thermal expansion (α_v). These properties are typically obtained through laboratory testing.

$$\beta = -\frac{1}{v}\left(\frac{\partial v}{dp}\right)_T \tag{66}$$

$$\propto_v = \frac{1}{v}\left(\frac{\partial v}{\partial T}\right)_p \tag{67}$$

By substituting Equation 66 and 67 into equation 65 we obtain.

$$dv = -v\beta dP + v\alpha_v dT \tag{68}$$

Assuming that the pressure change with respect to a temperature and volume change is zero, the following equations can be determined.

$$dv = v\alpha_v dT \tag{69}$$

$$d\rho = -\rho\alpha_v dT \tag{70}$$

The above equations show that as the temperature of a material is altered a resulting volume change will occur. The changes in volume will later be related to strains.

By assuming that the material is confined so that no volume changes occur, Equation 68 reduces to:

$$dp = \frac{\alpha_v}{\beta} dT \tag{71}$$

Equation 71 shows that a change in temperature causes a corresponding change in the pressure. This pressure can be considered an isotropic stress.

If equation 71 is written in terms of small increments, the equation can be rewritten as follows:

$$\Delta V = v\alpha_v \Delta T \tag{72}$$

where ΔV and ΔT are a change in volume and change in temperature respectively.

This change in volume can also be related to the principal strains such that:

$$\varepsilon_1 = \varepsilon_2 = \varepsilon_3 = -\alpha_l \Delta T \tag{73}$$

where α_l is the linear coefficient of thermal expansion and is one-third α_v.

If both elasticity and thermal effects are taken into consideration the total strains will be the algebraic addition of the elastic strains (found by inverting Eqs 7-9) and the thermal strains (Eqs 73).

$$\varepsilon_{xx} = \frac{1}{E}\left[\sigma_{xx} - v(\sigma_{yy} + \sigma_{zz})\right] + \alpha_l \Delta T \tag{74}$$

$$\varepsilon_{yy} = \frac{1}{E}\left[\sigma_{yy} - v(\sigma_{xx} + \sigma_{zz})\right] + \alpha_l \Delta T \tag{75}$$

$$\varepsilon_{zz} = \frac{1}{E}\left[\sigma_{zz} - v(\sigma_{xx} + \sigma_{yy})\right] + \alpha_l \Delta T \tag{76}$$

In terms of the stresses Equations 74-76 can be written as:

$$\sigma_{xx} = \frac{E}{(1+v)(1-2v)}\left[\varepsilon_{xx}(1-v) + \varepsilon_{yy}v + \varepsilon_{zz}v\right] - \frac{E\alpha_l \Delta T}{1-2v} \tag{77}$$

$$\sigma_{yy} = \frac{E}{(1+v)(1-2v)}\left[\varepsilon_{xx}v + \varepsilon_{yy}(1-v) + \varepsilon_{zz}v\right] - \frac{E\alpha_l\Delta T}{1-2v} \quad (78)$$

$$\sigma_{zz} = \frac{E}{(1+v)(1-2v)}\left[\varepsilon_{xx}v + \varepsilon_{yy}v + \varepsilon_{zz}(1-v)\right] - \frac{E\alpha_l\Delta T}{1-2v} \quad (79)$$

It is important to note that the thermal stress portions of equations 77-79 are only valid for situations where steady state temperature flow has been achieved. The equations for transient flow which include a time dependent component of temperature in space are more complex. An in depth review of how transient thermal stress analyses of composite cylinders is given by Kandil et al., (1994).

7.2. THICK-WALLED CYLINDER STRESSES.

The theory of stresses present in a thick-walled cylinder (Boresi and Schmidt 2002) is used to determine the three principal stresses which occur due to the presence of any combination of outer and inner pressures placed upon the cylinder. These principal stresses are the hoop stress, radial stress, and the axial stress. The influence of temperature change on the stresses can also be solved using this theory.

The thick-walled cylinder stress theory was first derived by Lame' in the 19th century (Boresi and Schmidt 2002). The derivation used here follows Boresi et. al. (2002) and is defined using the cross section of a loaded cylinder as given in Figure 7.1. The loading conditions include both an inner and outer pressure; P_i and P_o respectively, and a change in temperature ΔT.

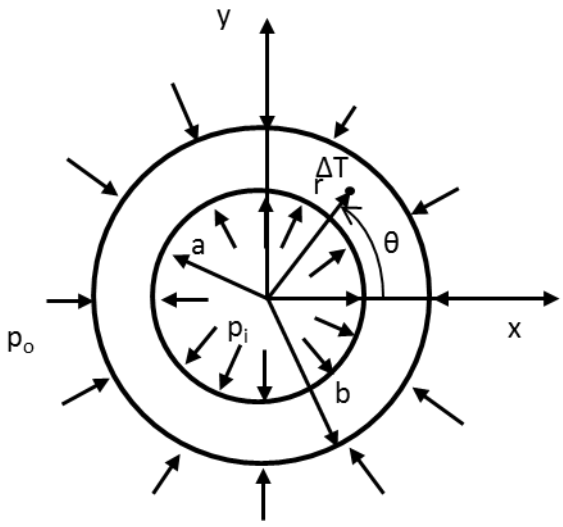

Figure 7.1. Depiction of thick walled cylinder with outer and inner pressures acting on the cylinder walls.

Using a volume in cylindrical coordinates we can determine that the shear stresses and normal stresses acting on the volume are a function of the radius of investigation (r), and that non-zero stress components comprise the entire principal stress tensor. The equations of equilibrium in cylindrical coordinates (Eqs 56-58) and stress-strain-temperature data can be used to determine the magnitude of these principal stresses as functions of the radius of investigation.

By neglecting body forces in the equations of equilibrium the force equilibrium in the radial direction gives:

$$r\frac{d\sigma_{rr}}{dr} = \sigma_{\theta\theta} - \sigma_{rr} \tag{80}$$

and the strain-displacement relations can defined as:

$$\varepsilon_{rr} = \frac{\partial u}{\partial r} \tag{81}$$

$$\varepsilon_{\theta\theta} = \frac{u}{r} \tag{82}$$

$$\varepsilon_{zz} = \frac{\partial w}{\partial z} \tag{83}$$

where u=u(r,z) and w = w(r,z) are displacement components in the r and z directions.

By investigating a portion of the cylinder which is far removed from the ends in the *z* direction, the responses of *u* and *w* in the z direction can be considered negligible. Further assuming that ε_{zz} is constant, the above equations reduce to:

$$\frac{d}{dr}(r\varepsilon_{\theta\theta}) = \varepsilon_{rr} \tag{84}$$

where equation 84 is the strain compatibility equation for a thick-walled cylinder.

Introducing the concept of thermal stresses into cylindrical coordinates we find that:

$$\varepsilon_T = \alpha\Delta T \tag{85}$$

where ε_T is the thermal strain caused by a temperature change in an isotropic material.

If the material of the cylinder is considered to be isotropic and behaves linear elastically, Hooke's law may be used to determine the linear stress-strain relationship of the material. Using the relationship between elastic moduli, changing coordinate systems, Equations 74-76 can be rewritten in the following way.

$$\varepsilon_{rr} = \frac{1}{E}[\sigma_{rr} - \nu(\sigma_{zz} + \sigma_{\theta\theta})] + \alpha\Delta T \tag{86}$$

$$\varepsilon_{\theta\theta} = \frac{1}{E}[\sigma_{\theta\theta} - \nu(\sigma_{rr} + \sigma_{zz})] + \alpha\Delta T \tag{87}$$

$$\varepsilon_{zz} = \frac{1}{E}[\sigma_{zz} - v(\sigma_{rr} + \sigma_{\theta\theta})] + \alpha\Delta T = constant \tag{88}$$

By inserting Equations 86 and 87 into Equation 84 we are able to express σ_{rr}, σ_{zz}, and $\sigma_{\theta\theta}$ in terms of their derivatives with respect to r. While equation 88 with constant can be used to eliminate the derivative of σ_{zz} with respect r from the equation. Lastly the equation 80 can be used to eliminate the σ_{rr}- $\sigma_{\theta\theta}$ factors leaving:

$$\frac{d}{dr}\left(\sigma_{rr} + \sigma_{\theta\theta} + \frac{\alpha E \Delta T}{1 - v}\right) = 0 \tag{89}$$

Double integration and elimination of the hoop stress in the above equation from the inner radius (a) to a radius of investigation (r) results in:

$$\sigma_{rr} = -\frac{\alpha E}{r^2(1 - v)}\int_a^r \Delta T r dr + \left(1 - \frac{a^2}{r^2}\right)C_1 + \frac{C_2}{r^2} \tag{90}$$

where C_1 and C_2 are constants of integration.

Substituting the results of the double integration (Equation 90) into the results of the single integration the relationship for the hoop stress in terms of the integration constants can be determined.

$$\sigma_{\theta\theta} = \frac{\alpha E}{r^2(1 - v)}\int_a^r \Delta T r dr - \frac{\alpha E \Delta T}{1 - v} + \left(1 - \frac{a^2}{r^2}\right)C_1 + \frac{C_2}{r^2} \tag{91}$$

Applying the boundary conditions below the integration constants C_1 and C_2 can be found:

$$\sigma_{rr} = -P_1 \ @ \ r = a \tag{92}$$

$$\sigma_{rr} = -P_2 \ @ \ a = b \tag{93}$$

$$C_1 = \frac{1}{b^2 - a^2}\left(P_1 a^2 - P_2 b^2 + \frac{\alpha E}{1 - v}\int_a^b \Delta T r dr\right) \quad (94)$$

$$C_2 = -P_1 a^2 \quad (95)$$

7.3. COMPOSITE CYLINDER THEORY

While the theory for thick-walled cylinders is a good representation to explain the stresses which are acting on a cylinder made of a single material, it must be modified in order to be applied to any system which contains more than one material. A thick cylinder which is composed of two concentric cylinders made of different materials is known as a composite cylinder. The stresses acting anywhere in a composite cylinder can be found by solving the thick walled cylinder theory in two parts, and considering how the pressures acting on the cylinder create displacements on the inner and outer surfaces of the cylinder (Boresi and Schmidt 2002). This theory can be used to explain the hoop and radial stresses for the casing-cement-formation sheath (Figure 7.2; Haider et al., 2012). The theory developed by Haider et al. (2012) assumes that the casing behaves as a thin cylinder. Since a perfect bond between casing and cement is assumed, the casing, cement, and formation will all behave as a thick cylinder.

The first scenario which is taken into account is one which contains only a pressure (P_i) on the inner surface of the casing. This pressure causes displacements to occur on both the casing-cement and cement-formation boundaries (Figure 7.2).

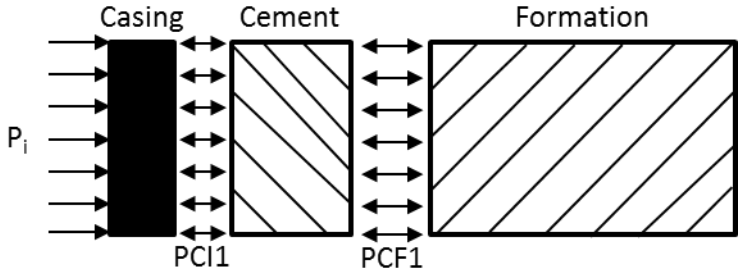

Figure 7.2. Axi-symmetric wellbore cylinder with internal pressure only. Figure after Haider et al. (2012).

For this scenario of internal pressure only the displacement at the interfaces can be calculated as follows:

$$d_{cc1} = -\frac{a}{E_s}\left[\left(\frac{b^2+a^2}{b^2-a^2}(1-v_s^2) - (v_s+v_s^2)\right)PCI1 - \frac{2P_i b^2}{b^2-a^2}\right] - b(1+v_s)\alpha_s \Delta T_s \quad (96)$$

$$d_{cc2} = \frac{b}{E_c}\left[\frac{b^2+c^2-2b^2v_c^2+c^2v_c-b^2v_c}{(c^2-b^2)}\mathrm{PCI1} - \frac{2c^2(1-v_c^2)}{c^2-b^2}PCF1\right] + b(1+v_c)\alpha_c \Delta T_c \quad (97)$$

$$d_{cf1} = \frac{c}{E_c}\left[\frac{2b^2(1-v_c^2)}{c^2-b^2}PCI1 + \frac{2c^2v_c^2+c^2v_c-b^2v_c-b^2-c^2}{c^2-b^2}PCF1\right] \quad (98)$$

$$d_{cf2} = \frac{c}{E_f}\left[PCF1\frac{d^2+c^2}{d^2-c^2}\left(1-v_f^2\right) + PCF1(v_f+v_f^2)\right] \quad (99)$$

where d_{cc1}, d_{cc2}, d_{cf1}, and d_{cf2} are the displacements at the casing and cement for the casing, the displacement at the casing and cement for the cement, displacement at the cement and formation for the cement, and the displacement at the cement and formation for the formation caused by the internal pressure respectively. PCI1 is the contact

pressure between the casing and cement caused by the inner pressure. PCF1 is the contact pressure between the cement and formation caused by the inner pressure. E_s, E_c, and E_f is the Young's moduli for the casing, cement, and formation respectively; ν_s, ν_c, and ν_f is the Poisson's ratios for the casing cement and formation respectively; α_s and α_c is the linear thermal expansion coefficients of the casing and cement respectively; a, b, c, d is the casing internal radius, cement internal radius, formation internal radius, and formation external radius respectively; and ΔT_s and ΔT_c is a uniform temperature change in the casing and cement respectively. The detailed derivation of Equations 96-99 can be found in (Haider et al., 2012).

By assuming a perfect bond between both the casing-cement and cement-formation, compatibility of the displacements must hold true. By considering compatibility, Equations 96 and 97 can be set equal; likewise Equations 98 and 99 can be set equal to each other. The resulting equations can be used to determine PCI1 and PCF1.

The second scenario which is taken into account is one which contains only a pressure (P_f) on the outer surface of the formation. This pressure also causes displacements to occur on both the casing-cement and cement-formation boundaries (Figure 7.3).

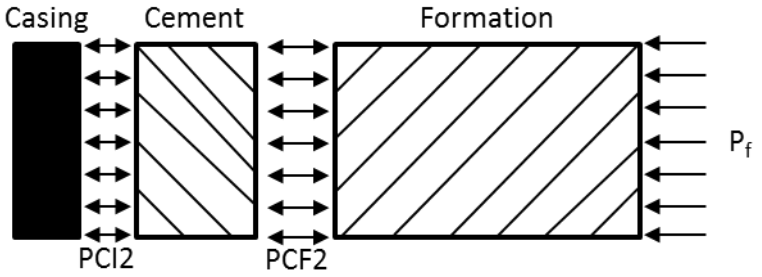

Figure 7.3. Axi-symmetric wellbore cylinder with external pressure only. After Haider et al., (2012).

For this scenario of external pressure only the displacements at the interfaces can be calculated as follows:

$$d_{cc3} = -\frac{a}{E_s}\left[\left(\frac{b^2+a^2}{b^2-a^2}(1-v_s^2)\mathrm{PCI2} - \mathrm{PCI1}(v_s+v_s^2)\right)\right] - b(1+v_s)\alpha_s\Delta T_s \quad (100)$$

$$d_{cc4} = \frac{b}{E_c}\left[\frac{b^2+c^2-2b^2v_c^2+c^2v_c-b^2v_c}{c^2-b^2}PCI2 - \frac{2c^2(1-v_c^2)}{c^2-b^2}PCF2\right] \quad (101)$$

$$d_{cf3} = \frac{c}{E_c}\left[\frac{2b^2(1-v_c^2)}{c^2-b^2}PCI2 + \frac{2c^2v_c^2+c^2v_c-b^2v_c-b^2-c^2}{c^2-b^2}PCF2\right] + c(1+v_c)\alpha_c\Delta T_c \quad (102)$$

$$d_{cf4} = \frac{c}{E_f}\left[\left(\frac{d^2+c^2}{d^2-c^2}\left(1-v_f^2\right)+(v_f+v_f^2)\right)PCF2 - P_f\frac{2d^2}{d^2-c^2}\right] + c(1+v_f)\alpha_f\Delta T_f \quad (103)$$

where d_{cc3}, d_{cc4}, d_{cf3}, and d_{cf4} are the displacement at the casing and cement for the casing, the displacement at the casing and cement for the cement, the displacement at the cement and formation for the cement, and the displacement at the casing and formation for the formation caused by the external pressure respectively. PCI2 is the contact pressure between the casing and cement caused by the external pressure. PCF2 is the contact pressure between the cement and formation caused by the external pressure. ΔT_f and α_f are the uniform temperature change in the formation, and the linear thermal expansion of the formation respectively.

By considering compatibility, PCI2 and PCF2 can be determined from the displacement equations. In order to determine the pressures which would be caused by the existence of both an internal and external pressure on the system, the principle of superposition can be used. The superposition of the contact pressures results in the following expressions:

$$PCI = PCI1 + PCI2 \quad (104)$$

$$PC2 = PCF1 + PCF2 \tag{105}$$

where PC1 and PC2 are the superposition of the contact pressures at the casing-cement and cement-formation boundaries respectively.

The new contact pressures which have been obtained can now be used in the Lame' equations for a hollow cylinder (Haider et al., 2012). These equations are used to determine the radial stress (σ_{rr}), hoop stress ($\sigma_{\theta\theta}$), and axial stress (σ_{zz}) for the cement elements in a composite cylinder which has been subjected to both an internal and external pressure.

$$\sigma_{rr} = \frac{PC1b^2 - PC2c^2}{c^2 - b^2} - \frac{b^2c^2}{r^2(c^2 - b^2)}(PC1 - PC2) \tag{106}$$

$$\sigma_{\theta\theta} = \frac{PC1b^2 - PC2c^2}{c^2 - b^2} + \frac{b^2c^2}{r^2(c^2 - b^2)}(PC1 - PC2) \tag{107}$$

$$\sigma_{zz} = \frac{PC1b^2 - PC2c^2}{c^2 - b^2} \tag{108}$$

where r is the radius of investigation.

8. WELLBORE INTEGRITY TECHNICAL APPROACH

8.1. WELLBORE MODEL APPROACH

8.1.1. Mapped-Meshing Approach. A mapped-meshing approach (Mitchell, 1997) is used for the wellbore model in order to create elements of a specific shape and size. This meshing approach allows for the use of a fine circular mesh in the near-wellbore region in order to have many elements in close proximity to the wellbore wall. The mesh used in this report represents a modified version from the results found by Lee (2011), where studies on the required near wellbore region mesh size are conducted. Because the state of stress is uniform in the far-field region the mesh density does not need to be as high as it does in the near wellbore region, however the far field region has been extended in this model to reduce any influence the boundary may exert on the temperature flow. The horizontal dimensions in the x-y plane of the model are shown in Figure 8.1a and 8.1b. It should also be noted that the model is 3 dimensional and extends 2m into the z-direction. Figure 8.1c shows the immediate vicinity of the wellbore and the mesh features different element sets for the casing, the cement and the formation.

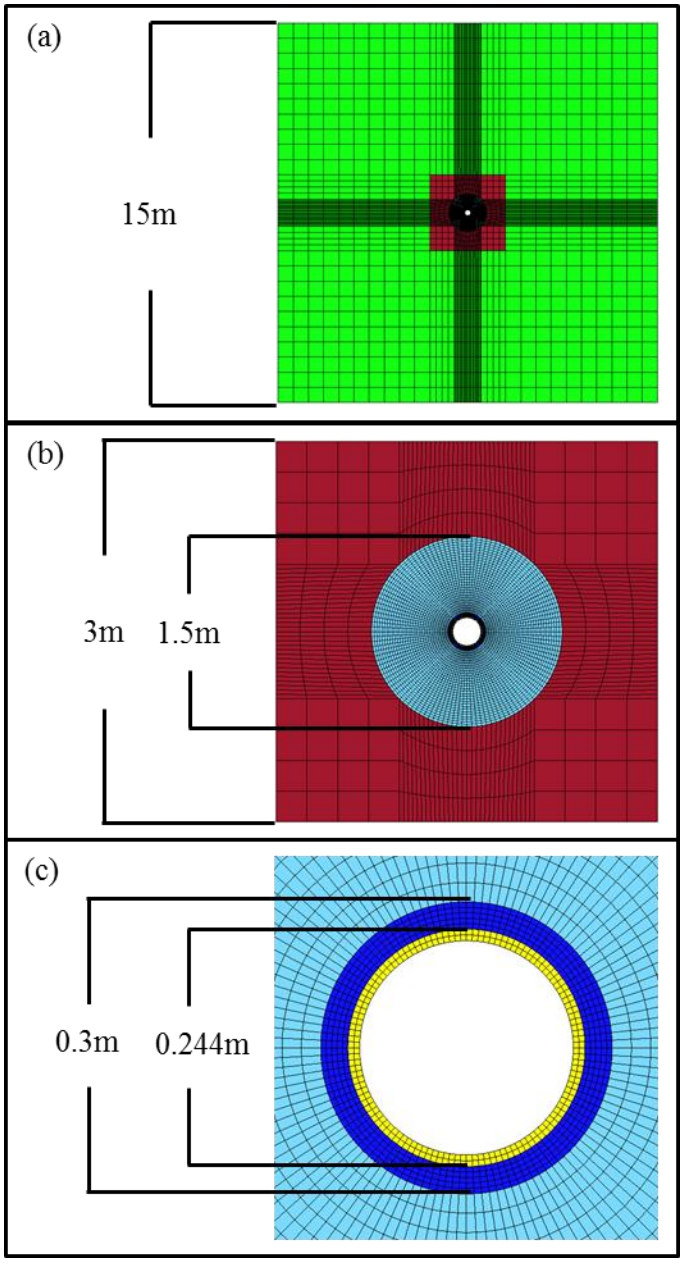

Figure 8.1. Top view of the mapped mesh used in the wellbore model (a). Mesh dimensions of the near wellbore region of the mapped mesh (b). Close up view of the casing and cement mesh (c).

8.1.2. Staged FE Model Approach. The wellbore model geometry (Figure 8.1) is used to simulate the drilling process as close to reality as possible. The analysis is run in multiple steps listed in the following section. The model material parameters are given in Table 8.1. The model geometry and basic boundary condition setup is shown in Figure

8.2. The appropriate vertical stress and horizontal stresses are achieved by applying initial stress conditions to the model. Pore pressure is assumed to be hydrostatic. For all models the vertical and horizontal model boundaries displacements are constrained (i.e. roller boundary condition; Figure 8.2c). The loading section of the ABAQUS™ input file is given in the Appendix. It should be noted that in the staged FE modeling approach used here cement shrinkage during the hardening process is not considered.

Table 8.1. Material properties for the casing, cement, and formation elements in the wellbore model.

Material Properties					
Property	**Units**	**SandStone**	**Cement**	**Casing**	**Pore Fluid**
Density (ρ)	kg/m^3	2300	2300	7800	1000
Young's Modulus (E)	GPa	15	20	200	X
Poisson's Ratio (ν)	unitless	0.3	0.3	0.3	X
Hydraulic Conductivity	m/s	1.00E-06	1.00E-06	X	X
Thermal Expansion	$1/^oC$	1.00E-06	9.50E-05	1.10E-06	5.00E-05
Specific Heat	$J/(kg^oC)$	1380	1380	490	4190
Thermal Conductivity	$J/(ms^oC)$	0.29	0.29	43	0.29

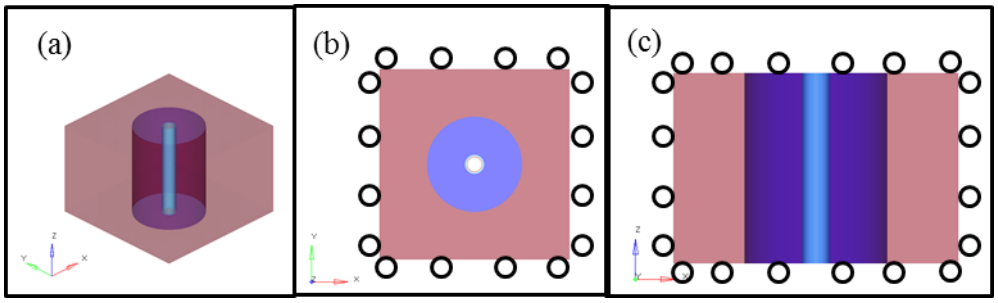

Figure 8.2. Full 3D view of the wellbore model (a). Top view of the wellbore model with boundary conditions (b). Side view of the wellbore model with boundary conditions (c).

8.1.2.1 Step one: Formation stress (Figure 8.3). In the first step the entirety of the model consists of a single block of sandstone with initial stress conditions and roller boundary conditions on each external face are imposed in order to create the appropriate

stress regime (Figure 8.3). For this study an extensional stress regime is used. The stresses were obtained from the crest of the anticline model which was used in Part I of this thesis and can be found in the Appendix. Equation 109 shows the principal stress tensor which is applied to the model.

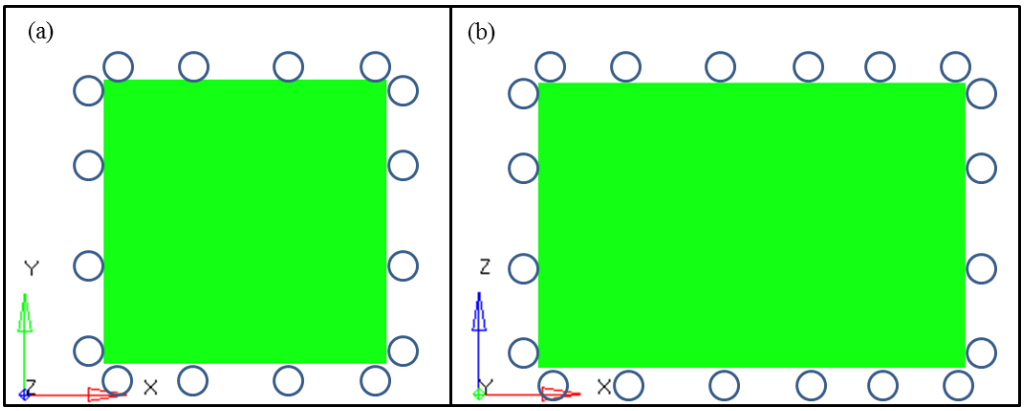

Figure 8.3. (a) top view of the block model roller boundary conditions on both the x and y coordinate directions. (b) Side view of the roller boundary conditions on the z and x axes.

$$\boldsymbol{\sigma} = \begin{bmatrix} 27 & 0 & 0 \\ 0 & 18.2 & 0 \\ 0 & 0 & 11.97 \end{bmatrix} (MPa) \tag{109}$$

8.1.2.2 Step two: Drilling I (Figure 8.4). The second step in the model is used to simulate drilling of the wellbore. During this step the inner wellbore, casing, and cement elements are removed from the model geometry. The lateral and vertical boundary conditions remain constant. At the end of step two the model consists of only rock elements, including a circular hole in the center of the model which represents the wellbore. After the wellbore is drilled the only boundary condition imposed on the new geometry are in the vertical direction. The inner elements are free to move in the x-y plane.

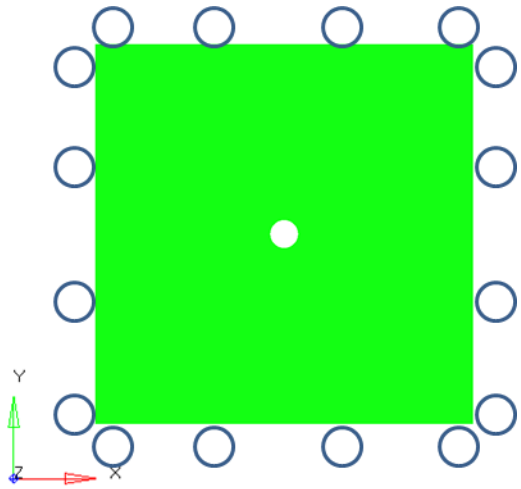

Figure 8.4. Top view of the model directly after the drilling process of Step 1 has occurred.

8.1.2.3 Step three: Drilling II (Figure 8.5). In step three a mud pressure (P_i) is applied to the inner surface of the borehole. In this step we are considering a balanced drilling approach where the mud pressure (P_i) is equal to the pore pressure (P_p), here 14.46MPa. This system represents an open-hole borehole system including mud pressure and pore pressure and the borehole state of stress can be calculated by Equations 28-33 in section 2.6.1.

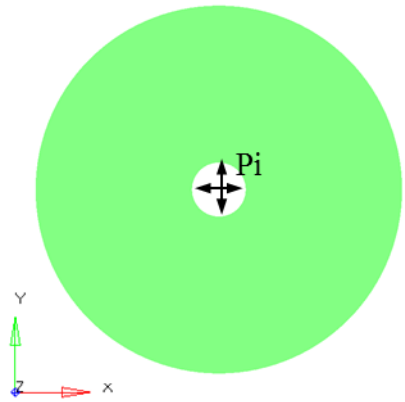

Figure 8.5. Top view of the near wellbore area depicting the mud pressure (Pi) which is acting on the wellbore wall.

8.1.2.4 Step four: Casing (Figure 8.6). In step four two main procedures are occurring: first the casing elements are reinserted into the model (Figure 8.6) , and second the same mud pressure which was applied to the inner borehole is now also applied to the inner and outer surfaces of the casing elements. This step thus represents the setting of the casing.

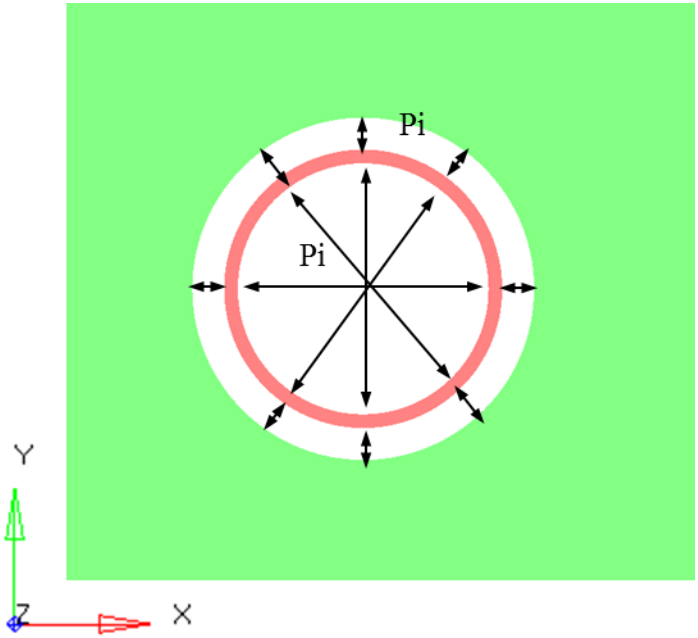

Figure 8.6. Top view after casing has been set. The mud pressure (Pi) is now acting on the inner casing, outer casing, and on the formation elements.

8.1.2.5 Step five: Cementing (Figures 8.7-8.9). The final step in the procedure consists of the simulation of the cementing phase. During this step multiple pressure loading conditions are applied. These pressure loadings are used to simulate the change in internal wellbore (i.e. mud) pressures which are acting on the formation and casing elements during the cementing stage. The first of these steps increases the pressure on the inner casing (Figure 8.7), followed by a step with an increase of mud weight on the outer casing and formation wall to simulate a fluid pressure equal to a hydrostatic column of cement (Figure 8.8). The cement pressure (P_{ce}) used in this thesis is 20MPa. The final

stage in this process is to decrease the mud weight on the inner casing section in order to simulate a mud pressure being applied to continue drilling deeper (Figure 8.9).

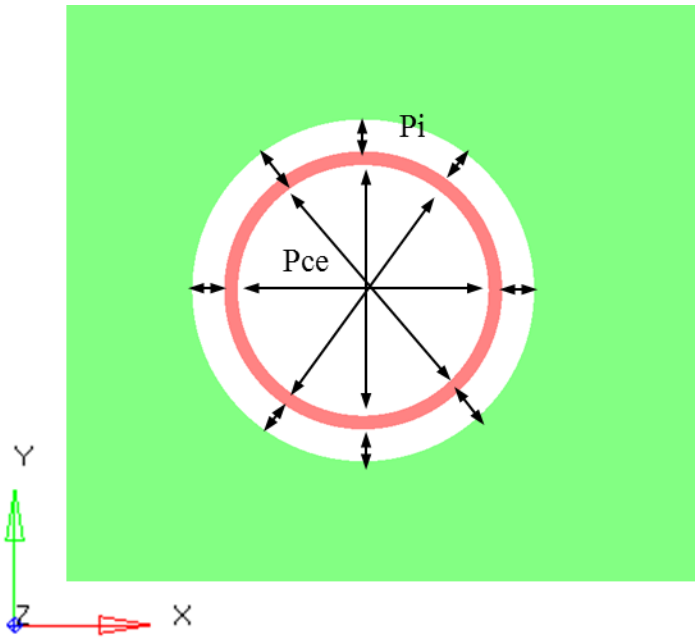

Figure 8.7. Top view of part one of Step five where the pressure on the inner casing is from the cement, while the pressure on the outer casing and formation is still from the mud.

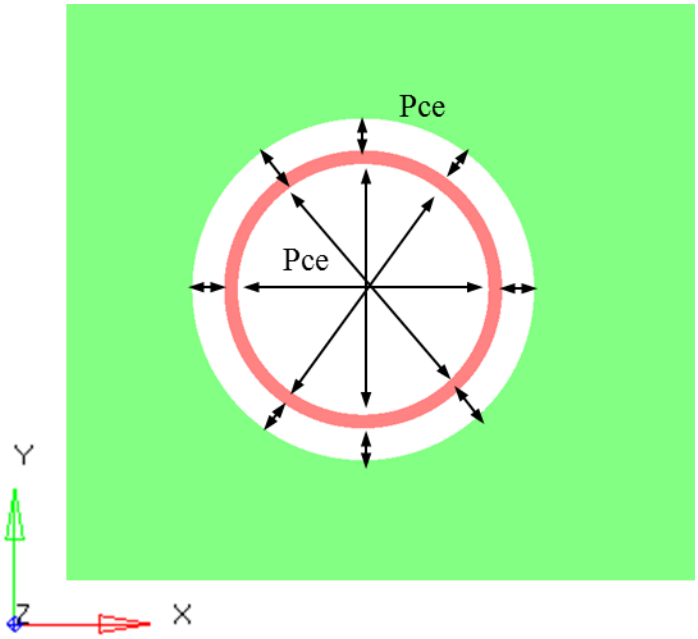

Figure 8.8. Top view of part two of Step five where the cement has displaced the mud in the annular space; all pressures are from the cement in this phase.

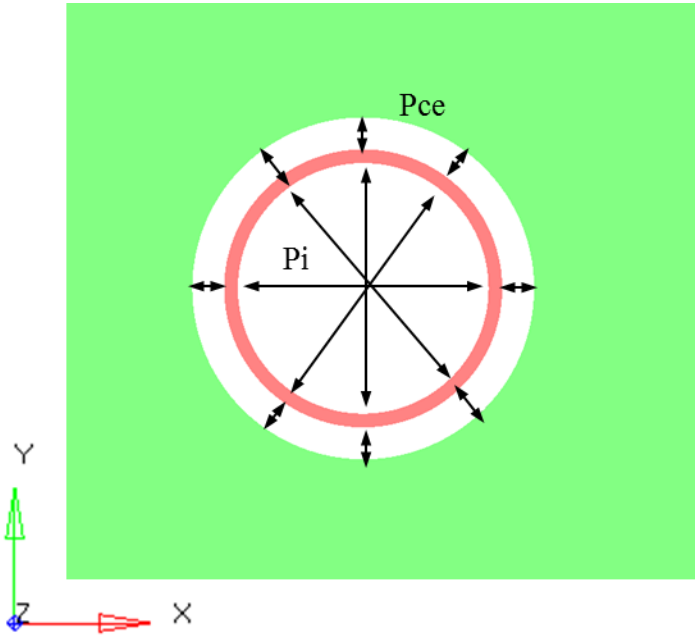

Figure 8.9. Top view of part three of Step five where mud is once again acting on the inner casing surface and the cement proceeds to act on the outer casing and formation face.

With the complete state of stress simulated using the staged FE modeling approach, the stresses for each stage can be exported for use in further analyses. The physical processes which are further investigated and use the stresses obtained from the staged FE model are cement hardening, cement degradation, and CO_2 flow through the wellbore. Figure 8.10 shows the final model which is used in this thesis. This model uses the stresses from the staged FE model as initial stress conditions, along with including initial stresses in the cement elements in which all three principal stresses are equal to the hydrostatic pressure of the cement slurry.

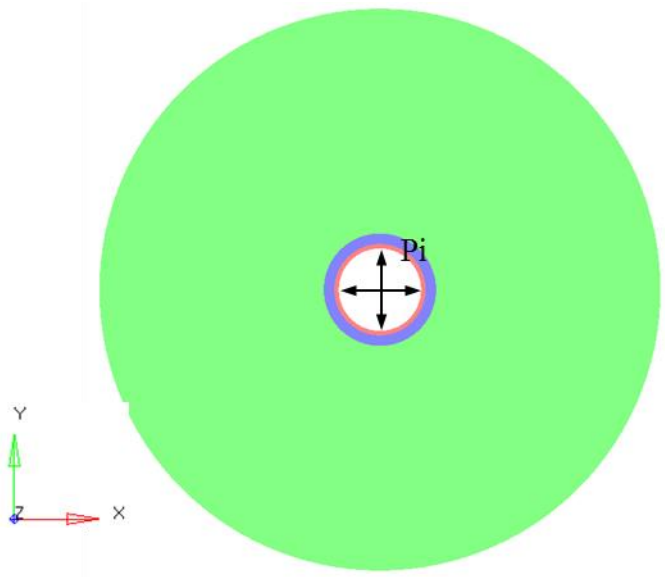

Figure 8.10. Top view of the final model in which the cement elements are added and pre-stressed. This model is then used to perform analyses on the cement hardening and degradation processes.

8.2. CEMENT HARDENING AND DEGRADATION

As cement paste cures and hardens the Young's Modulus increases while the Poisson's ratio has small variations (Mueller and Eid 2006). This process has been implemented in the wellbore scale model by including a time dependency on the Young's Modulus of the cement elements. This allows for testing the importance of Young's Modulus evolution on the state of stress in the cement sheath. The evolution of Young's

Modulus is generally found to follow a parabolic curve, but for this study a linear relationship is assumed for all models.

After the cement is considered fully cured the Young's Modulus remains constant until a process occurs that causes the cement to degrade. Mechanical examples of these could be caused by stress changes due to mud pressure, temperature, or pore pressure variations (Bois et al., 2010). These processes can cause dynamic changes in the local stress field which over time can influence the strength parameters of the cement. Although the aforementioned processes occur on a local scale certain large scale geologic occurrences such as earthquakes can also significantly influence cement sheath strength. In some situations where fluids have leached into the cement sheath chemical reactions may completely dissolve bonds weakening the cement. This is known as chemical degradation (Bois et al., 2010). Due to the inherent complexity of the subsurface, and the processes which occur within, the actual phenomena which degrade the cement sheath influence many properties other than the Young's Modulus, but these are out of the scope of this thesis.

8.3. CASING STRESS VERIFICATION

After each section of wellbore is successfully drilled casing strings are placed in the hole in order to protect the overlying formations from damage. During the first phase of this process the casing strings are lowered into the hole. As the casing is lowered a mud pressure is acting on both the inner and outer portions of the casing, and the vertical stress which would be caused by the weight of the casing is counteracted by buoyant forces. Because the same mud is acting both on the inside and outside of the pipe, there is an equal pressure on both the inside and outside of the pipe. For the purposes of this thesis the buoyant forces will be assumed to equal the total weight of the casing eliminating any axially stresses caused by the pipe weight. In this situation the stresses which are present in the casing can be characterized using the simplified thick-walled cylinder theory where the radial (σ_{rr}) and hoop ($\sigma_{\theta\theta}$) stresses can be defined as follows:

$$\sigma_{rr} = \frac{(P_i r_i^2 - P_o r_o^2)}{(r_o^2 - r_i^2)} + \frac{r_i^2 r_o^2 (P_o - P_i)}{r^2 (r_o^2 - r_i^2)} \tag{110}$$

$$\sigma_{\theta\theta} = \frac{(P_i r_i^2 - P_o r_o^2)}{(r_o^2 - r_i^2)} - \frac{r_i^2 r_o^2 (P_o - P_i)}{r^2 (r_o^2 - r_i^2)} \tag{111}$$

where P_i is the pressure on the inner surface, P_o is the pressure on the outer surface, r_i is the inner radius, r_o is the outer radius, and r is the radius to the point of investigation.

After the casing string is lowered into the hole, it is set permanently in place by pumping cement into the annular space between the casing and formation. During this process multiple inner and outer pressure scenarios are placed on the casing. The first of these scenarios occurs after enough cement has been pumped into the well to displace the drilling fluid inside the casing, but has not displaced the mud in the annular space between the casing and formation. In this scenario the pressure exerted on the inside of the casing is greater than the pressure exerted on the outside of the casing. The next scenario occurs as more cement has been pumped into the hole such that the mud in the annular space has been displaced by cement. In this stage the inner and outer pressures on the casing are equal in magnitude, as they were before the cement was pumped into the hole, but are of greater magnitude due to the increased density of the cement slurry compared to the drilling fluid. In the fourth and final scenario any cement remaining in the cased borehole is displaced by drilling fluid for a given amount of time for the cement to cure before drilling continues. In this scenario the pressure on the outside of the casing will be greater than the pressure on the inside of the casing.

Each of the above mentioned scenarios has been tested and values verified using a simple 3D FEM of a section of casing string. The properties used for the casing elements are given in Table 8.1. The results are compiled in the following four tables. For each of the scenarios a data point at the centroid of an element on both the inner and outer casing surface was chosen in order check whether the model results matched the analytical solution if the distance from the midpoint of the cylinder is extended.

The results (Tables 8.2-8.5) show that for all stages during the cementing stage the numerical modeling results match the analytical solution and the errors obtained are less than 1%.

Table 8.2. Results from model with casing inner pressure (10 MPa) casing outer pressure (20 MPa).

Casing Inner Pressure (10 MPa) Casing Outer Pressure (20 MPa)							
Model				**Analytical**			
r = 0.113 (m)		r = 0.119 (m)		r = 0.113 (m)		r = 0.119 (m)	
σ_{rr} =	-10.0 (MPa)	σ_{rr} =	-10.0 (MPa)	σ_{rr} =	-10.0 (MPa)	σ_{rr} =	-10.0 (MPa)
$\sigma_{\theta\theta}$ =	-10.0 (MPa)	$\sigma_{\theta\theta}$ =	-10.0 (MPa)	$\sigma_{\theta\theta}$ =	-10.0 (MPa)	$\sigma_{\theta\theta}$ =	-10.0 (MPa)

Table 8.3. Results from model with casing inner pressure (20 MPa) and outer pressure (10 MPa).

Casing Inner Pressure (20 MPa) and Outer Pressure (10 MPa)							
Model				**Analytical**			
r = 0.113 (m)		r = 0.119 (m)		r = 0.113 (m)		r = 0.119 (m)	
σ_{rr} =	-17.2 (MPa)	σ_{rr} =	-12.2 (MPa)	σ_{rr} =	-17.2 (MPa)	σ_{rr} =	-12.2 (MPa)
$\sigma_{\theta\theta}$ =	84.2 (MPa)	$\sigma_{\theta\theta}$ =	79.2 (MPa)	$\sigma_{\theta\theta}$ =	84.1 (MPa)	$\sigma_{\theta\theta}$ =	79.1 (MPa)

Table 8.4. Results from model with casing inner pressure (20 MPa) and outer pressure (20 MPa).

Casing Inner Pressure (20 MPa) and Outer Pressure (20 MPa)							
Model				**Analytical**			
r = 0.113 (m)		r = 0.119 (m)		r = 0.113 (m)		r = 0.119 (m)	
σ_{rr} =	-20.0 (MPa)	σ_{rr} =	-20.0 (MPa)	σ_{rr} =	-20.0 (MPa)	σ_{rr} =	-20.0 (MPa)
$\sigma_{\theta\theta}$ =	-20.0 (MPa)	$\sigma_{\theta\theta}$ =	-20.0 (MPa)	$\sigma_{\theta\theta}$ =	-20.0 (MPa)	$\sigma_{\theta\theta}$ =	-20.0 (MPa)

Table 8.5. Results from model with casing inner pressure (20 MPa) and outer pressure (10 MPa).

Casing Inner Pressure (20 MPa) and Outer Pressure (10 MPa)							
Model				**Analytical**			
r = 0.113 (m)		r = 0.119 (m)		r = 0.113 (m)		r = 0.119 (m)	
σ_{rr} =	-17.2 (MPa)	σ_{rr} =	-12.2 (MPa)	σ_{rr} =	-17.2 (MPa)	σ_{rr} =	-12.2 (MPa)
$\sigma_{\theta\theta}$ =	84.2 (MPa)	$\sigma_{\theta\theta}$ =	79.2 (MPa)	$\sigma_{\theta\theta}$ =	84.1 (MPa)	$\sigma_{\theta\theta}$ =	79.1 (MPa)

8.4. CEMENT SHEATH STRESS VERIFICATION

The cement sheath stresses have been verified using the composite cylinder theory given in Section 7.3. In order to verify these equations a simplified version of the wellbore model is used. This simplified model consists of three concentric cylinders of unique materials; the inner most cylinder has steel properties, the middle cylinder has cement properties, and the exterior has sandstone properties (Figure 8.10). The values for these properties can be found in Table 8.1. This 3D cylinder model was used in order to apply and understand the magnitudes for inner and outer pressures as required for the composite cylinder theory equations.

The derivation of the composite cylinder stresses given in Section 7.3 is only valid for the middle (cement) cylinder (Haider et al., 2012). Figure 8.11 shows the results of the hoop and radial stresses given at the centroid of the cement elements for the verification model. The plot shows that the FEM predicts stresses which are ~1.5MPa less than the analytical solution.

This error may be caused by the difference between the boundary conditions in the composite cylinder theory and the numerical simulation applied here. In the composite cylinder theory the applied pressure magnitude at both the outer and inner surfaces is assumed equal and the geometrical center of the cylinder system has no change due to stress balance. Thus, the deformation of the different cylinders in the composite cylinder theory is negligible and not considered to analyze the hoop and radial stresses. Instead of relating the displacements of the cylinders to the state of stress, pressure acting at both the inner and outer surfaces are adopted to obtain an analytical solution. However, the simulation using ABAQUS^{TM} requires the assignment of specific boundary conditions in the model. In this numerical model, the inner surface of casing cylinder is designed as a fixed surface in the vertical direction with no displacement. This is used to minimize the influence of the vertical load acting on the model. With all these specific boundary conditions, the numerical model generates stress results which are close to, but not exact matches, to the analytical solution with ~1.5 MPa difference.

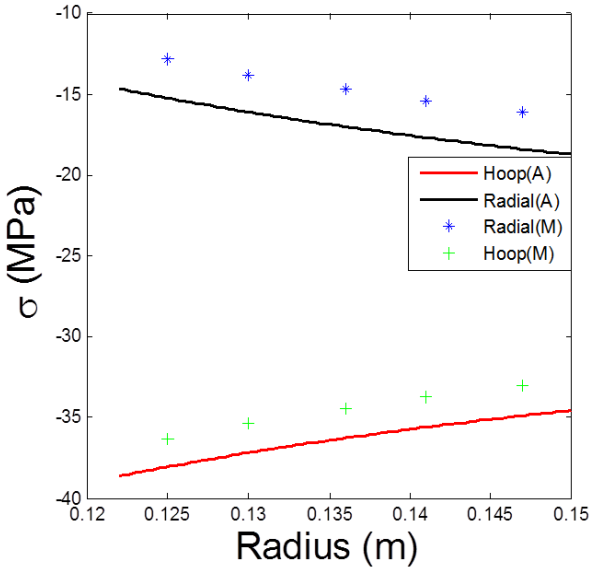

Figure 8.11. Results plot for the hoop and radial stresses comparing the values obtained from the analytical (A) solution to those obtained from a FEM (M) for the cement elements.

8.5. THERMAL STRESS MODEL VERIFICATION

A simple wellbore model has been created in order to verify the influence of a temperature change on the hoop stress in the wellbore. The model consists of a single sandstone material (Table 8.1) with a pre-existing cavity. Initial stress and temperature boundary conditions are assigned (Table 8.6) to the model in order to simulate the in-situ conditions which would exist in the anticline model (Appendix A). The model has been created such that it has a large enough horizontal extent to alleviate any influences from the boundary on the heat transfer.

Table 8.6. Stress and temperature values used in the model verification.

Parameter	Value
σ_1	27 MPa
σ_2	18.34 MPa
σ_3	11.97 MPa

Table 8.6. Stress and temperature values used in the model verification. (cont.)

T_i	50°C
T_f	20°C

The temperature change in the model is induced using the *SFILM keyword on a surface at the wellbore wall. The *SFILM keyword enables to study heat transfer whereby a reference temperature T_0 is emitted over a surface area (i.e. the borehole wall). The temperature which is applied to the wall is transferred via conduction to the formation over a given period of time. The time period used in this analysis was long enough such that the temperature just outside the wellbore wall is sufficiently close to the final temperature. The temperature which has been chosen as the film temperature is 20°C which is the reference temperature of liquid CO_2 at surface conditions.

As previously discussed, the hoop stress change caused by a temperature change (ΔT) may be significant enough to cause failure in a wellbore. If steady state conditions are assumed, the hoop stress change ($\sigma_{\theta\theta}^{\Delta T}$) caused by a temperature change can be as (Boresi and Schmidt 2002; Zoback 2007; Jaeger and Cook 2008):

$$\sigma_{\theta\theta}^{\Delta T} = \frac{\alpha_t E \Delta T}{1 - \nu} \tag{112}$$

Figures 8.12 shows the temperature distribution in the model at three time steps. The initial time step (Figure 8.12a) shows that the entire model is governed by a single temperature as given by the initial conditions (i.e. representing in-situ temperature conditions). Figure 8.12b shows the temperature distribution at an intermediate time step where the temperature has dropped rapidly at the wellbore wall caused by the application of a lower wellbore temperature using the *SFILM keyword. Figure 8.12c displays the temperature distribution at the ending time step. In Figures 8.12b and 8.12c it can be seen that the temperature change is occurring radially from the wellbore wall into the formation i.e. the heat transfer process represents pure conduction.

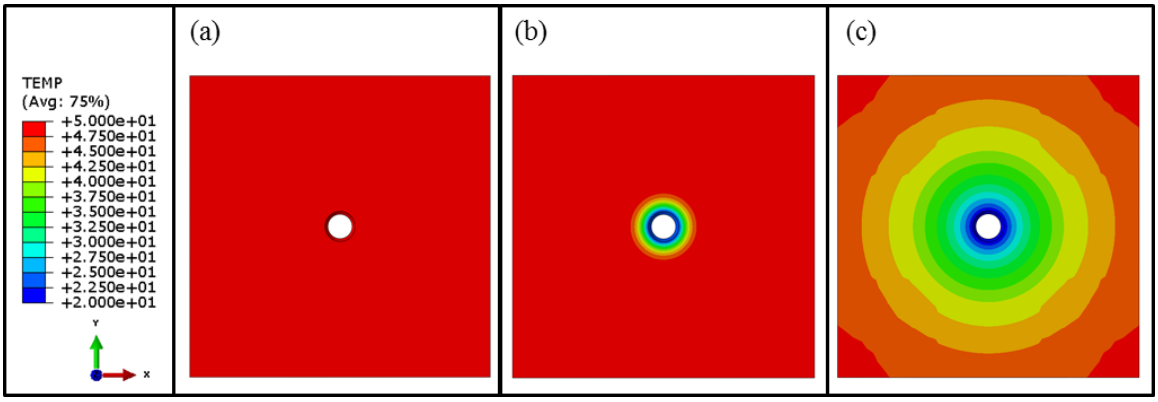

Figure 8.12. Top view of near wellbore region temperature distribution at early time (A), one-half the final time (B), and at the final time (C).

Figure 8.13 shows the hoop stress magnitude for the initial time step (Figure 8.13a) and for the final time step (Figure 8.13b). Figure 8.14 shows the radial stress magnitude for the initial time step (Figure 8.14a) and for the final time step (Figure 8.14b). As can be seen, the distribution of the hoop and radial stress does not change significantly in the far-field with the 30^{o} temperature drop. At the wellbore wall however significant changes in the state of stress occur. The hoop stress (i.e. S22) decreases from 39.2MPa to 33.1MPa. At $\theta=90^{o}$ the radial stress decreases from 1.29MPa to 0.8MPa.

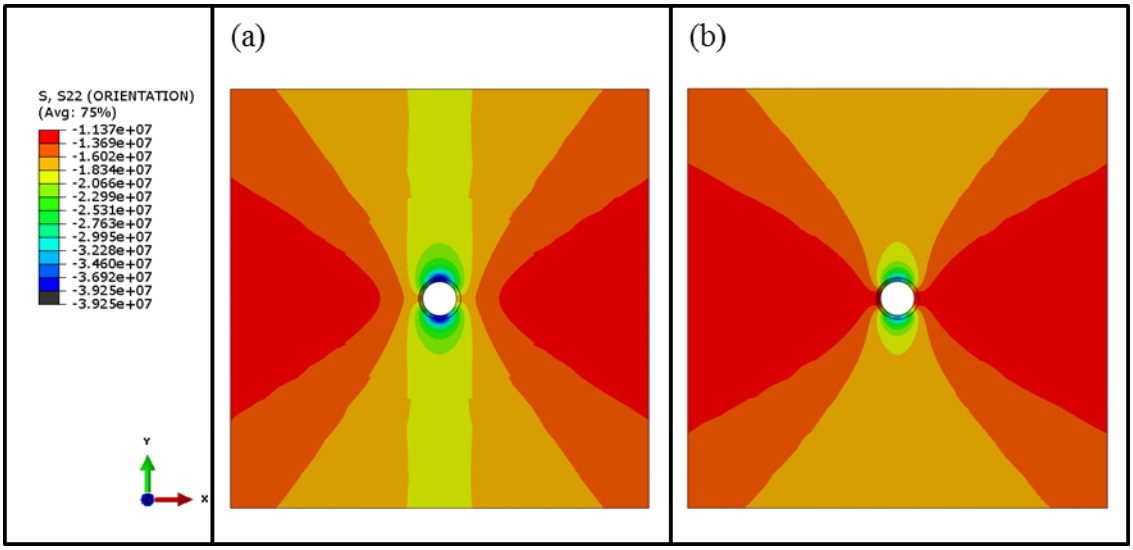

Figure 8.13. Hoop stress distribution for early time (a) before the temperature changes, and at late time after the temperature change has been induced (b).

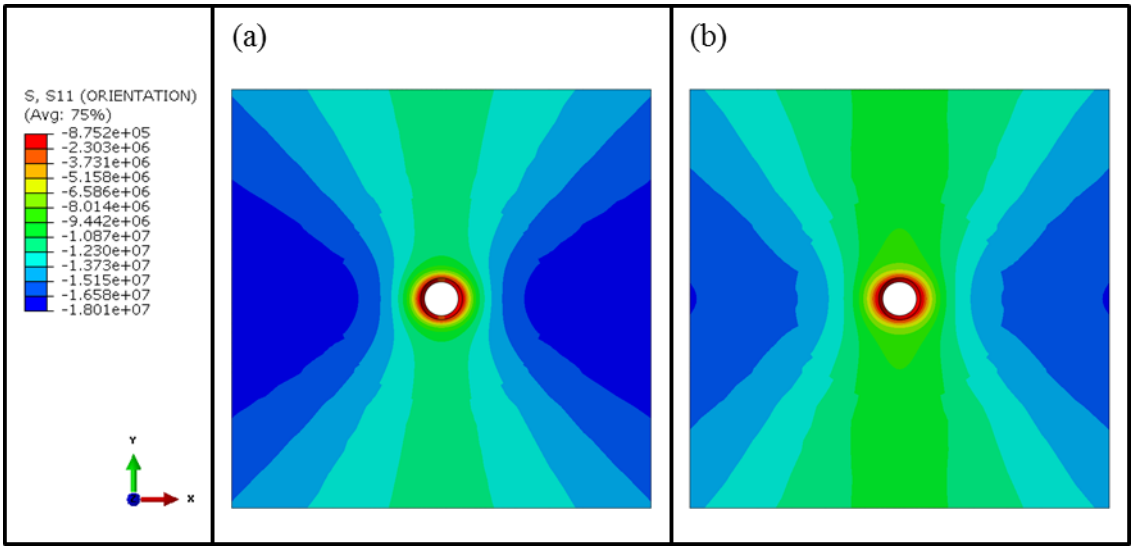

Figure 8.14. Radial stress distribution for early time (a) before the temperature changes, and at late time after the temperature change has been induced (b).

Temperature and hoop stress data are exported at two locations in the model in order to compare the modeling results to the analytical solution. One location is at the borehole wall, and the other at a distance of 2r of the borehole. Because only steady state temperature solutions are considered here the data is extracted once steady state

conditions are reached, i.e. the temperature at the point of reference remains constant for the remainder of the temperature flow step.

The data in Table 8.7 and Figure 8.15 show the results from the numerical model compared to the steady state analytical solution. The data displayed is the change in hoop stress which is caused by a temperature decrease of 30^o at the borehole wall. Figure 8.15 shows that for any time in the model in which steady state is not reached the error is significant. This explains the early time (before $\Delta T = 30^o$) error seen in Figure 8.15. However, if steady state conditions have been reached, the model results match well with the analytical solution. The analysis of steady state condition is considered sufficient as it results in the largest stress difference at a specific point of interest.

Table 8.7. Model data for temperature verification at a point X1 on the wellbore wall and point X2 at a distance of 2r away from the wellbore wall.

Thermal Stress Verification			
Solution Type	**Location**	**$\Delta\sigma_{\theta\theta}$ (MPa)**	**% Error**
Analytical	X1	0.03	0.5
Model	X2	0.94	3.8

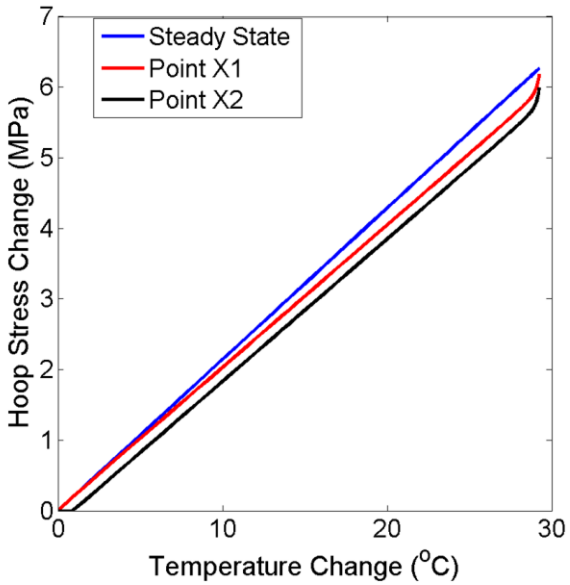

Figure 8.15. Comparison of the thermal stress analytical solution to the model results at locations X1 and X2. As the temperature at each point reaches the maximum temperature change value (30°C) the model results converge toward the analytical solution results. As the temperature change reaches its maximum at a point, that point is then at a constant temperature; steady state has been reached.

9. WELLBORE INTEGRITY RESULTS

In this group of simulations a series of FE models are established to investigate the influence of various Young's Modulus' evolutions (Tables 9.1 and 9.2) on the hoop stress in the cement sheath elements. For all models identical boundary conditions and material properties are used (Table 8.1). In the results analysis the evolution of the hoop stress for the cement sheath is studied in detail.

9.1. VARIABLE YOUNG'S MODULUS RESULTS

The influence of the magnitude of these Young's Modulus changes is tested in several wellbore scale FE models. 23 unique Young's Modulus evolution scenarios are used and the Young's Modulus values can be seen in Table 9.1 and Table 9.2. Where Table 9.1 are the scenarios which considers cement hardening only and Table 9.2 shows the scenarios for hardening and degrading Young's Moduli. For these cases E_o, E_i, and E_f are the initial, intermediate, and final Young's Moduli respectively. These scenarios are designed to test the influences of modeling the cement sheath if the overall increase in Young's modulus is greater than, less than, or equal to the subsequent decrease in Young's Modulus caused by cement degradation. Also compared in this analysis are scenarios in which the Young's Modulus is constant as is assumed in many cement sheath studies (Shahri et al., 2005; Gray et al., 2009; Haider et al., 2012; Shen and Beck 2012). In each of these scenarios linear increases/decreases of the Young's Modulus are assumed, and the intermediate value occurs at exactly half the total time of the simulation.

Table 9.1. Results of Scenarios 1-17 in which only hardening of the Young's Modulus occurs.

Model	E_o (GPa)	E_i (GPa)	E_f (GPa)	ΔE_1 (GPa)	$\sigma_{\theta\theta}^{max}$ (MPa)	σ_{rr}^{min} (MPa)
Scenario 1	5	20	20	15	53.1	5.54
Scenario 2	5	15	15	10	43.1	6.60
Scenario 3	5	25	25	20	66.3	4.08
Scenario 4	5	35	35	30	83.9	2.18
Scenario 5	10	20	20	10	28.0	5.79
Scenario 6	10	25	25	15	35.5	5.12
Scenario 7	10	30	30	20	41.2	4.24
Scenario 8	10	35	35	25	43.8	4.16
Scenario 9	15	20	20	5	19.6	5.88
Scenario 10	15	25	25	10	25.3	5.53
Scenario 11	15	30	30	15	29.1	5.11
Scenario 12	15	35	35	20	30.4	4.82
Scenario 13	20	30	30	10	23.2	5.39
Scenario 14	20	35	35	15	2.60	5.08
Scenario 15	20	20	20	0	14.2	5.75
Scenario 16	35	35	35	0	13.1	5.47
Scenario 17	10	10	10	0	15.2	6.49

Table 9.2. Results of Scenarios 18-46 in which both hardening and degradation of the Young's Modulus occurs.

Model	E_o (GPa)	E_i (GPa)	E_f (GPa)	ΔE_1 (GPa)	ΔE_2 (GPa)	$\sigma_{\theta\theta}^{max}$ (MPa)	σ_{rr}^{min} (MPa)
Scenario 18	5	15	10	10	5	30.5	7.73
Scenario 19	5	20	10	15	10	30.2	7.89
Scenario 20	5	20	15	15	5	42.6	6.86
Scenario 21	5	25	10	20	15	30.5	7.73
Scenario 22	5	25	15	20	10	43.1	6.60
Scenario 23	5	25	20	20	5	55.1	5.34
Scenario 24	5	35	10	30	25	30.2	7.89
Scenario 25	5	35	15	30	20	41.1	8.37
Scenario 26	5	35	20	30	15	55.1	5.34
Scenario 27	5	35	25	30	10	66.3	4.08
Scenario 28	5	35	30	30	5	72.0	2.84
Scenario 29	10	20	10	10	10	16.6	6.93
Scenario 30	10	20	15	10	5	23.1	6.51
Scenario 31	10	25	20	15	5	29.6	5.79
Scenario 32	10	35	20	25	15	29.6	5.79
Scenario 33	10	35	25	25	10	35.5	5.12
Scenario 34	10	35	30	25	5	41.1	4.54
Scenario 35	10	35	10	25	25	16.6	6.93
Scenario 36	10	35	15	25	20	23.1	6.51
Scenario 37	15	20	10	5	10	12.1	6.61
Scenario 38	15	20	15	5	5	16.6	6.93
Scenario 39	15	25	20	10	5	21.1	5.94
Scenario 40	15	35	10	20	25	12.1	6.61
Scenario 41	15	35	15	20	20	16.6	6.39
Scenario 42	15	35	30	20	5	29.1	5.11
Scenario 43	15	35	25	20	10	25.3	5.53
Scenario 44	15	35	20	20	15	21.1	5.94
Scenario 45	20	35	30	15	5	23.2	5.39
Scenario 46	20	35	25	15	10	20.1	5.71

The above models contains three material types; steel, cement, and formation rock. The values for the material properties are listed in Table 8.1. The cement elements which are of interest here do not contain pore pressure. It is commonly accepted that the pore pressure in the cement sheath will evolve over time to equal the pore pressure of the

surrounding formation (Bois et al., 2010). All reported hoop stress magnitudes are total stresses.

9.1.1. Cement Sheath Hardening. Figure 9.1 shows the results for 8 scenarios (1, 4, 5, 8, 9, 12, 15, and 16 in Table 9.1) in which the initial Young's modulus, E_0, has a lower value than the intermediate, E_i, and the final Young's modulus, E_f, and whereby E_i and E_f are equal. Figure 9.1 also includes two scenarios (15 and 16) in which the Young's modulus remains constant throughout the hardening stage. The results presented in Figure 9.1 show the hoop stress after cement hardening is achieved.

These scenarios are designed to investigate the influence of increasing Young's Modulus in the cement sheath and to compare it to a case whereby the Young's modulus remains constant; a common assumption in wellbore integrity studies (Shahri et al., 2005; Gray et al., 2009; Haider et al., 2012; Shen and Beck 2012). Figure 9.1a shows the hoop stress magnitudes (vs. radius) in the cement from scenarios in which various initial magnitudes of Young's Modulus increase to a value of 20GPa. Figure 9.1b shows the hoop stress magnitudes (vs. radius) in the cement from scenarios in which various initial magnitudes of Young's Modulus increase to a value of 35GPa. From Figure 9.1a it can be observed that the values of hoop stress throughout the cement are strongly influenced by the magnitude of increase in Young's Modulus. Larger increases of Young's Modulus lead to higher hoop stresses at the end of hardening. The same finding is also observed in Figure 9.1b. For Figure 9.1a, the lowest magnitude of hoop stress (e.g. 13MPa when R=0.147) is observed for the scenario featuring a constant Young's Modulus (e.g., scenario 15 with E=20GPa). For Figure 9.1b, the lowest magnitude of hoop stress (e.g. 12MPa when R=0.147) is observed for the scenario featuring a constant Young's Modulus (e.g., Scenario 16 with E=35 GPa). With the same final Young's Modulus (E_f), the reduction in the difference of intermediate (E_i) and final Young's Modulus (E_f) results in lower magnitudes of hoop stress throughout the cement sheath. For example, the hoop stress is 50 MPa at the center of the cement sheath in Scenario 1 (15GPa increase in Young's Modulus) and 19 MPa in scenario 9 (5GPa increase in Young's Modulus).

Another important observation is that the degree of decrease of hoop stress (resulting from a radius increase) is influenced by the Young's Modulus evolution. For

Scenario 1 (15GPa increase in Young's Modulus), the difference between the hoop stress at the inner and outer nodes of the cement sheath is 6 MPa; while for Scenario 9 (5GPa increase in Young's Modulus), the difference between the hoop stress at the inner and outer nodes of the cement sheath is 1MPa. The same observations can also be obtained from the scenarios in Figure 9.1b.

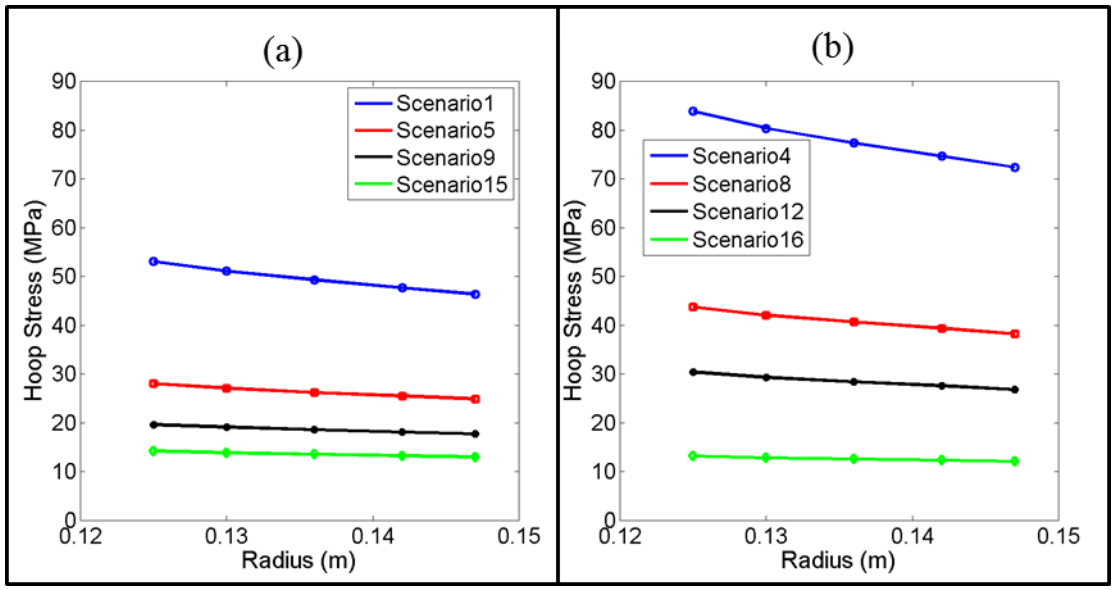

Figure 9.1. Results plot of the hoop stress vs. the radius for the cement elements in Scenarios 1, 5, 9, and 15 (a). Results plot of the hoop stress vs. radius for the cement elements in Scenarios 4, 8, 12, and 16 (b).

In order to investigate the relative impact of initial Young's modulus, E_0, and the change in Young's modulus during hardening, $\Delta E_1=E_i-E_0$, the results of the hardening models (Table 9.1) are re-plotted in Figure 9.2.

For all modeling scenarios it can be seen that, as the initial Young's Modulus is increased the final hoop stress obtained is decreased. This can be seen easily from the four models with a $\Delta E_1=E_i-E_0$ of 15GPa. The maximum hoop stress recorded is 53.1MPa (for E_0=5GPa). The minimum hoop stress recorded is 26.0MPa (for E_o=20GPa).

For each set of models which contain equal initial Young's Modulus values, it can be seen that as the value of ΔE_1 increases (as the cement hardens) the final hoop stress

also increases. For the models with E_o=5GPa the maximum and minimum hoop stresses are 83.9MPa and 43.1MPa, respectively. For the models with E_o=10GPa the maximum and minimum hoop stresses are 43.8MPa and 28.0MPa, respectively. For the models with E_o=15GPa the maximum and minimum hoop stresses are 30.4MPa and 19.6MPa, respectively. For the models with E_o=20GPa the maximum and minimum hoop stresses were 26.0MPa and 23.2MPa respectively.

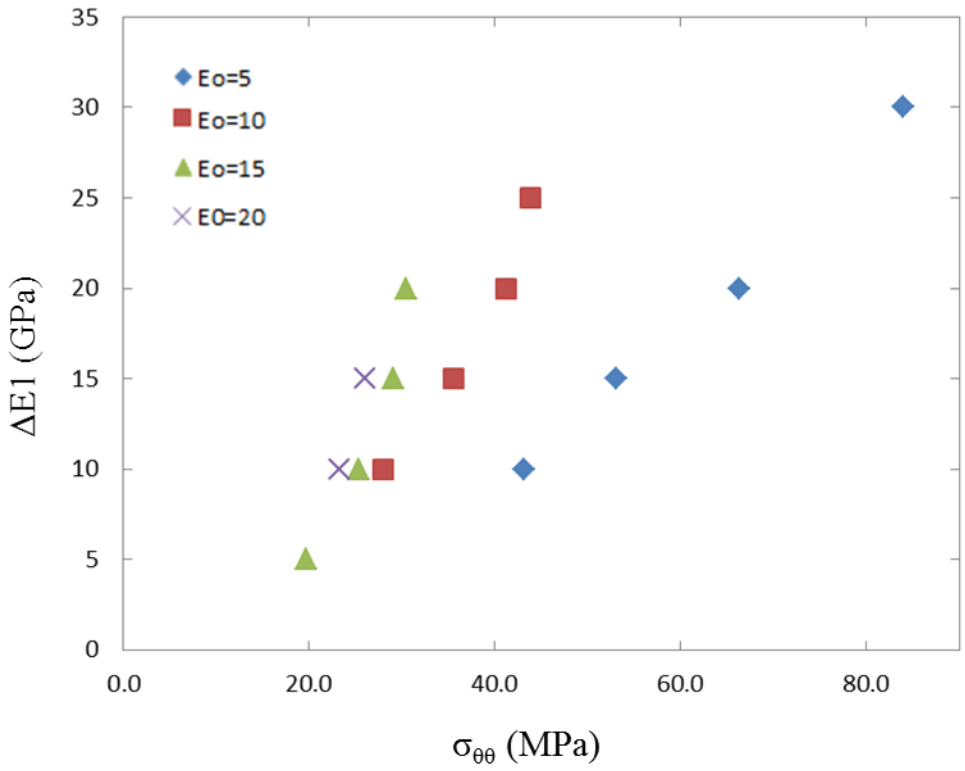

Figure 9.2. Hoop stress results for the hardening models scenarios.

9.1.2. Cement Sheath Hardening and Degrading. In order to study the hardening and degrading process of the cement sheath, the hoop stress of the cement sheath from scenarios containing both an increase and a decrease of Young's Modulus are plotted in Figure 9.3. Figure 9.3 shows the stress history of the hoop stress for an inner cement element in Scenario 24. This scenario includes both hardening and degradation of the Young's Modulus. An initial hoop stress at time t=0 of 20MPa is observed due to the initial conditions given from the staged FE analysis. An initial drop

of 1MPa is recorded as the model equilibrates. At t=1 the hardening of the Young's Modulus (from 5GPa to 35GPa) begins. From t=1 to t=3.5 an increase in the hoop stress is observed during the hardening stage. At t=3.5 the degradation process (from 35GPa to 10GPa) begins. From t=3.5 to t=6 a decrease in the hoop stress is observed during the degradation process.

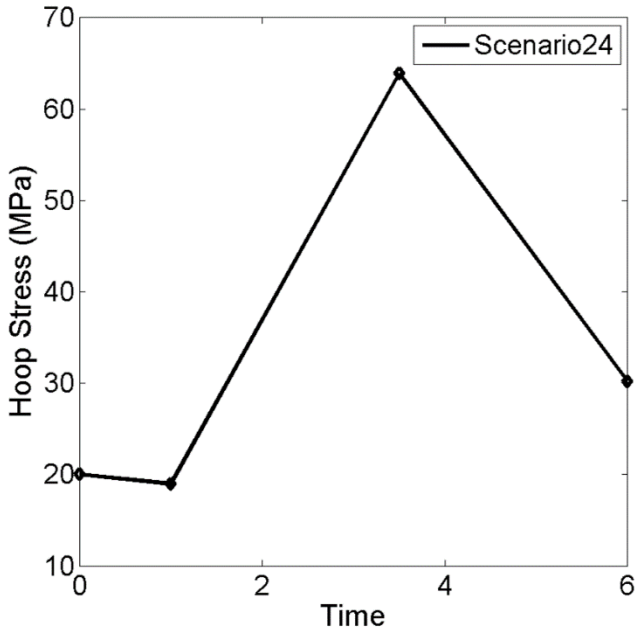

Figure 9.3. Hoop stress change vs. time for an element in the cement sheath for Scenario 24. In Scenario 24 both hardening and degradation occur.

The results of the various hardening and degrading scenarios are shown in Figure 9.4 (Scenarios 29 and 35 for Figure 9.4a and Scenarios 38 and 41 for Figure 9.4b). Figure 9.4 shows the hoop stress magnitudes throughout the cement sheath from scenarios in which $E_o = E_f$. For scenario 29 and 35, both E_o and E_f equal 10 GPa, and for Scenario 38 and 41 both E_o and E_f equal to 15 GPa. With different intermediate Young's Moduli (E_i), little difference in hoop stress magnitude in the cement sheath is observed.

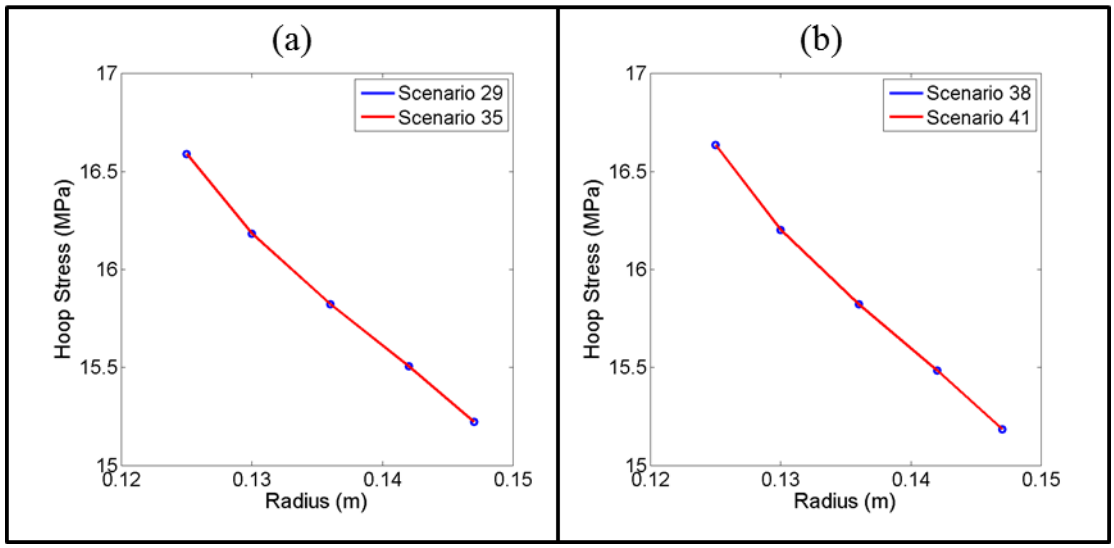

Figure 9.4. Results plot of the hoop stress vs. the radius for the cement elements in Scenarios 29 and 35 (a). Results plot of the hoop stress vs. the radius for the cement elements in Scenarios 38 and 41 (b).

Figure 9.5 shows how the magnitude of ΔE_1 and ΔE_2 influence the hoop stress in the cement sheath for models with E_o=5GPa. It can be seen that for a constant ΔE_2, large values of ΔE_1 result in larger final hoop stress. For example, for ΔE_2=5GPa the maximum hoop stress (72MPa) is obtained in models with ΔE_1=30GPa, while the minimum hoop stress (30.5MPa) is found in models with ΔE_1=10GPa.

Also observed in Figure 9.5 is that as the magnitude of ΔE_2 decreases, the final hoop stress decreases for models with the same ΔE_1 values. For example, models with ΔE_1=30MPa result in hoop stress values ranging from 30.2MPa when ΔE_2=25GPa to 72MPa when ΔE_2=5MPa. Similar results can be seen in Figures 9.6, 9.7, and 9.8 which report ΔE_2 versus hoop stress for the scenarios with E_o values of 10GPa, 15GPa, and 20GPa respectively. If Figures 9.5, 9.6, 9.7, and 9.8 are viewed as a whole, another observation can be made. For constant values of ΔE_1 and ΔE_2 (e.g. ΔE_1=10GPa and ΔE_2=5GPa) as the E_o value decreases the final hoop stress increases. For this example the greatest hoop stress is 30.5MPa and is for E_o=5GPa, and the smallest hoop stress is 16.6MPa and corresponds to E_o=15GPa.

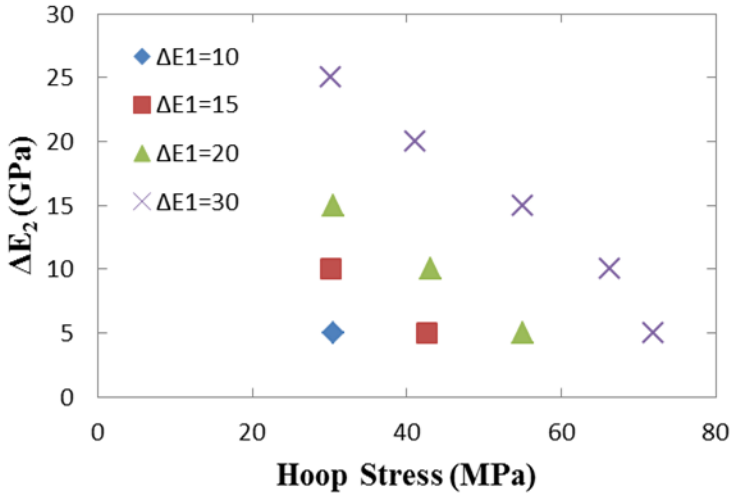

Figure 9.5. Plot of ΔE_2 versus hoop stress for scenarios where E_o=5GPa.

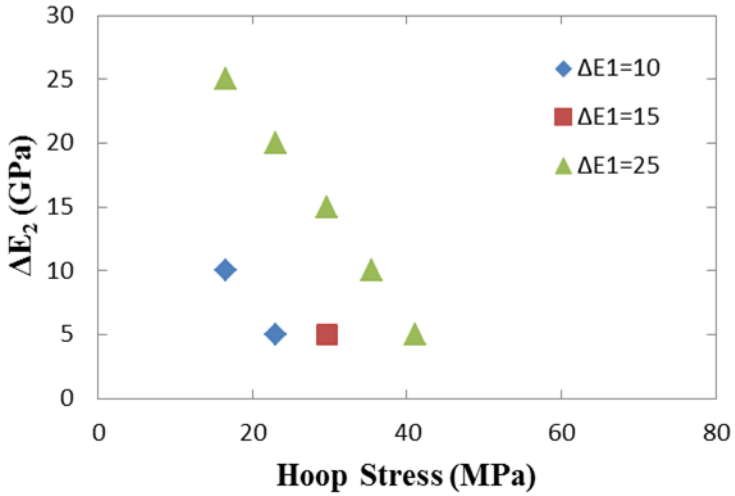

Figure 9.6. Plot of ΔE_2 versus hoop stress for scenarios where E_o=10GPa.

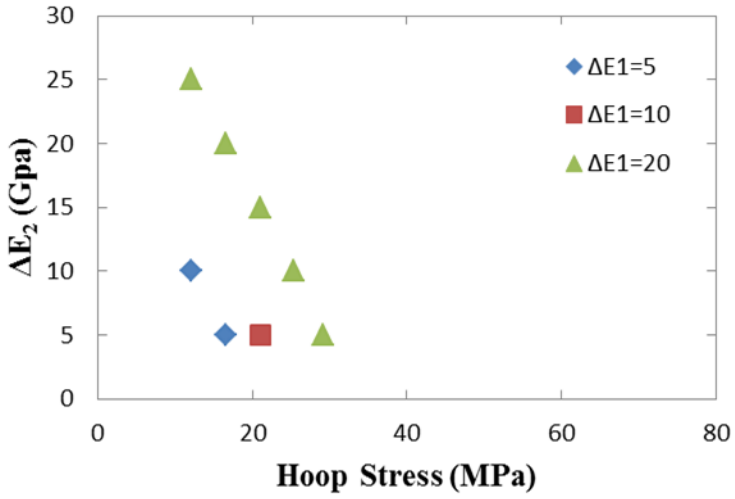

Figure 9.7. Plot of ΔE_2 versus hoop stress for scenarios where E_o=15GPa.

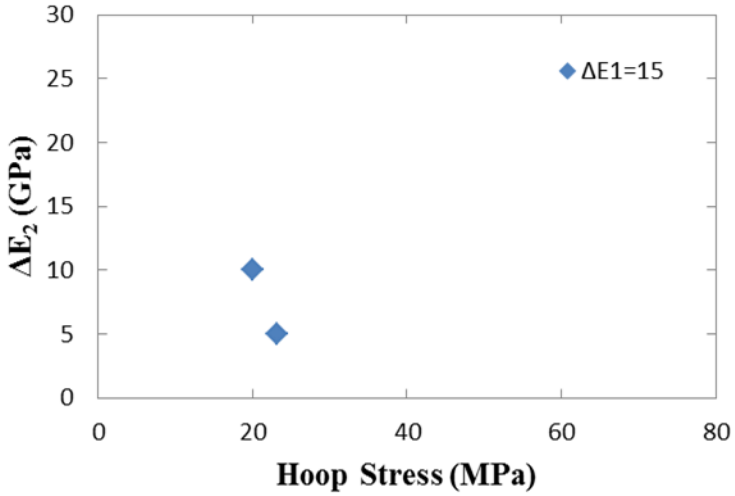

Figure 9.8. Plot of ΔE_2 versus hoop stress for scenarios where E_o=20GPa.

Figure 9.9 shows the hoop stress magnitudes throughout the cement sheath from scenarios with equal E_f (10 GPa). For Scenarios 19 and 24 the same initial and final Young's Moduli are applied to the cement material; little difference of hoop stress magnitude at the same radius is observed. The same observation is found between Scenarios 37 and 40, when the same initial and final Young's Moduli are applied to the cement material. However, significant difference of hoop stress is shown between

scenarios with the same initial Young's Moduli only. For example, the hoop stress at the inner cement sheath is 30MPa for scenario 19, and 12MPa for scenario 37 when Scenarios 19 and 37 share the same E_i (20GPa) and E_f (10 GPa). The obvious difference in hoop stress resulting from the different E_o is also observed in Scenarios 24 and 40 with the same E_i (35GPa) and E_f (10 GPa).

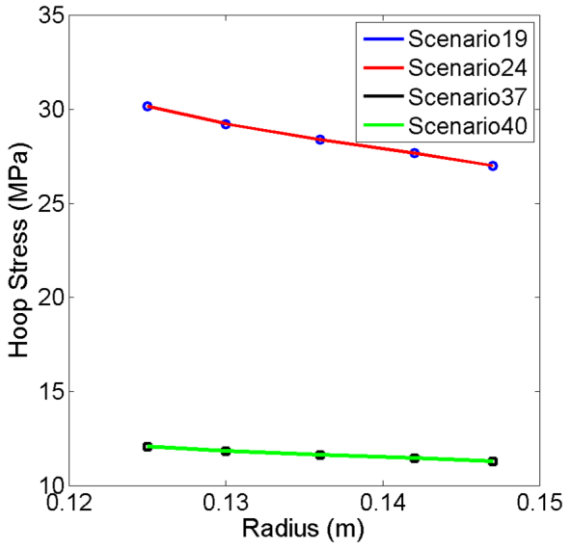

Figure 9.9. Results plot of the hoop stress vs. the radius for the cement elements in Scenarios 19, 24, 37, and 40.

Hoop stress magnitudes throughout the cement sheath from scenarios with equal E_i (20 GPa) and E_f (15 GPa) are shown in Figure 9.10. In these scenarios the initial Young's Modulus changes from 5 GPa to 20 GPa. Figure 9.10 shows the significant influence of the initial value of Young's Modulus on the hoop stress magnitudes. At the inner nodes of the cement sheath, the maximum magnitude of the hoop stresses is generated. The maximum hoop stress (43 MPa) for Figure 9.10 is generated in scenario 20 which has the lowest initial Young's Modulus (E_o=5 GPa), and the minimum magnitude of hoop stress (10 MPa) is generated in scenario 38 which has the highest initial Young's Modulus (E_o=20 GPa).

Another important observation is that the degree of decrease of Hoop stress (resulting from a radius increase) is influenced by the Young's Modulus evolution. For Scenario 20 (15GPa increase before degrading), the difference of hoop stress between the inner and outer nodes of the cement sheath is as large as 6 MPa. For scenario 38 (no increase in Young's Modulus before degrading), the difference of hoop stress between the inner and outer nodes of the cement sheath is 1MPa.

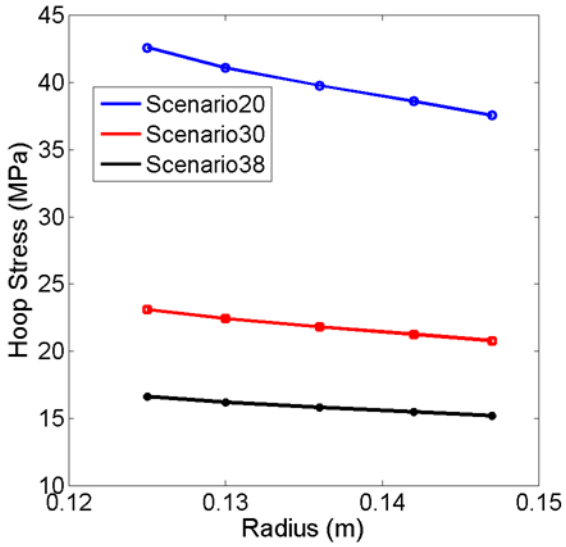

Figure 9.10. Results plot of the hoop stress vs. the radius for the cement elements in Scenarios 20, 30 and 38.

10. WELLBORE INTEGRITY DISCUSSION AND CONCLUSIONS

The 3D numerical modeling approach presented here is used to provide a more accurate representation of the near wellbore cement sheath stresses by applying a staged FE approach and inclusion of the Young's Modulus evolution of the cement. Generally, FE models of the near wellbore region consist of a single step. These single step models do not include the stress history which would arise from the actual drilling and completing processes. By using a staged FE model, the entire process, from in situ stress state to completion, is included and their influence on every following step is thus considered. With the SoS from the staged FE model obtained, further analyses can be performed.

This study applies the staged FE approach to a model testing the influences of Young's Modulus evolution on the cement sheath stresses. Many wellbore integrity studies investigating cement sheath integrity assume a final Young's modulus after the cement is hardened can be used (Shahri et al., 2005; Gray et al., 2009; Haider et al., 2012; Shen and Beck 2012). This implies that the evolution of the Young's modulus during cement hardening and degrading, as observed by other studies (Mueller and Eid 2006; Bois et al., 2010), is neglected and the state of stress is independent on the cement evolution. The numerical modeling results presented in this thesis show that by including the Young's Modulus evolution the cement sheath stresses are in fact much different than in models where single values for cement Young's Modulus is assumed. In comparison, the radial stress in the cement sheath shows changes which are small compared to the changes in hoop stress.

The hoop stress values obtained in this thesis are unrealistic due to pre-straining of the cement elements. In a real situation the cement would be stressed with a magnitude equal to the hydrostatic pressure of the cement slurry. However, the scenarios in which high hoop stress values are reported in this thesis will produce high hoop stresses in a wellbore situation in which post-curing strains are introduced into the wellbore system. These strains could be caused by a multitude of drilling and production processes.

10.1. HARDENING

The following observations can be summarized after the Young's modulus variation during cement hardening:

- Not considering any variation of E (i.e. assuming a constant final E) results in the lowest hoop stress magnitudes compared to cases where E is increasing.
- The lower the initial Young's modulus E_0, and for a constant increase during hardening (ΔE_1=constant), the higher the resulting hoop stress.
- The larger ΔE_1, the larger the resulting hoop stress.

This shows that in order to asses cement sheath integrity both the initial Young's modulus and the increase in Young's modulus during hardening significantly affects the resulting hoop stress. In order to display the consequences for cement sheath failure a Mohr-Coulomb failure criterion with S_0=10MPa, φ=30^o, and T_0=5MPa is applied to scenarios 4 (i.e. considering hardening; Figure 10.1b) and 16 (i.e. assuming a constant E; Figure 10.1a) and the distribution of plastic strain is shown in Figure 10.1.

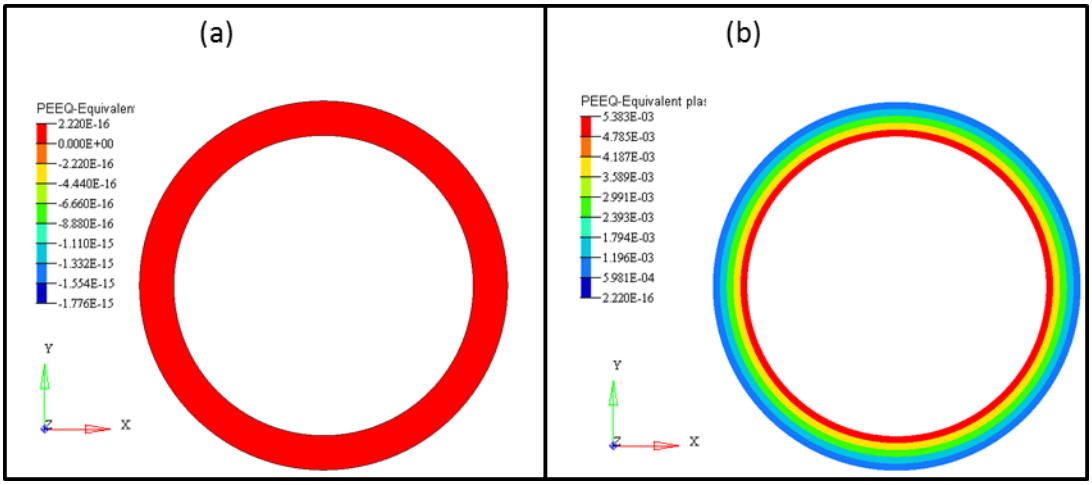

Figure 10.1. Plastic strain distribution due to shear failure for the cement sheath of Scenario 16 (a) and Scenario 4 (b).

The results show that 0 plastic strain (and therefore no failure) occurs in the cement sheath for Scenario 16 (Figure 10.1a), while Scenario 4 develops plastic strain with a maximum value of 5.4x10^-3 at the inner elements, decreasing radially outward. This implies that for models with a single Young's Modulus a smaller, more stable, Mohr-Circle will be obtained. Models with variable Young's Modulus may be at further risk for shear failure by increasing the size the Mohr Circle with increases in the hardening amount (Figure 10.2). Figure 10.2 shows an accurate representation of the cement state of stress using Mohr's circles for Scenarios 4 and 16. It can be seen that as the change in Young's Modulus increases, the state of stress in the cement elements becomes more likely to fail in shear. For Scenario 4 the increase was so great that the state of stress causes shear failure in the cement while Scenario 16, with a constant E_0 value which is equal to the E_f value of Scenario 4, would be safe from shear failure. If shear failure occurs, debonding of the cement from the casing is likely (Celia, 2004). This debonding would then open a fluid pathway between the cement and casing in which liquids or gases may travel (Figure 6.1).

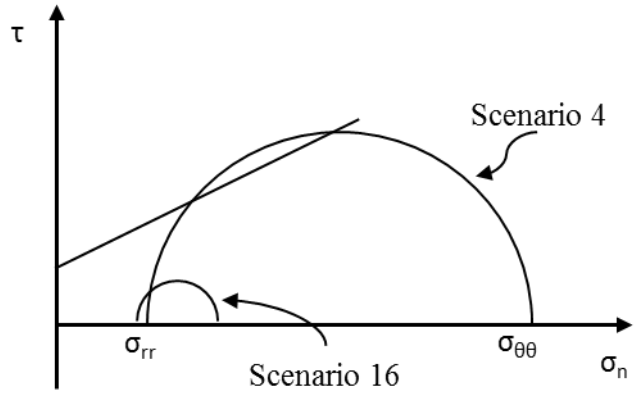

Figure 10.2. Mohr-Circles for Scenarios 4 and 16 showing failure of Scenario 4 in shear based on a Mohr-Coulomb failure envelope.

The hardening scenarios herein are conducted using a linear increase in the magnitude of the Young's Modulus. A more realistic non-linear version of Scenario 8

was created in order to test the influence of non-linearity during hardening of the Young's Modulus on the final hoop stress in the cement sheath. Figure 10.3 shows the hardening curve which are used in both the linear and non-linear versions of Scenario 8. The non-linear hardening curve was created by curve fitting the Young's Modulus for scenario 8 (from 10GPa to 35GPa) with lab data from experiments conducted by Mueller and Eid (2006) on cement sheath properties during cement curing. The hardening relationship is given by:

$$E = -25.028t^2 + 52.19t + 8.058 \tag{113}$$

where E is the Young's Modulus in GPa and t is time.

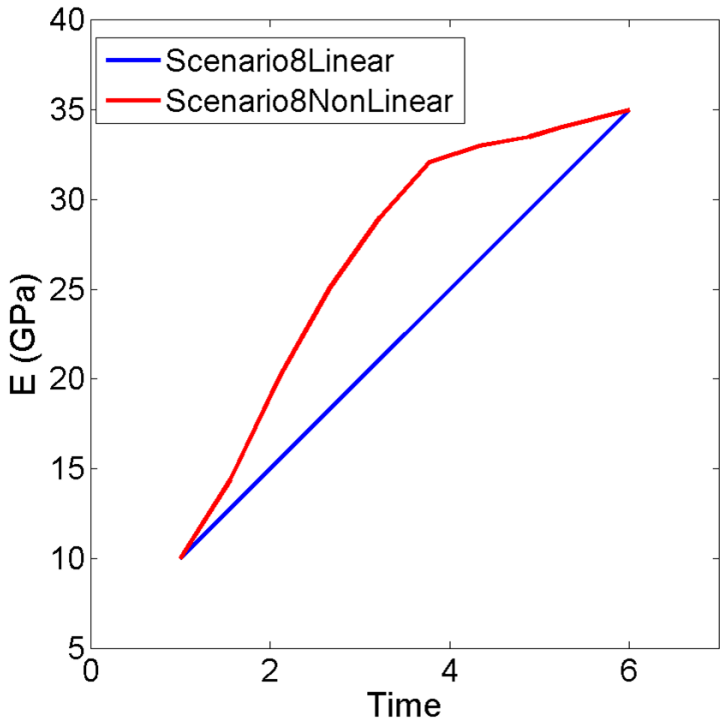

Figure 10.3. Linear and non-linear Young's Modulus hardening curves used in Scenario 8.

Figure 10.4 contains the hoop stress results from the models in which the hardening curves shown in Figure 10.3 are used. It can be seen that the hoop stress evolution corresponds strongly with the Young's Modulus curve.

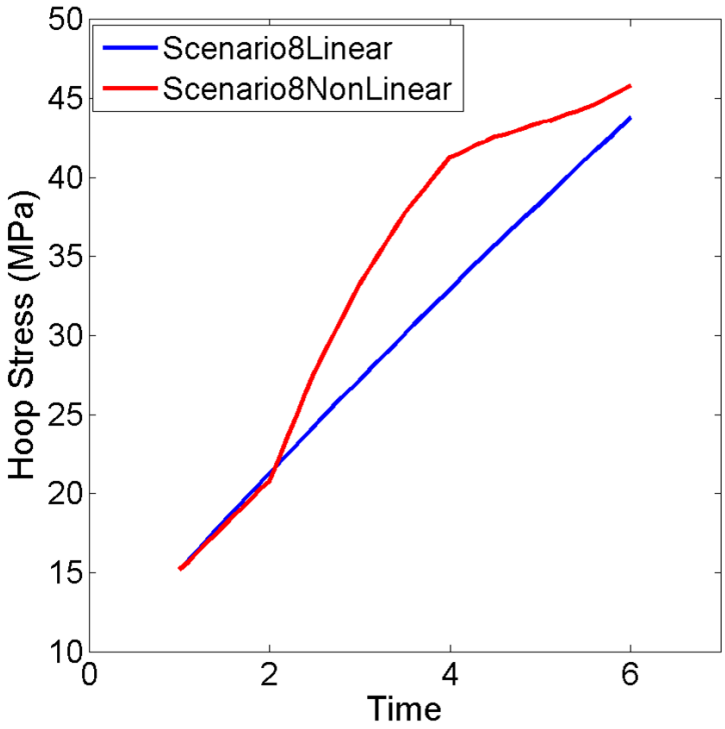

Figure 10.4. Hoop stress path during hardening for both a linear and non-linear Young's Modulus hardening curve for Scenario 8.

Figure 10.4 shows that not only is the final value of Young's Modulus important, but the hardening curve itself has significant influence on the stress at any given time (e.g. at time=4 the linear E reports values of 33MPa while the non-linear reports 40MPa). If the rock strength properties were such that failure were to occur at hoop stress values of 40MPa, the failure would occur at much earlier times in models with more realistic hardening curves than the linear curves used here. Also seen in Figure 10.4 is that the final value of hoop stress has been affected by the non-linear hardening curve. For the

linear hardening curve the final hoop stress is 43.8MPa, while the non-linear curve shows a maximum hoop stress of 45.8MPa.

10.2. HARDENING AND DEGRADING

The following observations can be summarized after the Young's modulus variation during cement hardening and degrading:

- If the initial Young's modulus and the final Young's modulus are equal, the respective change in Young's modulus (i.e. the magnitude of E_i) does not have a significant contribution on the resulting hoop stress.
- For a constant decrease ΔE_2, a larger initial increase ΔE_1 results in higher hoop stress.
- For a constant increase ΔE_1, for lower ΔE_2 the hoop stress magnitude decreases.
- For $\Delta E_1 > \Delta E_2$: for lower initial Young's modulus, E_o, the hoop stress decreases.
- The higher E_o, the lower the resulting hoop stress.
- For cases with $E_o = E_f$: the largest hoop stress results for the lowest E_0.

This shows that in order to asses cement sheath integrity both the initial Young's modulus and the increase and decrease in Young's modulus during hardening and degrading significantly affect the resulting hoop stress. The results presented show that (for both hardening and hardening and degrading cement) in order to assess cement sheath failure, robust laboratory testing is crucial to calibrate the presented numerical modeling study.

The scenarios presented in this study have shown that for linear increases and decreases of Young's Modulus if $E_i = E_f$, little effect will be seen in the resulting hoop stress. While the maximum hoop stress has been shown to vary when non-linear increases in E are used for hardening, this non-linear increase does not influence the final hoop stress reported when $E_i = E_f$. This is tested using the Young's Modulus values from Scenario 35. Figure 10.5 shows the Young's Modulus evolution for Scenario 35 when a

linear increase and linear decrease is used, and the evolution when a non-linear increase and a linear decrease are given.

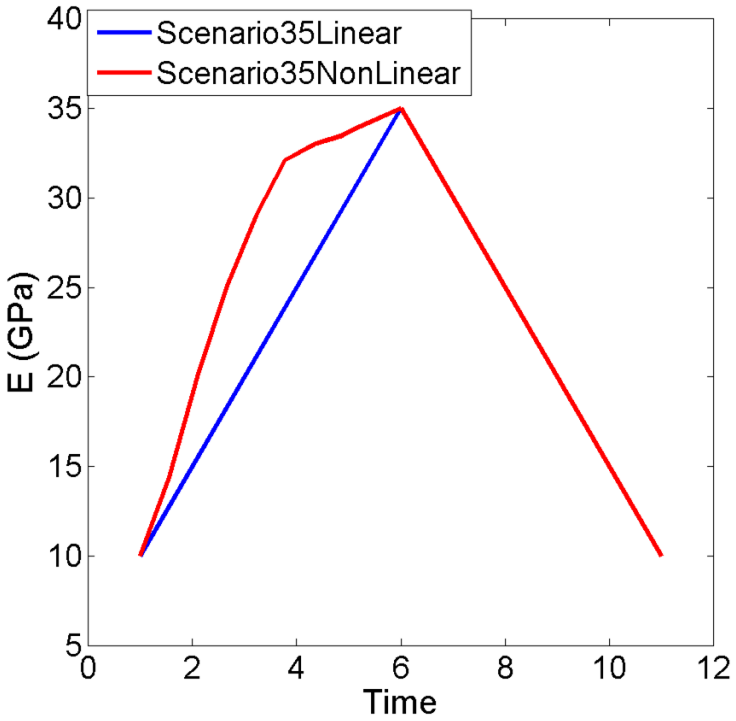

Figure 10.5. Linear and non-linear hardening and degradation curves for Scenario 35.

The results of the models which followed the Young's Modulus curves given in Figure 10.5 are shown in Figure 10.6. The figure shows that even though a non-linear hardening curve was used, the final hoop stress after degradation has occurred is the same as the final hoop stress obtained from scenario 35 in which both hardening and degrading occurred in a linear fashion. However, by inspection of Figure 10.6 at Time = 8 it can be seen that the hoop stress in each model would not be the same. This leads to the conclusion that the hoop stress generation for any model with the same boundary conditions may be highly time dependent, and that if any Young's Modulus values are equal the stresses may eventually converge on identical values.

In order to predict failure of the cement sheath accurate knowledge of cement integrity over time is needed. Depending on the environment in which the cement is subjected to, the integrity may be compromised. In the case of abandoned oil wells the flow of hydrocarbons in the near wellbore region can have detrimental effects on cement integrity, both mechanically and chemically (Celia 2004).

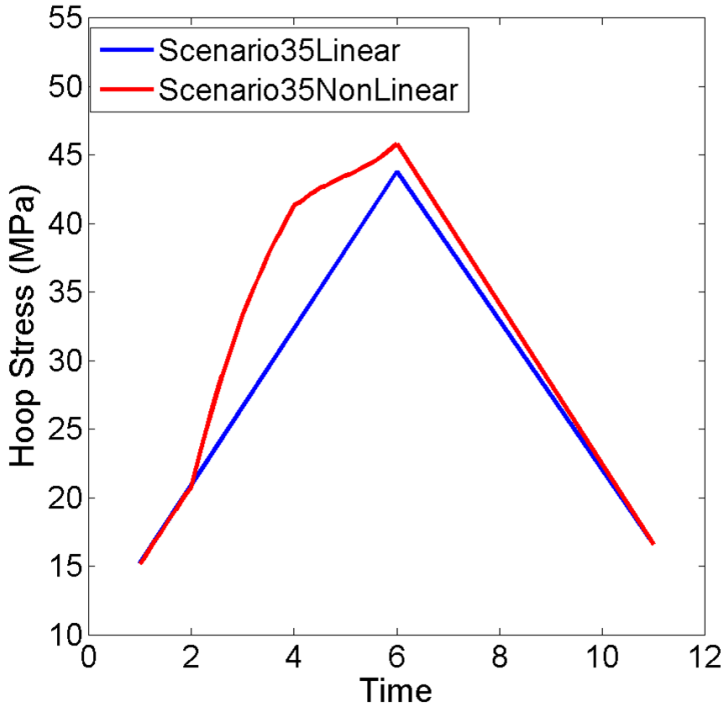

Figure 10.6. Hoop stress evolution for Scenario 35 in which both linear and non-linear hardening curves, and linear degradation curves are implemented.

10.3. TEMPERATURE LOADING

In order to test the cement integrity in a scenario of cold CO2 injection the modeled wellbore system for Scenario 40 (Table 9.2), containing a Mohr-Coulomb failure criterion and a Rankine tension cutoff (S_0=10MPa, φ=30^o, and T_0=5MPa), is subjected to pore pressure and temperature loads. The model is given a final pore pressure value of 14.46MPa which is constant throughout the simulation. A temperature decrease of up to ΔT=30^{o}C is then applied to the model as described in section 8.5.

Figure 10.7 shows the hoop stress and plastic strain for an element in the cement sheath in the aforementioned model.

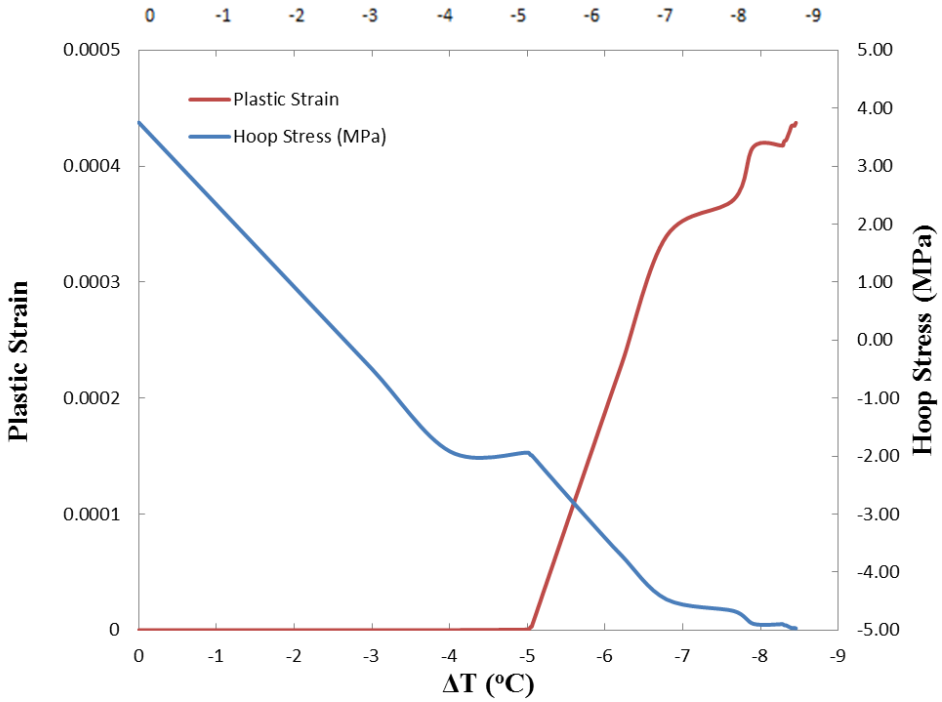

Figure 10.7. Hoop stress and plastic strain vs. ΔT for Scenario 40 in which pore pressure and a temperature decrease are implemented.

Figure 10.7 shows that as the temperature decreases the hoop stress also decreases (towards tensile failure). Small reductions in radial stress also occur (<1MPa). After a temperature decrease of 5^{o}C the hoop stress becomes tensile and tensile failure of the cement sheath begins to occur as the plastic strain is increasing. Any further decrease in hoop stress causes additional plastic strain to develop. This plastic strain would then correspond to increased amounts of tensile failure and fractures in the cement sheath. This could potentially lead to leaks in the cement sheath and contamination of the surrounding formations. While the example given in Figure 10.7 is modeled using Scenario 40 (where E_f=10GPa) it should be noted that if a larger E_f value is present a larger hoop stress change will occur following equation 112. This would lead to an increasingly greater chance for tensile failure. This again shows the importance of

accurate laboratory testing for both hardening and degradation curves which would be unique for each cement sheath based on their in situ conditions.

10.4. LIMITATIONS

The work presented on the cement sheath integrity has three main limitations. The first and most significant limitation is the lack of cement shrinkage. The models presented here contain three concentric cylinders (casing, cement, and formation) which are assumed to be perfectly bonded to each other; this allows for the use of the thick-walled cylinder assumption. This condition implies that at each boundary of two materials, each material undergoes the same magnitude of displacement. In a real world scenario, this would not occur. Each of the three materials should undergo their own displacements, especially in the case of cement which is inserted into the annular space as a fluid slurry and not as a competent material as is modeled here.

ABAQUS^{TM} is able to implement contact surfaces which could be used in order to allow separation between materials to occur. If contact surfaces are used, the user would obtain the ability to allow the cement elements to de-bond from either the casing or the formation rather than assuming the cement follows the displacements of the casing and formation. This approach was not followed in this thesis as the study of the Young's modulus during the hardening and degrading stages could be compared to the thick-walled cylinder theory. Since laboratory testing was not performed the comparison of the numerical modeling results to the thick-walled cylinder solution represented the only means to model validation.

The second limitation is that the hardening and degrading process occur through a change in a single elastic parameter. The actual hardening and degrading processes which occur influence the cement paste at a molecular level by either creating or destroying bonds between elements. The assumption that these processes can be accurately portrayed by changing a single property is limited. At a minimum the process should be modeled as a porous-elastic material in order to couple the change in porosity which occurs in the hardening and degrading processes to the change in elastic parameters.

The third limitation is the lack of accurate, laboratory obtained data. This thesis assumes all values of Young's Modulus without any on site laboratory testing. The values

were obtained from the literature, and are believed to be within acceptable ranges. However, it is unknown whether this assumption holds true for cement which hardens at the specific pressures and temperatures which is encountered at reservoir depth. Another aspect which is overlooked is total time which would need to pass before the level of degradation which is used in this study occurs. The time for degradation of cement is highly dependent upon cement type, additives, and the subsurface conditions. For this to be accurately implemented into the FE models, substantial lab work and knowledge of the materials used would be required.

10.5. FUTURE WORK

The work presented in this thesis is part of an ongoing project to study the state of stress in the near wellbore region during drilling and completions. The stage of the project presented here is the design and staged modeling approach verification for a model with perfect bonds at the cement interfaces. In the future the model will be enhanced to include the concepts of cement shrinkage induced by the associated temperature change by use of contact surfaces. Also included in future studies will be the porous-elastic constitutive relationships and integrated plasticity and hardening models. These concepts will allow for more in depth failure analysis to be performed.

A more robust study including integration of pore pressure, temperature, and plasticity modeling will also be included in future studies. Pore pressure evolution plays an important role for all subsurface studies, especially if areas of overpressure are encountered. The role of temperature on the stress evolution of the cement sheath will also be studied in greater detail. In future studies a constant temperature change will not be used, but a temperature cycle (Cooke et al., 1983; Shahri et al., 2005) will be implemented. This cycle is caused from the non-constant pumping of fluids though the wellbore. In many situations the material pumped down hole is not in a constant supply, and thus must be pumped in stages.

APPENDIX A

ANTICLINE MODEL GEOMETRY AND SETUP

In this thesis generic anticline model geometry previously used in Paradeis et al. (2012) and Amirlatifi et al. (2012) is used as a base case for the wellbore trajectory optimization. The modeling approach is based on the assumptions that the anticline structure is pre-existing and that static displacement boundary conditions can be used to simulate all three Andersonian stress regimes. These models do not include any information which could be gained by including the development of the structure through geologic time. The use of static displacement boundary conditions is a common approach in simulating the in-situ stress state for many geomechanical studies.

The geometry for the generic anticline structures used in this study is shown in Figure A1a. The models are 6000m (x-direction) by 1500m (y-direction) by 2500m (vertical direction). In order to minimize the boundary effects of the numerical model, the anticline is positioned in the center of the model with 1500m of horizontally layered material on both sides of the anticline. The models comprise rock layers of four different materials: a sandstone and shale sequence (Figure A1b) in the middle of the model is covered by an overburden layer and bounded on the bottom by a basement layer. The total thickness of the shale and sandstone sequence is 500m. The top shale, top sandstone, and caprock are each 100m for all model stress regimes tested. The interface between each layer is modeled as a frictional contact surface enabling in-plane displacements.

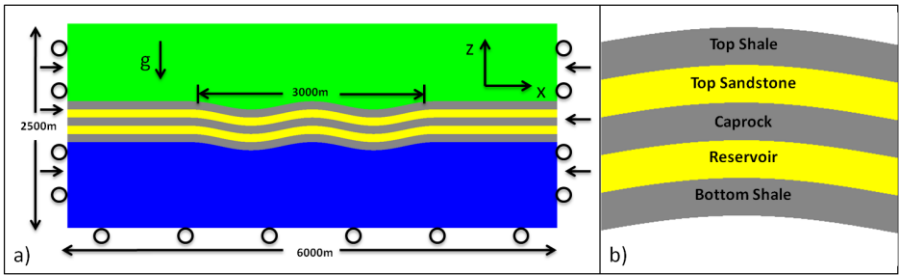

Figure A1. Model geometry for the anticline model.

The finite element analyses are run in two consecutives steps. The first step serves to equilibrate the gravitational body force over the complete model domain. In the second step displacement boundary conditions are used to generate the strains simulating the

different stress regimes in 3D. The corresponding equations of linear poro-elasticity were used to calculate the displacements (Jaeger et al., 2007). For the extensional stress regime, it is assumed that the sedimentary layers are tectonically relieved and thus the uni-axial strain assumption to calculate the resulting horizontal stresses applies (Engelder, 1993).

$$\sigma_h = \frac{\nu}{1-\nu}\sigma_V + \frac{(1-2\nu)}{(1-\nu)}\alpha P \quad (2)$$

For strike-slip and compressional regimes, the three-dimensional boundary conditions are calculated using the relative stress ratios. For both of these regimes, the vertical stress is given by the integration of overburden density. In a strike-slip regime, the minimum principal stress is the minimum horizontal stress which is given by $\sigma_h = 0.8 * \sigma_v$, the vertical stress is the intermediate principal stress and the maximum principal stress is $\sigma_H = 1.2\sigma_v$. For the compressional regime, the vertical stress is the minimum principal stress, the intermediate stress is $\sigma_h = 1.25\sigma_v$ and the maximum principal stress is$\sigma_H = 1.5\sigma_v$.

One of the major advantages to using finite element codes is the ability to apply unique material properties onto specific sets of elements in a model. In both of the models used in this study multiple materials are present, and each material has its own unique set of properties. Table x.x lists the complete set of properties for each of the materials used. The properties are chosen based on typically accepted values.

Table A1. Material Properties for the anticline model.

Material Properties			
Property	Units	Sandstone	Shale
Density (ρ)	kg/m^3	2300	2130
Young's Modulus (E)	GPa	15	15
Poisson's Ratio (ν)	unitless	0.3	0.25
Hydraulic Conductivity	m/s	1.00E-06	1.00E-07

Table A1. Material Properties for the anticline model.

Thermal Expansion	$1/^{o}C$	1.00E-06	X
Specific Heat	$J/(kg^{o}C)$	1380	X
Thermal Conductivity	$J/(ms^{o}C)$	0.29	X

APPENDIX B

ANTICLINE MODEL EXTENSIONAL STRESS REGIME OPERATIONAL WINDOWS

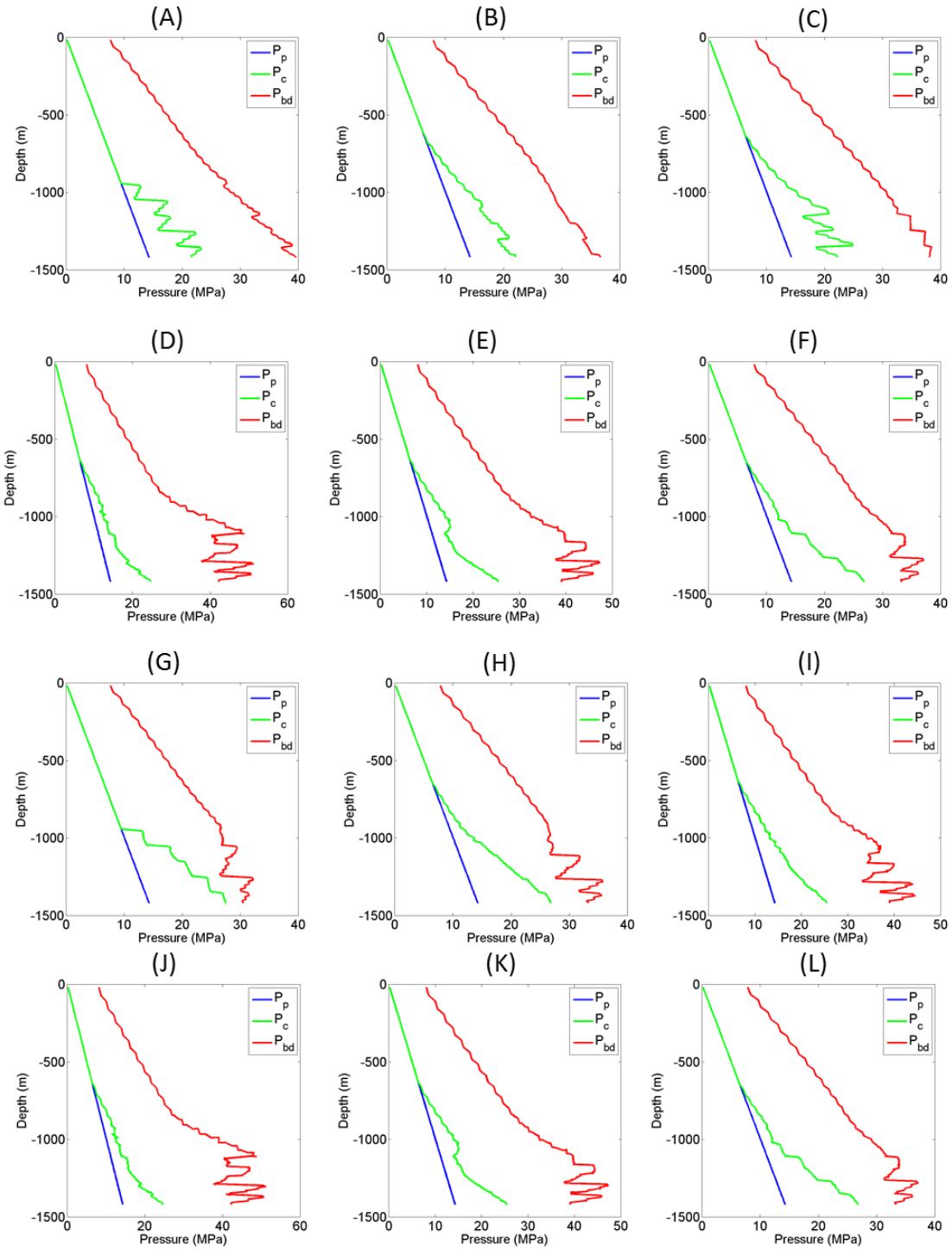
(A)
(B)
(C)
(D)
(E)
(F)
(G)
(H)
(I)
(J)
(K)
(L)
Depth (m)
Pressure (MPa)
P_p
P_c
P_bd

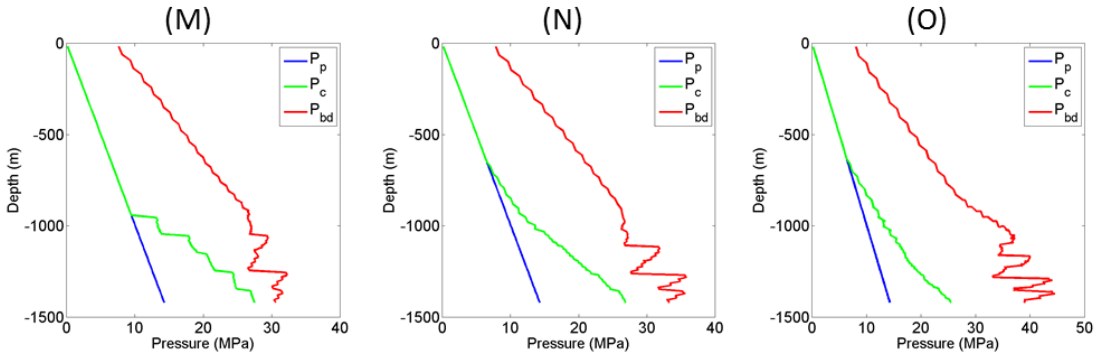

Where Figures A, B, and C are the pressure windows for the crest, limb, and valley respectively, and D, E, F, G, H, I, J, K, L, M, N, and O are the pressure windows for wells with azimuths of 0 , 30, 60, 90, 120, 150, 180, 210, 240, 270, 300, and 330 degrees respectively.

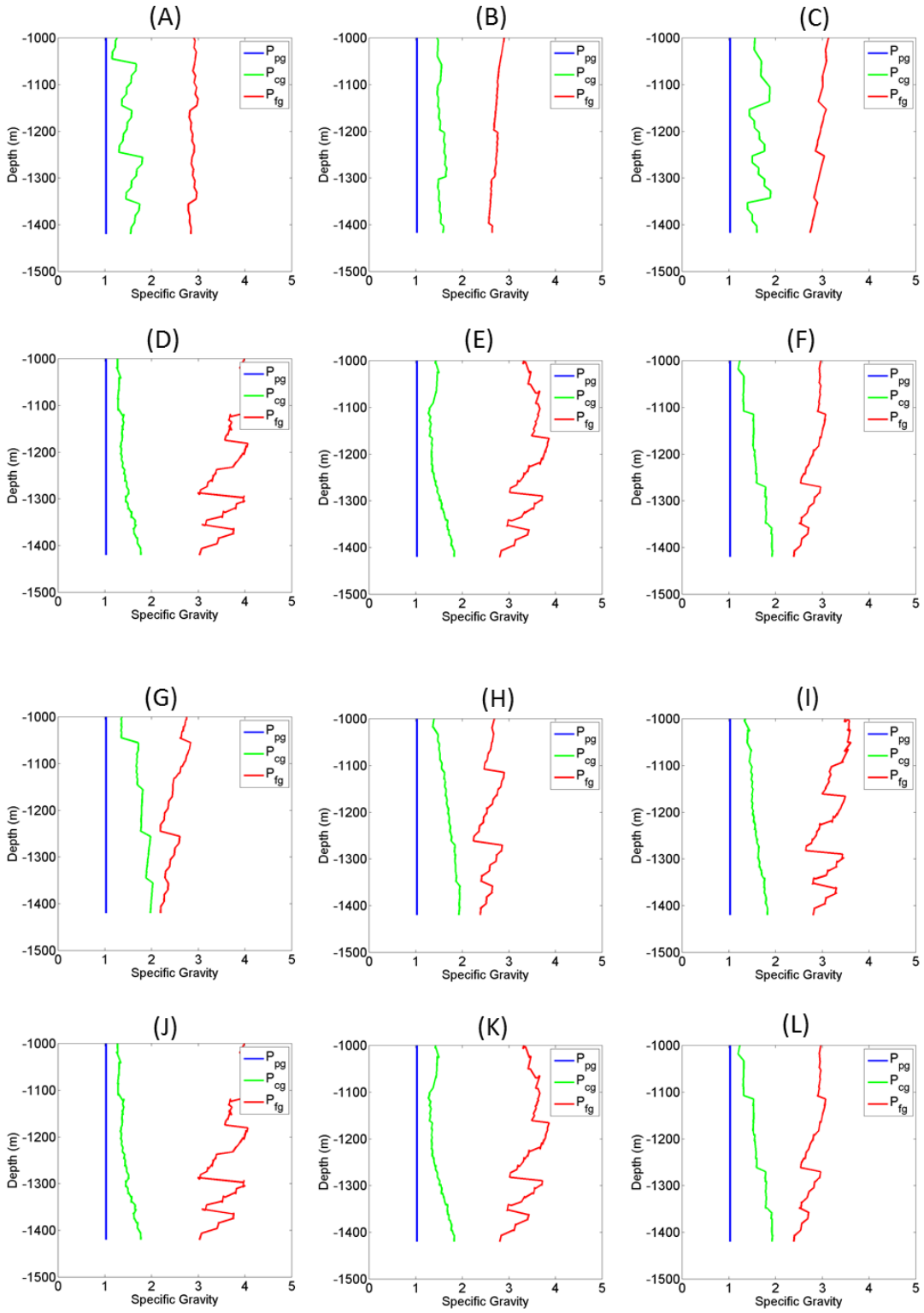
(A)
(B)
(C)
(D)
(E)
(F)
(G)
(H)
(I)
(J)
(K)
(L)
Depth (m)
-1000
-1100
-1200
-1300
-1400
-1500
0
1
2
3
4
5
Specific Gravity
P pg
P cg
P fg

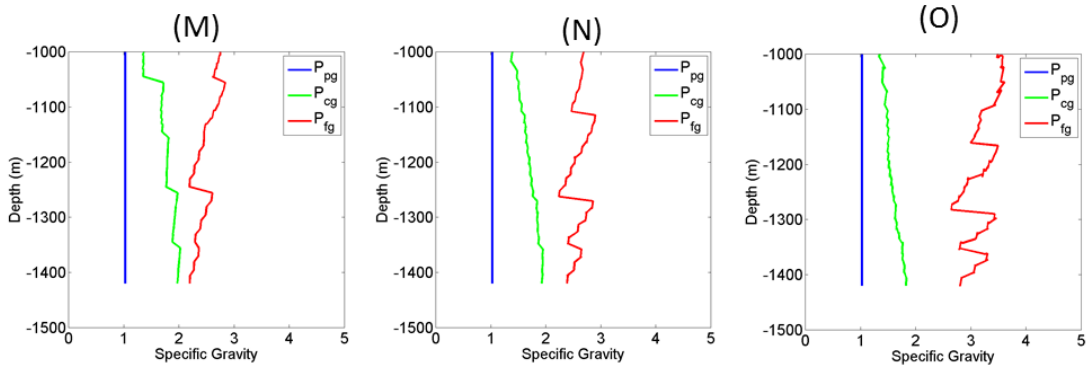

Where Figures A, B, and C are the specific gravity windows for the crest, limb, and valley respectively, and D, E, F, G, H, I, J, K, L, M, N, and O are the pressure windows for wells with azimuths of 0 , 30, 60, 90, 120, 150, 180, 210, 240, 270, 300, and 330 degrees respectively.

APPENDIX C

ANTICLINE MODEL COMPRESSIONAL STRESS REGIME OPERATIONAL WINDOWS

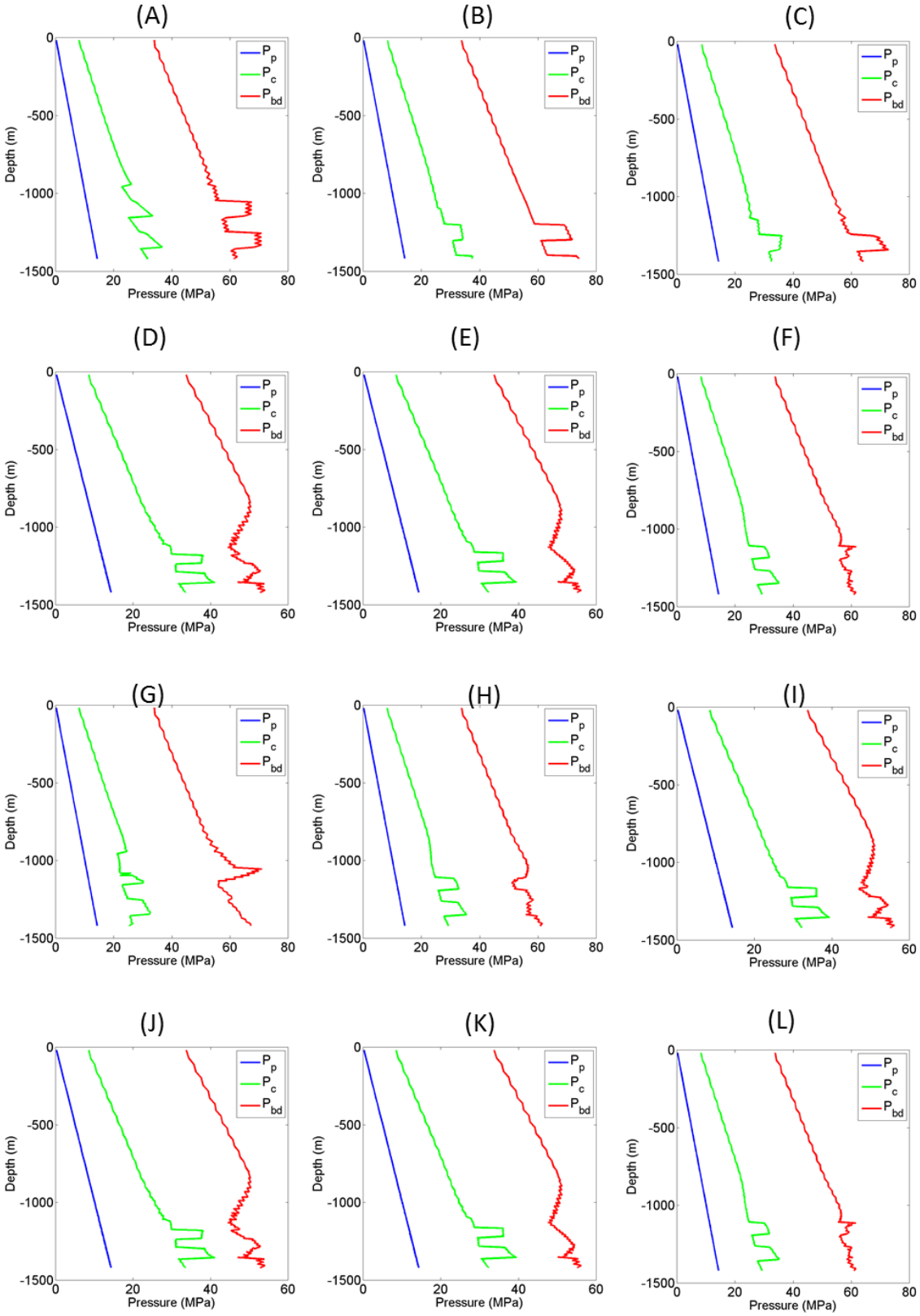
(A)
(B)
(C)
(D)
(E)
(F)
(G)
(H)
(I)
(J)
(K)
(L)
Depth (m)
Pressure (MPa)
P_p
P_c
P_bd

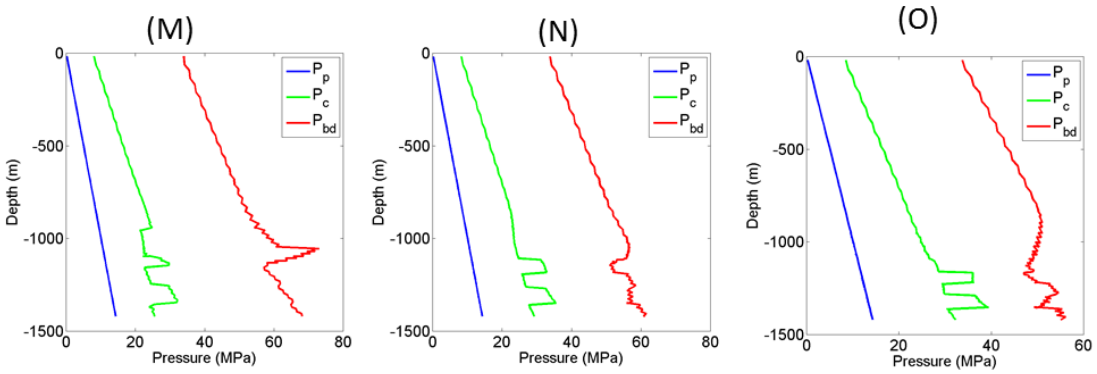

Where Figures A, B, and C are the pressure windows for the crest, limb, and valley respectively, and D, E, F, G, H, I, J, K, L, M, N, and O are the pressure windows for wells with azimuths of 0 , 30, 60, 90, 120, 150, 180, 210, 240, 270, 300, and 330 degrees respectively.

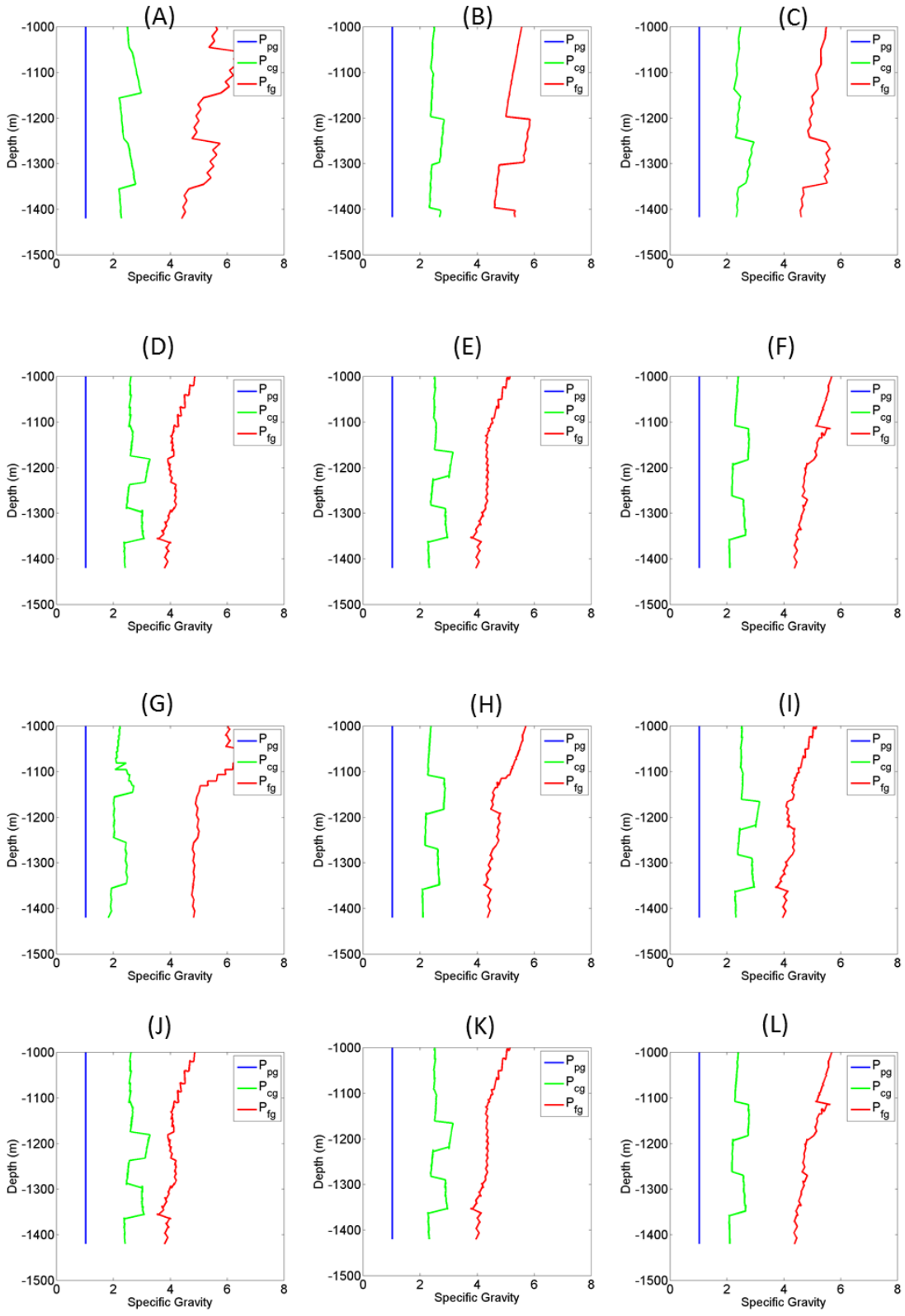
(A)
(B)
(C)
(D)
(E)
(F)
(G)
(H)
(I)
(J)
(K)
(L)
Depth (m)
-1000
-1100
-1200
-1300
-1400
-1500
Specific Gravity
0
2
4
6
8
P pg
P cg
P fg

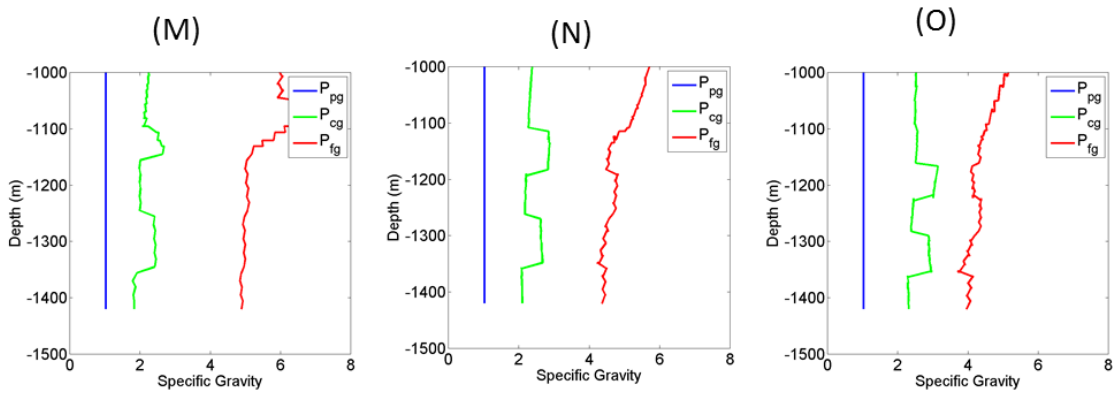

Where Figures A, B, and C are the specific gravity windows for the crest, limb, and valley respectively, and D, E, F, G, H, I, J, K, L, M, N, and O are the pressure windows for wells with azimuths of 0 , 30, 60, 90, 120, 150, 180, 210, 240, 270, 300, and 330 degrees respectively.

APPENDIX D

ANTICLINE MODEL STRIKE-SLIP STRESS REGIME OPERATIONAL WINDOWS

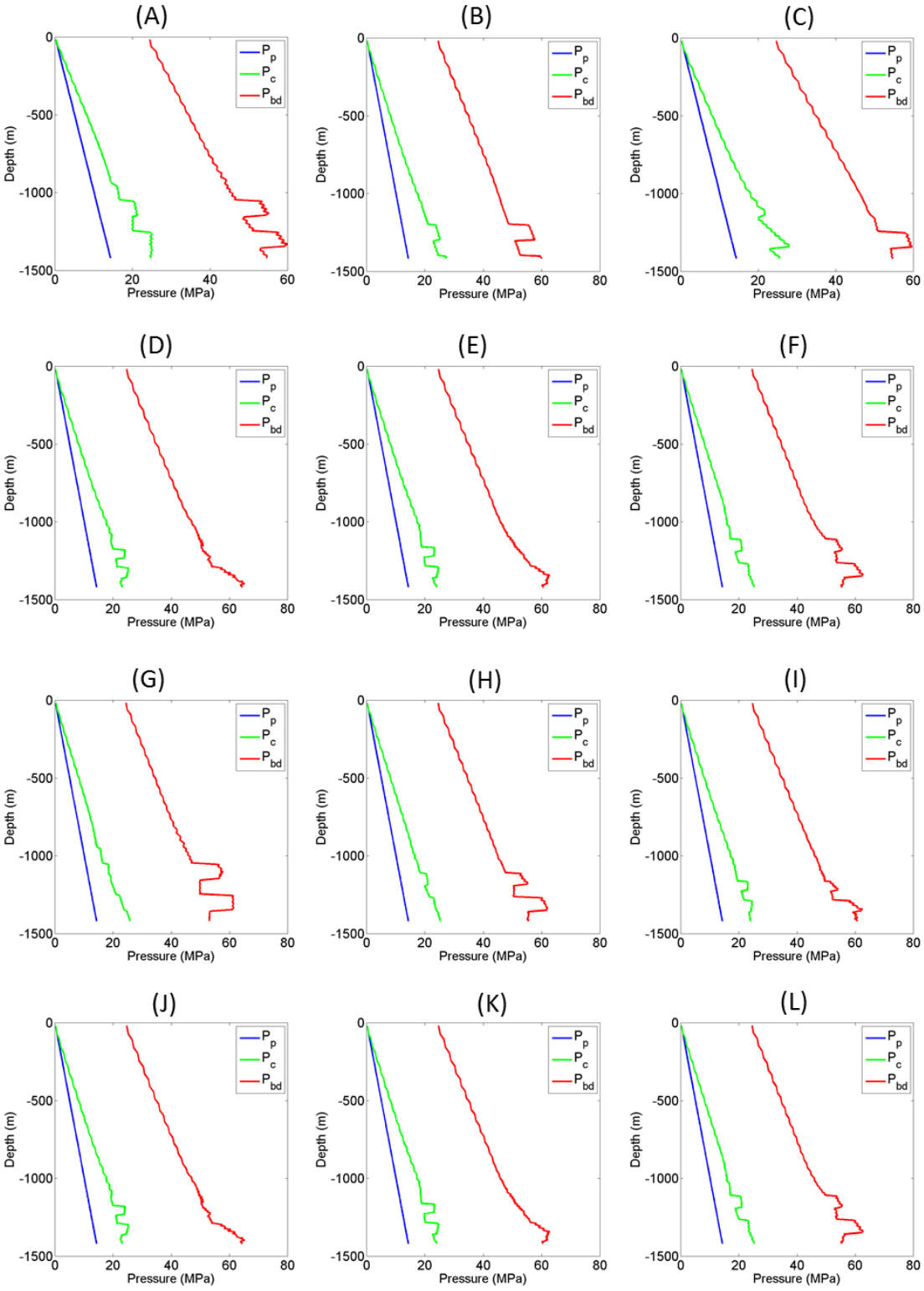
(A)
(B)
(C)
(D)
(E)
(F)
(G)
(H)
(I)
(J)
(K)
(L)
Depth (m)
Pressure (MPa)
P_p
P_c
P_bd

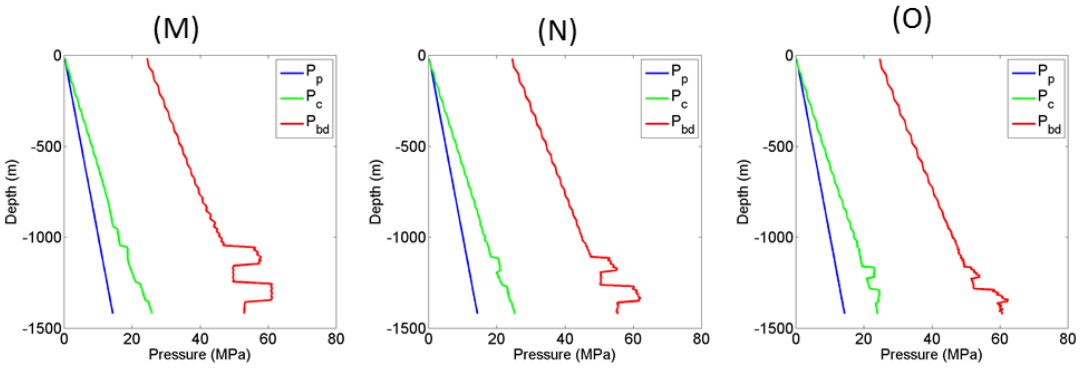

Where Figures A, B, and C are the pressure windows for the crest, limb, and valley respectively, and D, E, F, G, H, I, J, K, L, M, N, and O are the pressure windows for wells with azimuths of 0 , 30, 60, 90, 120, 150, 180, 210, 240, 270, 300, and 330 degrees respectively.

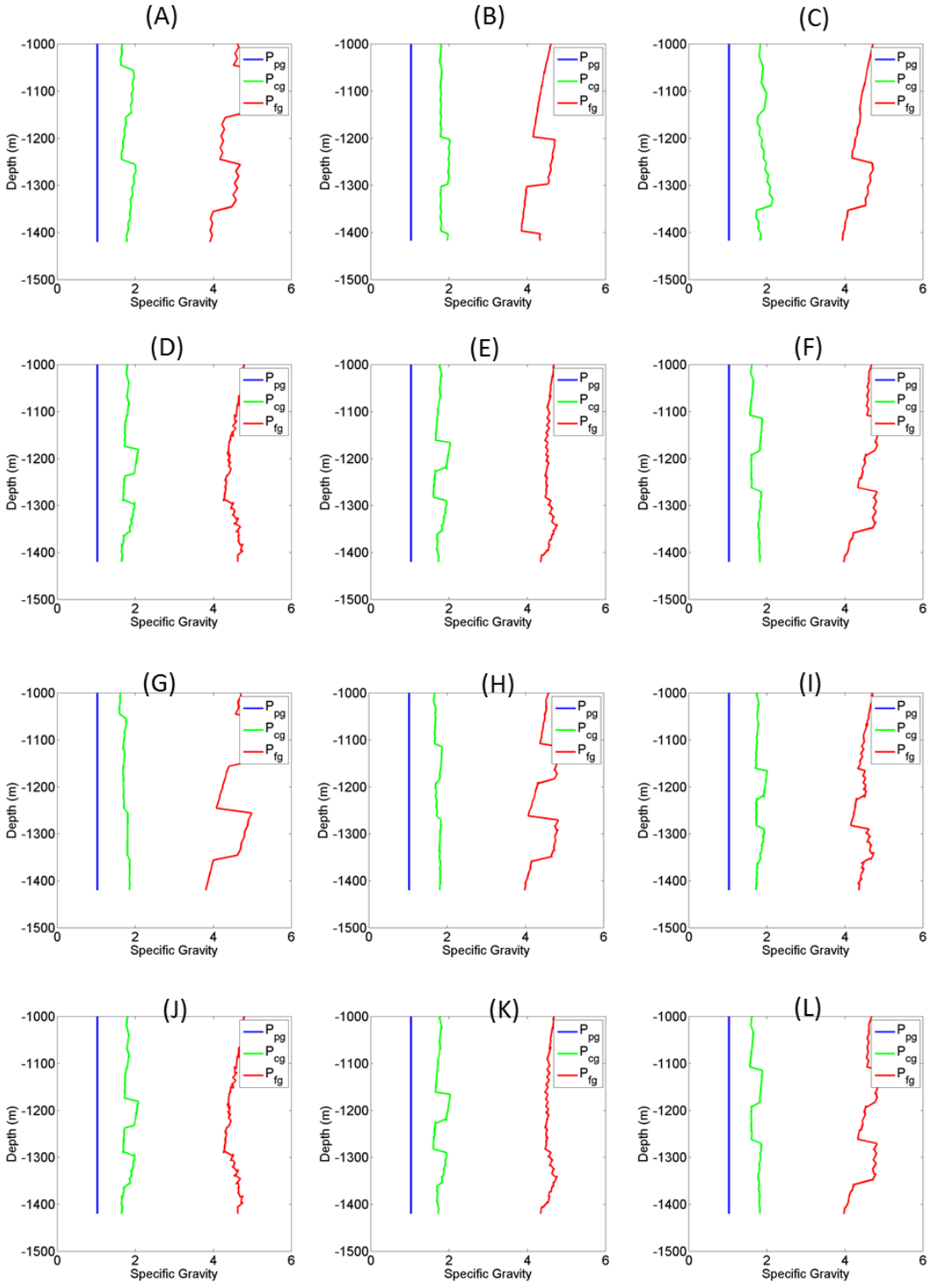
(A)
(B)
(C)
(D)
(E)
(F)
(G)
(H)
(I)
(J)
(K)
(L)
Depth (m)
-1000
-1100
-1200
-1300
-1400
-1500
Specific Gravity
0
2
4
6
P pg
P cg
P fg

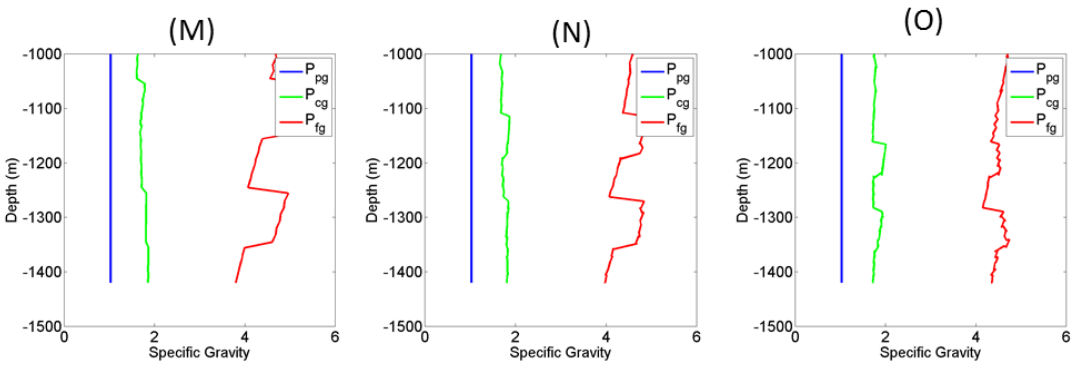

Where Figures A, B, and C are the specific gravity windows for the crest, limb, and valley respectively, and D, E, F, G, H, I, J, K, L, M, N, and O are the pressure windows for wells with azimuths of 0 , 30, 60, 90, 120, 150, 180, 210, 240, 270, 300, and 330 degrees respectively.

BIBLIOGRAPHY

Aadnøy, B.S.. U. of Stavanger, and A.K. Hansen. 2005. Bounds on In-Situ Stress Magnitudes Improve Wellbore Stability Analyses. *SPE Journal*. June: 115-120.

Addis, M.A. 1997. Reservoir Depletion and Its Effect on Wellbore Stability Evaluation. *International Journal of Rock mechanics & Mining Sciences* 34:3-4, paper No. 004.

Al-Ajmi, A.M., and R.W. Zimmerman. 2009. A new well path optimization model for increased mechanical borehole stability. *J. Pet. Sci. Eng.* 69: 53-62.

Amirlatifi, A., A. Eckert, R. Nygaard, B. Bai, X. Liu, and M. Paradeis. 2012. Role of Geometrical Influences of CO_2 Sequestration in Anticlines. In *46th U.S. Rock Mechanics Symposium, Chicago, IL, USA, 24-27 June 2012.*

Barton, C.A. and Moos, D., Peska, P., and Zoback, M.D. 1997. Utilizing Wellbore Image Data to Determine the Complete Stress Tensor: Application to Permeability Anisotropy and Wellbore Stability. *The Log Analyst.* 38:6.

Bois, A-P, A. Garnier, G. Galdiolo, and J-B Jaudet 2010. Use of a Mechanicstic Model To Forecast Cement-Sheath Integrity for CO_2 Storage. In *SPE Internationa Conference on CO_2 Capture, Storage, and Utilization, New Orleans, Louisiana, USA, 10-12 November 2010.*

Boresi, A.P., and R.J. Schmidt, (2002). *Advanced Mechanics of Materials*. John Wiley and Sons Inc, New York, NY.

Bosma, M., K. Ravi, W. Driel, and G. Schreppers. 1999. Design approach to sealant selection for the life of the well. In SPE, (*SPE 56536), 26 October, 1999. Houston, Texas.*

Bourgoyne, A.T. Jr., K.K. Millheim, M.E. Chnevert, and F.S. Young Jr. (1986), *Applied Drilling Engineering*. SPE Textbook Series Vol. 2

Brudy, M., M.D. Zoback, K. Fuchs, F. Rummel, and J. Baumgärtner. 1997. Estimation of the complete stress tensor to 8km depth in the KTB scientific drill holes: Implications for crustal strength. *J. of Geoph. Res.* 102(B8): 18,453-18,475.

Buchmann, T.J., G. Peters, and P.T. Connolly. 2008. Recent faulting in the Upper Rhine Graben (Germany): a 3D finite element approach to predict fault reactivation. In *42nd U.S. Rock Mechanics Symposium and 2nd U.S.-Canada Rock Mechanics Symposium, San Francisco, CA, 29 June – 2 July.*

Buchmann, T. J. (2008), Three Dimensional Multi-scale Finite Element Analysis of the Present-day Crustal State of Stress and the Recent Kinematic Behavior of the Northern and Central Upper Rhine Graben. Logos Verlag Berlin GmbH, Berlin.

Buchmann, T. J., and P. T. Connolly, (2007), Contemporary kinematics of the Upper Rhine Graben: A 3D finite element approach, Global and Planetary Change, 58(1), 287-309, doi: 10.1016/j.gloplacha.2007.02.012.

Byerlee, J. D. (1978), Friction of rocks. Pure and Applied Geophysics, v. 116(4-5),615-626.

Celia, M.A., S. Bachu, J.M. Nordbotten, S.E. Gasda, and H.K. Dahle. 2004. Quantitative Estimation of CO_2 Leakage from Geological Storage: Analytical Models, Numerical Models, and Data Needs. *Int'l Conf. Greenhouse Gas Control Technologies*. Paper ID 228 for GHGT-7.

Cooke, C.E. Jr., M.P. Kluck, and R. Medrano. 1983. Field Measurements of Annular Pressure and Temperature During Primary Cementing. *Journal of Petroleum Technology, V. 35, n. 8.* August 1983.

Cooper, G.A. 1994. Directional Drilling. *Scientific American.* 270(5): 82-87.

Coulomb, C.A. 1776. Essai sur une application des regles des maximis et minimis a quelquels problemesde statique relatifs, a la architecture. Mem. Acad. Roy. Div. Sav. 7: 343-387.

Dassault Systèmes (2011), ABAQUS® User Manual (version 6.11). SIMULIA, a division of Dassault Systèmes, Providence, Rhode Island.

Davis, R. O., and A.P. Selvadurai, (1996), Elasticity and geomechanics. Cambridge University Press.

Dhatt, G., and G. Touzot (2012), *Finite Element Method*. John Wiley and Sons.

Eckert, A., and P.T. Connolly. 2004. 2D Finite Element Modelling of Regional and Local Fracture Networks in the Eastern California Shear Zone and Coso Range, California USA. *Geothermal Resources Council Transaction*. 28: 643-648.

Engelder, T. 1993. Stress Regimes in the Lithosphere. *Princeton University Press.* 9780691085555.

Ewy, R.T. 1999. Wellbore-stability prediction by use of a modified Lade criterion. *SPE Drilling & Completion.* 14: 85-91.

Feng, Y., and Shi, X. 2013. Hydraulic fracturing process: roles of in-situ stress and rock strength. *Adv. Mat. Res.* 616-618: 435-440.

Fjaer, E., R.M. Holt, P. Horsrud, A.M. Raaen and R. Risnes. 2008. *Petroleum Related Rock Mechanics.*. 2nd ed. New York: Elsevier B.V.

Fontoura, S., C.E. Lautenschlaeger, G. Righetto, N. Inoue, R. Albuqueque, C.J. Goncalves, and M. Alcure. 2013. Workflow for Wellbore Integrity Analysis during Reservoir Development. Presented at the Offshore Technology Conference Brazil held in Rio de Janeiro, Brazil, 29-31 October 2013.

Freij-Ayoub, R., 2009. Casing Integrity in Hydrate Bearing Sediments. Presented at the 43rd US Rock Mechanics Symposium and 4th U.S.-Canada Rock Mechanics Symposium, Asheville, NC June 28th-July 1, 2009. ARMA paper 09-138.

Goodman, H.E., and P. Connolly. 2007. Reconciling Subsurface Uncertainty With the Appropriate Well Design Using the Mechanical Earth Model (MEM) Approach. In *31st Nigeria Annual International Conference and Exhibition, Abuja, Nigeria, 6-8 August*.

Gray, K.E., E. Podnos and E. Becker. 2007. Finite element studies of near-wellbore region during cemending operations: Part I. In *SPE(106998-MS), 31 March-3 April, Oklahoma City, Oklahoma, U.S.A.*

Haider, M.G., J. Sanjayan, and P.G. Ranjith 2012. Modeling of a Well-bore Composite Cylinder System for Cement Sheath Stress Analysis in Geological Sequestration of CO_2. In *46th U.S. Rock Mechanics Symposium, Chicago, IL, USA, 24-27 June 2012.*

Harrison J. P, and .J A. Hudson, (2000), Engineering rock mechanics-an introduction to the principles[M]. Access Online via Elsevier.

Hilbert, L.B. Jr., R.L. Gwinn, and T.A. Moroney. 1999. Field-Scale and Wellbore Modeling of Compaction-Induced Casing Failures. Presented at the 1998 SPE/ISRM Eurock, Trondheim, Norway, 8-10 July. SPE paper 56863.

Islam, M.A., Skalle, P., Al-Ajmi, A.M., and Søreide, O.K. 2010. Stability Analysis in Shale through Deviated Boreholes using the Mohr and Mogi-Coulomb Failure Criteria. In *44th US Rock Mechanics Symposium and 5th U.S.-Canada Rock Mechanics Symposium, Salt Lake City, UT, 27-30 June.*

Jaeger, J. C. and N. G. Cook, (1979), W, *Fundamentals of Rock Mechanics*. Chapman and Hall, London.

Jarrell, P.M., M.H. Stein, and Amoco Production Co. (1991). Maximizing Injection Rates in Wells Recently Converted to Injection Using Hearn and Hall Plots. SPE Production Operations Symposium, 7-9 April, Oklahoma City, Oklahoma. DOI 10.2118/21724-MS.

Kandil, A., A.A. El-Kady, and A. El-Kafrawy. 1994. Transient Thermal Stress Analysis of Thick-Walled Cylinders. *J. Mech. Sci.* Vol. 37, No. 7. Pp. 721-732, 1995.

Kirsch, G. 1898. Die Theorie der Elastizitaet und die Beduerfnisse der Festigkeitslehre. *Zeitschrift des Vereines Deutscher Ingenieure.* 42: 707.

Kocher, T., N.S. Mancktelow, and S.M. Schmalholz. 2008. Numerical modelling of the effect of matrix anisotropy orientation on single layer fold development. J. Struct. Geol. 30, 1013-1023.

Last, N.C., and M.R. McLean. 1996. Assessing the Impact of Trajectory on Wells Drilled in an Overthrust Region. *JPT.* July: 620-626.

Lee, M., A. Eckert, and R. Nygaard. 2011. Mesh optimization for finite element models of wellbore stress analysis. In *45th US Rock Mechanics/Geomechanics Symposium, San Francisco, CA, 26-29 June.*

Liu, X. 2011. Universal Technique Normalizes and Plans Various Well-Paths for Directional Drilling. In *SPE Middle East Oil and Gas Show and Conference, Manama, Bahrain, 25-28 September.*

Medina, C.R., J.A. Rupp, and D.A. Barnes. (2011), Effects of reduction in porosity and permeability with depth on storage capacity and injectivity in deep saline aquifers: A case study from the Mount Simon Sandstone aquifer, International Journal of Greenhouse Gas Control, 5,146-156, doi: 10.1016/j.ijggc.2010.03.001.

Mueller, B., J.B. Altmann, T. Mueller, A. Weisshardt, S. Shapiro, F. Schiling, and O. Heidbach. 2010. Tensor character of pore pressure/stress coupling in reservoir depletion and injection. 72nd EAGE Conference and Exhibition incorporating SPE EUROPEC 2010 (Barcelona 2010).

Meuller, D., and R. Eid. (2006), Characterizing early-state physical properties, mechanical behavior of cement designs. Paper SPE 98632 presented at the *Drilling Conference on 22 February,* Miami Beach, FL 2006.

Mitchell, S.A. 1997. Choosing corners of rectangles for mapped meshing. In *Proceedings of the thirteenth annual symposium on Computational geometry, New York, NY, 1997. 87-93.*

Nawrocki, P.A. 2010. Critical wellbore pressures using different rock failure criteria. In *International Symposium – 6th Asian Rock Mechanics Symposium, New Delhi, India,* 23-27 *October*.

Paradeis, M.A., A. Eckert, and X. Liu. 2012. Influences of Anticline Reservoir Geometry on Critical Pore Pressures Associated with CO_2 Sequestration. In *46th U.S. Rock Mechanics/ Geomechanics Symposium, Chicago, IL, 24-27 June.*

Pattillo, P.D. and Kristiansen, T.G. 2002. Analysis of Horizontal Casing Integrity in the Valhall Field. Paper SPE 78204 presented at the SPE/ISRM Rock Mechanics Conference, Irving, Texas, USA, 20-23 October. DOI: 10.2118/78204-MS.

Peska, P., and M.D. Zoback. 1995. Compressive and tensile failure of inclined well bores and determination of in situ stress and rock strength. *J. of Geo. Res.* 100(B7): 12,791-12,811.

Rahim, Z., A.A. Al-Kanaan, H.A. Al-Anazi, and M.S. Ahmed. 2012. Successful drilling of lateral wells in minimum horizontal stress direction for optimal fracture placement. *Oil & Gas J.* 110(12): 74-82.

Schutjens, P.M.T.M., J.R. Snippe, H. Mahani, J. Turner, J. Ita, and A.P. Mossop. 2012. Production-Induced Stress Change in and Above a Reservoir Pierced by Two Salt Domes: A Geomechanical Model and Its Applications. *SPE Journal.* March: 80-97.

Shahri, M.A., J.J. Schubert, and M. Amani (2005). Detecting and Modeling Cement Failure in High-Pressure/High-Temperature (HP/HT) Wells, Using Finite Element Method (FEM). Presented at the *International Petroleum Technology Conference* held in Doha, Qatar, 21-23 November 2005.

Shen, Z., and F.E. Beck. (2012). Three-Dimensional Modeling of Casing and Cement Sheath Behavior in Layered, Nonhomogeneous Formations. Presented at *IADC/SPE Asia Pacific Drilling Technology Conference and Exhibition* held in Tianjin, China, 9-11 July 2012.

Smart, K.J., D.A. Ferrill, and A.P. Morris. 2009. Impact of interlayer slip on fracture prediction from geomechanical models of fault-related folds, AAPG bulletin, 90(11), 1447-1458, doi: 10.1306/05110909034.

Smart, K.J., D.A. Ferrill, A.P. Morris, B.J. Bichon, D.S. Riha, and L. Huyse,. 2010a. Geomechanical modelling of an extensional fault-propagation fold: Big Brushy Canyon monocline, Sierra Del Carmen, Texas. American AAPG bulletin 94, 221-240.

Smart, K.J., D.A. Ferrill, A.P. Morris, and R.N. McGinnis. 2010b. Geomechanical modelling of a reservoir-scale fault-related fold: the Bargy anticline, France. 44th U.S. Rock Mechanics Symposium, ARMA Paper 10-201.

Smart, K.J., D.A. Ferrill, D.W. Sims, N.M. Franklin, G.I. Ofoegbu, and A.P. Morris. 2004, Integrated structural analysis and geomechanical modeling: an aid to

reservoir exploration and development. Gulf Rocks 2004-6th North American Rock Mechanics Symposium: Rock Mechanics Across Borders and Disciplines. Houston, TX, 5-9 June 2004: ARMA/NARMS Paper 04-470.

Tan, Q., J. Deng, and B. Yu. 2013. Study on Borehole Stability of Unconsolidated Sandstone in Depleted Reservoir. *Adv. Mat. Res.* 616-618: 720-725.

Terzaghi, K. (1936), The shearing resistance of saturated soils and the angle between planes of shear, in Proc. Int. Conf. Soil Mech. Found. Eng., Vol.1, Harvard University Press,Cambridge, MA,pp . 54–6.

Tran, M.H., and Y.N. Abousleiman. 2010. The impacts of failure criteria and geological stress states on the sensitivity of parameters in wellbore stability analysis. In *44th U.S. Rock Mechanics Symposium and 5th U.S.-Canada Rock Mechanics Symposium, Salt Lake City, UT, 27-30 June.*

Turcotte, D. L., and G. Schubert, (2002), *Geodynamics*. Cambridge University Press, New York.

Twiss, R.J and E.M. Moores. 2007. Mechanics of Natural Fractures and Faults. In *Structural Geology*, 2nd ed. New York: W.H. Freeman and Company, 231-264.

Yang, X., L. Zhiyuan, H. Zhang, Q. Xiong, and H. Liu. 2012. An analysis on wellbore collapse of open hold completion in carbonate formation. *Appl. Mech. And Met.* 220-223: 150-156.

Zare-Reisabadi, M.R., A. Kaffash, and S.R. Shadizadeh. 2012. Determination of optimal well trajectory during drilling and production based on borehole stability. *J. of Rock Mech. And Min. Sci.* 56: 77-87.

Zhang, J., W.B. Standifird, K., Adesina, and G. Keaney. 2006. Wellbore Stability with consideration of pore pressure and drilling fluid interactions. In *41st U.S. Symposium on Rock Mechanics, Golden, CO, 17-21 June.*

Zhang, Y., Mancktlow, N.S., Hobbs, B.E., Ord, and H.B. Muhlhaus, (2000), Numerical modeling of single-layer folding: clarification of an issue regarding the possible effect of computer codes and the influence of initial irregularities, J. Struct. Geol., 22, 1511-1522, doi: 10.1016/S0191-8141(00)00063-8.

Zhang, Y., N.S. Hobbs, B.E. Ord, and H.B. Muhlhaus, (1996), Computer simulation of single-layer buckling, J. Struct. Geol., 18, 645-655, doi: 10.1016/S0191-8141(96)80030-7.

Zheng, J., X. Zhou, L. Shao, and X. Jin. 2010. Simple Three-Step Analytical Scheme for Prediction of Elastic Moduli of hardened Cement Paste. *J. of Mater. In Civ. Eng.* 2010.22:1191-1194.

Zienkiewicz, O. C., R. L. Taylor, and J. Z. Zhu. (2005), The finite element method: its basis and fundamentals. Elsevier,UK.

Zoback, M.D. 2007. *Reservoir Geomechanics* 5th prtg. New York: Cambridge University

VITA

Nevan Christopher Himmelberg was born in Kansas City, Kansas. He earned his Bachelor's degree in Petroleum Engineering from Missouri University of Science and Technology in May 2012. Immediately after completing his Bachelor's degree Nevan enrolled in the Petroleum Engineering Master's program at the same university. During his time as a Master's student he held positions of graduate research assistant and graduate teaching assistant in the Department of Geological Science and Engineering. Nevan completed his Master's degree in Petroleum Engineering in May 2014.